Doctoral Thesis

SYNTHESIS AND PROPERTIES OF EPITAXIAL OXIDE THIN FILMS PREPARED BY POLYMER ASSISTED DEPOSITION

José Manuel Vila Fungueiriño

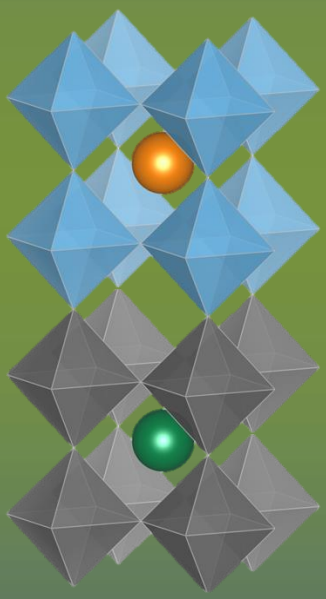

USC
UNIVERSIDADE DE SANTIAGO DE COMPOSTELA

Departamento de Química Física
Facultade de Química

Santiago de Compostela
2016

Doctoral Program in Materials Science

Synthesis and properties of epitaxial oxide thin films prepared by polymer assisted deposition

José Manuel Vila Fungueiriño

2016

Departamento de Química Física. Facultade de Química.
Universidade de Santiago de Compostela

USC
UNIVERSIDADE
DE SANTIAGO
DE COMPOSTELA

Dr. **José Francisco Rivadulla Fernández**, Profesor Titular at the Department of Physical Chemistry, University of Santiago de Compostela and Dr. **Beatriz Rivas Murias**, Ph. D. at the Department of Physical Chemistry, University of Santiago de Compostela.

DECLARE:

That this thesis entitled *Synthesis and properties of epitaxial oxide thin films prepared by polymer assisted deposition* was carried out by José Manuel Vila Fungueiriño under our supervision.
In Santiago de Compostela, 26th April, 2016.

Signed:

José Francisco Rivadulla Fernández Beatriz Rivas Murias

José Manuel Vila Fungueiriño

USC
UNIVERSIDADE
DE SANTIAGO
DE COMPOSTELA

Acknowledgments

On these humble lines I would like reflect my thankfulness to everyone who contributed to that this thesis came to a fruitful end.

The first in this list, without any doubt, has to be the director of the thesis, Prof. Francisco Rivadulla. Without his guidance and perseverance in the project, support, commitment, dedication, enthusiasm, tenacity, work, for always be there, etc.; I could increase the number of adjectives but I could never fully describe the gratitude that represented to me his confidence. I do not know if you still remember my job interview at FEDER, you asked me for compromise and responsibility and expressed how the project was really important to you. I really hope that I could fulfill some of your expectations.

I have to thank the co-director of the thesis, Beatriz Rivas, for her effort and perseverance during the experimental work.

I am deeply grateful to my colleagues of group, what a great team! Starting with Camilo, an example of order and scientific meticulousness, but first of all a person who does enhance the spirit of the group. Víctor, always ready to help me in any set-up problem. I also thank to Elias, Alex, Eric, Tinh, Lucia and Manuel (almost a member of the group). I hope one day we will get back to working together in any interesting project.

I would like to acknowledge Prof. Massimo Lazzari for NMR and SEC measurements for chemical characterization of polymers. His contribution was really valuable towards the comprehension of the role of purification of polymer in PAD.

I also have to thank to Francisco Guitián and Alfredo for his disposition to ICP analysis of metal solutions. Juan Antelo is acknowledged for potentiometric titrations, and Manolo Bañobre for his kindly support to viscosity determination in Braga. Arturo López and Carlos Vázquez are acknowledged for let me use the AFM in FEDER, whose people I also like to thank, especially Mª Carmen with whom I share the practices of Chemist degree.

I would like to thank Irene Lucas for the excellent work to move forward with the bilayers for tunnel junctions. Ananda Sagari is also acknowledged for boron oxide films.

I am very grateful and satisfied with my stays. In Barcelona I am indebted to Jose Santiso for his warm hospitality and generous teaching on structural characterization of thin films. I also thank his group at CIN2, especially Jaume and Nuria.

In Lyon I got the fortune and opportunity to work closely with Adrián Carretero, quillo! I would like to thank your effort and creativity in the laboratory, and coexistence in that French social housing. I also appreciate the collaboration with his colleagues at INL Lyon, especially Romain and Michel.

I would like to thank my friends and colleagues, Narcís Mestres, Victor Pardo, Daniel Baldomir. Surely I do not mention people who deserve to be in.

I would like to recognize the financial assistance from Ministerio de Economía y Competitividad (MINECO) of Spain for support me with a PhD grant of the FPI program (MAT2010-16157).

Non quixera esquecerme da xente allea á tese pero que sufriron con ela. En especial a Martín o meu irmán, que sabe por todo o que pasamos e aguantamos, a miña nai e o meu avó Manuel. E á familia de Ana, a miña familia tamén, da que sempre botarei de menos ó señor Ricardo.

E por suposto, máis que merecidamente agradézoche a ti, Ana, polo teu apoio e paciencia, amor e ánimo, por todo o que tiveches que pasar comigo, relacionado ou non coa tese. Por todo iso e máis, sempre saberei que podo contar contigo, e ti comigo.

Resumo

O desenvolvemento de métodos físicos e químicos que permitiron a estruturación de materiais en forma de películas delgadas de espesor nanométrico supuxo un extraordinario logro científico e tecnolóxico. Na década dos 1970´s fabricáronse as primeiras películas delgadas epitaxiais de gran calidade da man de sofisticadas técnicas de fabricación que implican a evaporación a partir dun material en condicións de alto baleiro. Entre estes métodos os máis relevantes son *Pulsed Laser Deposition* (PLD), *Sputtering*, *Molecular Beam Epitaxy* (MBE) e *Atomic Layer Deposition* (ALD). Estas técnicas permiten acadar un extraordinario control sobre a síntese (estequiometría, espesor, homoxeneidade) pero precisan complexos e custosos sistemas de baleiro. O alto custe desta tecnoloxía impide o acceso a importantes sistemas de estudo dentro da química e da física da materia condensada para moitos grupos de investigación.

O método empregado nesta tese, a Deposición Asistida por Polímero (PAD), é un método accesible para a síntese de películas delgadas, na que a calidade dos filmes producidos chega a ser comparable ós obtidos por PLD ou *Sputtering*. Estes filmes obtéñense mediante un proceso respectuoso co medio ambiente no que non se precisan disolventes orgánicos nin procesos de síntese complexos con moitas etapas intermedias. Resulta ademais un método con potencial de ser escalable para procesos industriais.

Nesta tese descríbense os aspectos químicos máis relevantes no método PAD e o proceso de optimización dos mesmos para obter películas delgadas epitaxiais de óxidos multicatiónicos de gran calidade. Para elo analizouse a estrutura e o comportamento de polímeros tanto en disolución como ante a súa degradación térmica, e determinouse o seu grao de retención con distintos metais en combinación con varios axentes quelatantes. A síntese e a caracterización de filmes aplicouse a un conxunto de óxidos con diferentes composicións e propiedades, controlando o espesor das películas e comparando os efectos das condicións de crecemento coas dos procesos físicos, en particular PLD. Ademais, combináronse dous materiais distintos na mesma mostra en forma de bicapas cunha clara interface entre eles. Todo este avance na síntese sobre substratos monocristalinos aplicouse a estruturas funcionais monoliticamente integradas de óxidos en silicio.

Resumen

El desarrollo de métodos físicos y químicos que permitieron la estructuración de materiales en forma de películas delgadas de espesor nanométrico supuso un extraordinario logro científico y tecnológico. En la década de los 1970´s se fabricaron las primeras películas delgadas epitaxiales de gran calidad mediante el uso de sofisticadas técnicas de fabricación que implican un proceso de evaporación a partir de un material en condiciones de alto vacío. Entre estos métodos, *Pulsed Laser Deposition* (PLD), *Sputtering*, *Molecular Beam Epitaxy* (MBE) y *Atomic Layer Deposition* (ALD) son los más relevantes. Estas técnicas permiten alcanzar un extraordinario control sobre la síntesis (estequiometría, espesor, homogeneidad), pero necesitan un sistema de alto vacío. El alto coste de esta tecnología impide el acceso a importantes sistemas de estudio dentro de la química y la física de la materia condensada para muchos grupos de investigación.

El método empleado en esta tesis, la Deposición Asistida por Polímero (PAD), es un método químico accesible para la síntesis de películas delgadas, en el que la calidad de las películas llega a ser comparable a la de las obtenidas por PLD o *Sputtering*. Estas películas se obtienen mediante un proceso respetuoso con el medio ambiente en el que no es necesario el uso de disolventes orgánicos ni complejos procesos de síntesis. Y resulta además un método con potencial escalable para procesos industriales.

En esta tesis se describen los aspectos químicos más relevantes del método PAD y el proceso de optimización de los mismos para la obtención de películas delgadas epitaxiales de óxidos multicatiónicos de gran calidad. Para ello se ha analizado la estructura y el comportamiento de los polímeros tanto en disolución como ante su degradación térmica, y se ha determinado su grado de retención con distintos metales en combinación con varios agentes quelatantes. La síntesis y caracterización de películas se ha aplicado a un conjunto de óxidos con diferentes composiciones y propiedades, controlando el espesor de las películas y comparando los efectos de las condiciones de crecimiento con los de los procesos físicos. Además, se han combinado dos materiales distintos en la misma muestra en forma de bicapas con una clara interfase entre ellos. Todo este avance en la síntesis sobre substratos monocristalinos se ha aplicado a estructuras funcionales monolíticamente integradas de óxidos en silicio.

Abstract

The development of physical and chemical methods that allowed structuring materials in the form of nanometer thick films represented an extraordinary scientific and technological achievement. In the 1970's the first high-quality epitaxial thin films were fabricated through the use of sophisticated manufacturing techniques which imply evaporation from a source under high vacuum. Among these methods Pulsed Laser Deposition (PLD), Sputtering, Molecular Beam Epitaxy (MBE), and Atomic Layer Deposition (ALD) are the most relevant. These techniques lead to extraordinary control over the synthesis (stoichiometry, thickness, homogeneity), but require a high vacuum system. The high cost of this technology prevents many research groups the access to these studies.

The method used in this thesis, the Polymer Assisted Deposition (PAD), is an affordable method for thin films synthesis, whose quality is in many aspects comparable to those obtained by PLD or Sputtering. These films are obtained by a process respectful with the environment, avoiding the need to use organic solvents or complex synthesis processes. Moreover, it is a scalable method with potential for applications in industrial processes.

This thesis describes the most relevant aspects in PAD method as well the process of optimization to obtain high quality epitaxial thin films of multicationic oxides. For this we have analyzed the structure and the behavior of polymers both in solution and under thermal degradation, and it has been determined the degree of retention for different metals in combination with various chelating agents. The synthesis and characterization of thin films have been applied to a set of oxides with different compositions and properties, controlling the thickness, stoichiometry, etc. The effect of growth conditions was studied by comparison with films prepared by classical physical methods. Furthermore, two different materials were combined in the same structure in the form of bilayers with a clear interface between the two individual layers. All this progress over single-crystal substrates was used to deposit functional oxides integrated on silicon at the end of this thesis.

USC
UNIVERSIDADE
DE SANTIAGO
DE COMPOSTELA

Contents

List of acronyms

2D	Two-dimensional
2-MOE	2-methoxyethanol
AFM	Atomic Force Microscopy
ALD	Atomic Layer Deposition
ATR	Attenuated Total Reflectance
BST	$(Ba,Sr)TiO_3$
C-AFM	Conductive Atomic Force Microscopy
CAS	Chemical Abstracts Service
CBD	Chemical Bath Deposition
cDTPA	Diethylenetriaminepentaacetic dianhydride
CSD	Chemical Solution Deposition
DI	De-Ionized
DOSY	Diffusion Ordered Spectroscopy
DSP	Digital Signal Processor
DTGS	Deuterated Triglycine Sulfate
DTPA	Diethylenetriaminepentaacetic acid
EDTA	Ethylenediaminetetraacetic acid
EDX	Energy-Dispersive X-Ray
FC	Field-Cooled
FIB	Focused Ion Beam
FM-I	Ferromagnetic-Insulator
FMR	Ferromagnetic Resonance
FT-IR	Fourier Transform - Infrared
FWHM	Full Width at Half Maximum

GSO	$GdScO_3$
HAADF-STEM	High-Angle Annular Dark Field Scanning Transmission Electron Microscopy
HSQC	Heteronuclear Single Quantum Coherence
ICP-AES	Inductively Coupled Plasma - Atomic Emission Spectroscopy
LAO	$LaAlO_3$
LCO	$LaCoO_3$
LMO	$LaMnO_3$
LSMO	$La_{0.7}Sr_{0.3}MnO_3$
MBE	Molecular Beam Epitaxy
MOD	Metal-Organic Decomposition/Deposition
MPMS	Magnetic Property Measurement System
MR	Magnetoresistance
MWCO	Molecular Weight Cut-Off
NMR	Nuclear Magnetic Resonance
NOE	Nuclear Overhauser Effect
PAD	Polymer Assisted Deposition
PECS	Precision Etching and Coating System
PEI	Polyethyleneimine
PEIC	Carboxylated Polyethyleneimine
PEO	Poly(Ethylene Oxide)
PFG	Pulsed-Field Gradient
PFM	Piezoresponse Force Microscopy
PIPS	Precision Ion Polishing System
PLD	Pulsed Laser Deposition
PLZT	$(Pb,La)(Zr,Ti)O_3$. Lanthanum-doped Lead Zirconium Titanate
PPC	Parallel Plate Collimator
PPEI	Phosphorylated Polyethyleneimine
PSPD	Position Sensitive Photo Detector
PZT	$Pb(Zr,Ti)O_3$. Lead Zirconium Titanate
RSM	Reciprocal Space Map
SEC	Size Exclusion Chromatography
SEM	Scanning Electron Microscopy
SILAR	Successive Ion Layer Absorption and Reaction
SPEI	Sulfonated Polyethyleneimine
SPM	Scanning Probe Microscopy

SQUID	Superconducting Quantum Interference Device
STM	Scanning Tunneling Microscopy
STO	$SrTiO_3$
TDL	Theoretical Detection Limit
TEM	Transmission Electron Microscopy
TGA	Thermogravimetric Analysis
TIO	Ti-doped In_2O_3
TOCSY	Total Correlation Spectroscopy
UV-Vis	Ultraviolet-visible
XRD	X-Ray Diffraction
XRR	X-Ray Reflectivity
YSZ	Yttria-Stabilized Zirconia
ZFC	Zero-Field Cooled

USC
UNIVERSIDADE
DE SANTIAGO
DE COMPOSTELA

Motivation

Oxides show an extraordinary variety of physical properties with applications in many different fields: mechanics, optics, magnetism, energy harvesting, etc. This diversity comes from a high structural and composition flexibility, which results in a wide range of fundamental electronic and magnetic interactions [i,ii]. In order to exploit these properties and new phenomena, it requires the fabrication of highly crystalline thin films. An increasing number of oxides have been synthesized as epitaxial thin films, multilayers or superlattices during the last decades, by using sophisticated growing techniques, mostly by high vacuum physical deposition (MBE, Sputtering, PLD, and ALD).

These materials are characterized by excellent chemical and crystalline homogeneity over the whole sample, abrupt interfaces, and low roughness. Although sometimes polycrystalline films are enough for meeting the bulk properties in a reduced dimension, single-crystal epitaxial films are required for fundamental studies and some advanced applications. However, achieving an epitaxial film by means of a chemical solution deposition (CSD) method is challenging, and the results obtained by these routes correspond mostly to polycrystalline samples. For this reason the results obtained by Polymer Assisted Deposition (PAD) in the last decade opened a promising and affordable route for the synthesis of high quality epitaxial films. Moreover, in contrast to other CSD methods, PAD was selected because in principle does not require complex chemical manipulation, toxic reactants, distillation, refluxing, etc.

However, many chemical aspects of the method are still unclear. As a result, some results have been difficult to reproduce by different groups. In this thesis we identified the most relevant chemical aspects of the PAD method. We optimize the method to produce homogenous epitaxial thin films of multicationic oxides over areas of several square centimeters. As we show in this thesis the films deposited by this method grow close to thermodynamic equilibrium conditions, conditioned by substrate, strain, temperature, thermal annealing, atmosphere, etc. This poses an important difference with respect to

classic physical methods, like PLD, where kinetic aspects define the growth of the films over thermodynamics ones. So, not only studying the materials synthesized but also studying the synthesis process itself will provide important conclusions to advance further in the design of more effective chemical methods, and to add further functionalities to the material.

We applied the PAD method in this thesis to a wide range of perovskite-type oxides: manganites $La_{1-x}Sr_xMnO_3$ and $La_{1-x}Ca_xMnO_3$; cobaltite $LaCoO_3$; titanate $SrTiO_3$, ferrite $BiFeO_3$, iridate $SrIrO_3$, and epitaxial bilayers of $LaCoO_3/La_{1-x}Sr_xMnO_3$.

We achieved, by the first time, the fabrication of epitaxial bilayer heterostructures with abrupt quality interfaces by chemical methods. The ability to synthesize bilayers combining materials with different properties is highly desirable for sophisticated technological applications.

In addition, the synthesis of elusive materials for high vacuum process was also obtained, showing the versatility of the PAD method. The problem to synthesize thin films of these materials by standard high-vacuum physical methods resides in the difficult to transfer their stoichiometry from bulk, because the distinct nature of cations in their structures. We will demonstrate the high-quality synthesis by PAD of $Ca_3Co_4O_9$, $Sr_3Co_4O_9$, $[Bi_{1.74}Sr_2O_4][CoO_2]_{1.82}$, $[Bi_2Ba_{1.8}Co_{0.2}O_4][CoO_2]_2$, and $[Bi_{1.68}Ca_2O_4][CoO_2]_{1.69}$.

Finally, the possibility of soft integration of oxides in silicon by PAD in combination with MBE was explored in this thesis. Silicon is the second most abundant element (just after oxygen) in the earth´s crust and the basis for electronic industry. However the deposition of epitaxial oxides on silicon is complicated as a native SiO_2 barrier tends to grow at interface. To overcome this, we attempted a strategy of coupling chemical solution method with buffer layers of STO deposited by MBE.

1. Introduction to chemical methods for thin-film deposition

1.1. Review of chemical solution methods for the synthesis of oxide thin films

There are many different methods to obtain oxides thin films, either by physical or chemical routes. In this section we focus on chemical methods (as alternative to physical ones) that use liquid solutions, so called Chemical Solution Deposition (CSD) methods, and review shortly the most common for synthesizing thin films. There is a great diversity of such methods compiled in literature [3-7]: sol-gel, chemical bath deposition (CBD), chelate processes, hydrolysis-condensation, Polymer Assisted Deposition (PAD), Metal-Organic Decomposition (MOD), Successive Ion Layer Absorption and Reaction (SILAR), hydrothermal, electrochemical, etc. In the next pages are described the most important chemical routes utilized for oxide thin film fabrication.

CSD methods must satisfy several requirements: solubility of the precursors, homogeneity of the solution without phase segregation (i.e. precipitation), long term stability of the solution, good adherence and viscosity of solution to substrate, and total decomposition of the precursors in the thermal treatment without cracking of the film.

The main advantages of chemical solution deposition (CSD) methods with respect to physical ones are the low cost, easy implementation and the applicability for coating large areas. Any CSD method follows three general steps (Figure 1):

1. Preparation of a stable solution (precursor solution) containing the cations of interest from soluble precursors.
2. Deposition of the solution onto a substrate by spin coating, dip coating, spray coating, stamping, microcontact printing, inkjet printing, or any other method able to coat the substrate surface with a homogeneous layer of the precursor solution.
3. Thermal treatment in a given atmosphere and temperature to remove the solvent and organic parts of the solution and induce the crystallization of the inorganic film. This process might involve some intermediate steps with different temperatures, depending on the final composition of the film.

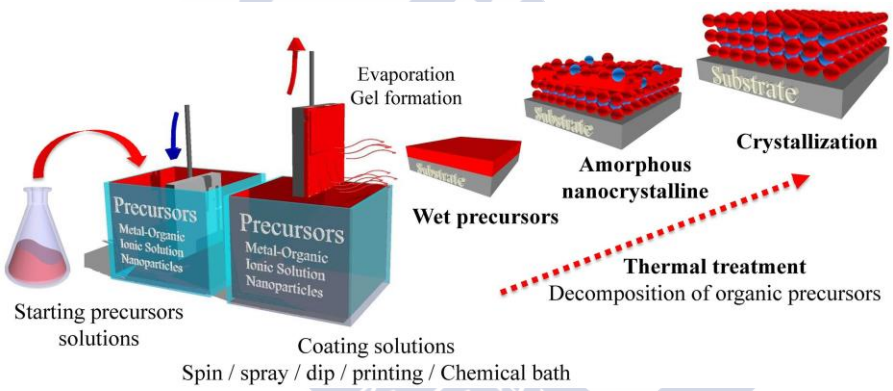

Figure 1. Scheme of the general steps in a Chemical Solution Deposition process. In this example the deposition onto the substrate is carried out by dip coating.

1.1.1. Sol-gel processes

Sol-gel is the most extended chemical deposition method for thin film preparation [8-11]. It is very common for the synthesis of oxides [12], in the form of bulk [13,14], powders [15,16], coatings [17,18], nanopowders [19,20], nanoparticles [21,22], nanocrystals [23,24], nanotubes [25,26] or porous structures [27-29]. It has been used since the nineteenth century [30] for preparing inorganic compounds because it reduces the temperature [31,32] and time needed to form the final material with respect to typical solid state reaction conditions. The success of sol-gel processes can be quantified attending to the number of documents published, which increased continuously during the last decades (Figure 2).

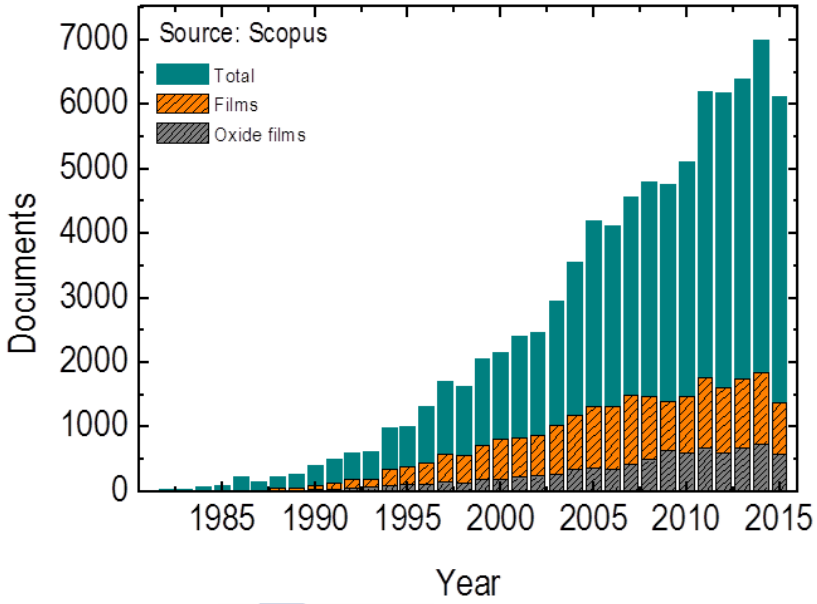

Figure 2. Number of scientific papers published during the period 1981-2015 using sol-gel techniques, indicating also these exclusively for the preparation of oxide films. The search criteria have been "sol-gel", "sol-gel film" and "sol-gel oxide film". Data obtained from *Scopus* database.

The name "sol-gel" is derived from the fact that a colloidal suspension of solid particles in a liquid called *sol*, condenses into a solid network called *gel*, after a slow evaporation of the solvent. The precursors for the preparation of colloids are reactive metal salts or metalorganic compounds, a metal element surrounded by several organic ligands, generally alkoxides. An important feature in this route is the use of particularly reactive species to moisture [33,34], as metal alkoxides $M(OR)_x$, that must be managed generally under inert atmosphere. The most employed alkoxides are ethoxides, propoxides, isopropoxides, butoxides, sec-butoxides, etc. derived from their respectively parent alcohol. That requires complex manipulation of reactants in dry atmosphere and of solution with refluxing, distillation, control of hydrolysis and condensation, etc. Organic solvents (ethanol, 1,3-propanediol, 2-methoxyethanol (2-MOE), 2-butoxyethanol) have to be employed instead of water, increasing the toxicity of the process, especially in the case of 2-MOE. Alkoxides with polar organic parts (amine, keto, alcohol), as aminoethoxide, are particularly interesting because they can react in water as solvent with a controllable hydrolysis.

This method is able to synthesize different types of products both from the sol and from the gel precursors (Figure 3).

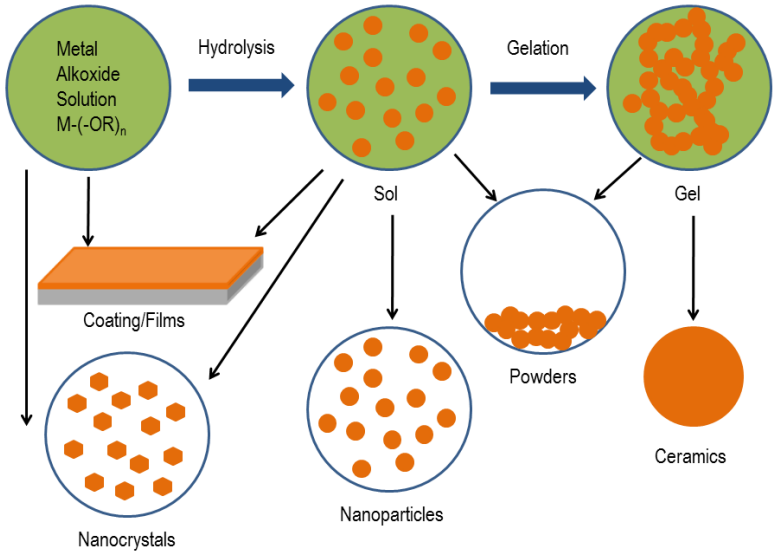

Figure 3. Schematic description of sol-gel process and some of the products than can be obtained. Both sol and gel precursors can be employed for synthesizing films, nanoparticles, nanocrystals or powders.

Pechini process [35] or the citrate gel process, is the most extended variant of sol-gel method because it does not need complex chemistry reactions, nor dry atmosphere conditions. It has been historically considered within sol-gel routes because implies the formation of a gel but the precursors are chemically different. The presence of alkoxides is substituted here by the formation of a complex (chelate) between the metal ion and a carboxylic acid (typically citric acid). For this, metal salts are dissolved in water and then a carboxylic acid is added. By further addition of a polyhydroxyalcohol (typically ethylene glycol), a carboxylate gel is obtained by a condensation reaction. *Pechini* process can be performed with no addition of polyhydroxyalcohol, just dissolving metals in aqueous solution in presence of other gelificant agent as urea, and heating the solution to evaporate the water and form a gel. *Pechini* process is a simple variant widely used for obtaining oxide thin films [36,37] and fine powders of particles [38,39].

1.1.2. Metal-Organic Decomposition or Deposition (MOD)

In contrast to sol-gel process that generally uses alkoxide precursors, MOD routes employ carboxylate or β-diketonate precursors (such as acetate, propionate, 2-ethylhexanoate, citrate, neodecanoate, di-methoxy di-neodecanoate, trifluoroacetate, etc. Figure 4) that do not undergo hydrolysis or condensation reaction during preparation of metal solution. Hence, chemical interaction among different metal

precursors in solution is low and for this reason the synthesis is straightforward. The stability of these precursors comes from the fact that the carboxyl group can coordinate to metals as a bidentate ligand (see examples of acetate and acetylacetonate coordination in Figure 6).

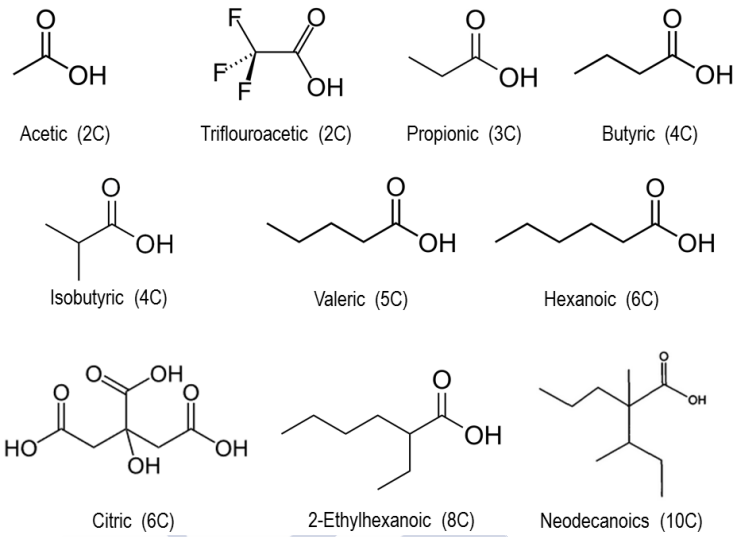

Figure 4. Some examples of carboxylic acids (lower to 10 Carbon atoms in alkyl chain), indicating in brackets their number of Carbon atoms. Their conjugate forms coordinated to metals are employed as precursors in MOD.

In order to obtain a multicomponent oxide the metal-organic compounds are dissolved in the appropriate solvent, usually their parent carboxylic acids (acetic acid, propionic acid, etc.), but also other organic solvents (alcohols, xylene, etc.), and then combined according to the final stoichiometry. Carboxylates and solvent define the rheological properties of the solution for deposition. The organic part of the precursor is removed during the subsequent thermal treatment. This route has been used for ferroelectric [40-42], high temperature superconductors [43-45], colossal magnetoresistive [46,47], photocatalytic [48], or conductive [49] oxide films.

The typical problems of MOD are defects in film due to cracking caused by premature evaporation of volatile components of the solution and decomposition of large organic ligands in the annealing step. It is a non-aqueous method that requires organic solvents due to non-polar long alkyl groups of precursors. In addition, some ligands can react with solvent to display stability problems. These drawbacks can be partially avoided by using precursors with lower organic content; as short alkyl chain (2-4 carbons) carboxylates that are soluble in water (Figure 5). Otherwise, as the chemical nature of the organic chain determines the polarity of the precursor, the use of groups containing electronegative heteroatoms (O, N,

F) promotes the solubility in water, in order to prevent the use of organic solvents. Notwithstanding, it must be considered that the hydrophobic nature of long carboxylic chain protects the metal in solution, and shorter chain length imply lower protection.

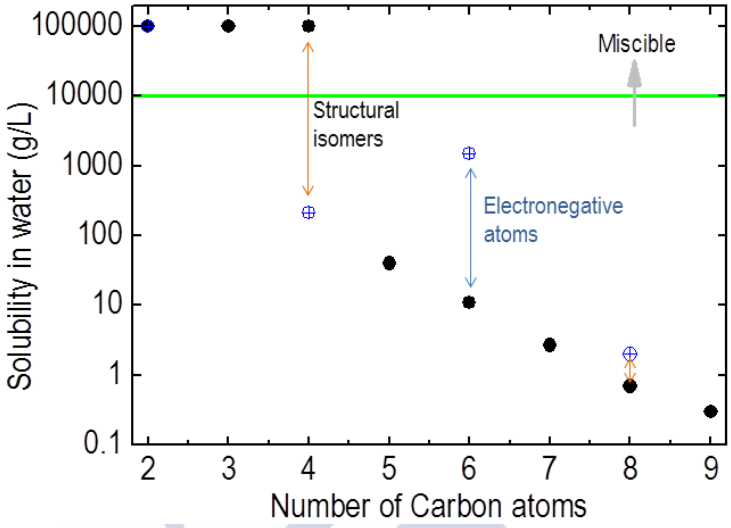

Figure 5. Solubility in water (g/L at 20ºC) for carboxylic acids as a function of the number of carbon atoms in the alkyl chain. Linear alkyls groups are represented in black dots. The marked effect of structural isomery in butyric (4C) contrast to octanoic (8C) where is negligible. The effect of introducing electronegative atoms is evidenced for citric acid (6C) where solubility is increased by 2 orders of magnitude.

1.1.3. Hybrid routes: chelate processes

These routes are commonly applied for the synthesis of multicationic materials, in which the use of different types of precursors is required, combining alkoxides and carboxylates in the same process. The objective is the modification of metal alkoxides with any additive to reduce their sensitive to moisture. According to this route, for the synthesis of a perovskite-type (ABO_3) compound, a carboxylate precursor is employed for the *A*-site cation and an alkoxide precursor is used for the *B*-site cation. The *A*-site carboxylate is first dissolved in the parent carboxylic acid or other organic solvent, with removal of water by distillation, and then the *B*-site alkoxide is added. During this synthesis alkoxides usually react with solvent (carboxylic acid) to form oligomers or chelating species.

Metal organic chelation reaction

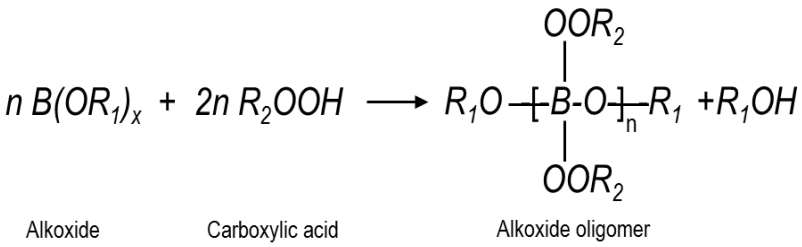

The chelation of starting alkoxides increases the stability of these precursors against the hydrolysis and can be an alternative for sol-gel method in some cases [50,51]. By this route functional polycrystalline perovskite thin films with a good control of stoichiometry can be obtained, such as $Pb(Zr,Ti)O_3$ (PZT) [52], La-doped PZT (PLZT) [53], and $(Ba,Sr)TiO_3$ (BST) [54-56].

Typically carboxylic acids (acetic, propionic, butyric or larger alkyl groups) are employed as additives, but also β-diketonates (acetylacetone) and other chelating ligands such as amine compounds or ethylenediaminetetraacetic acid (EDTA) (Figure 6) can be utilized with the objective of preventing the hydrolysis of alkoxides [57]. Chelation decreases the alkoxide reactivity in solution and under air conditions, so increasing the stability of the solution. That means that the chemical tasks (distillation, refluxing, etc.) in this route are generally less complex than those involving just alkoxides. However, the time stability of the precursor solution is still short, which limits long-term storage as further incontrollable chemical reaction and precipitation might occur [58].

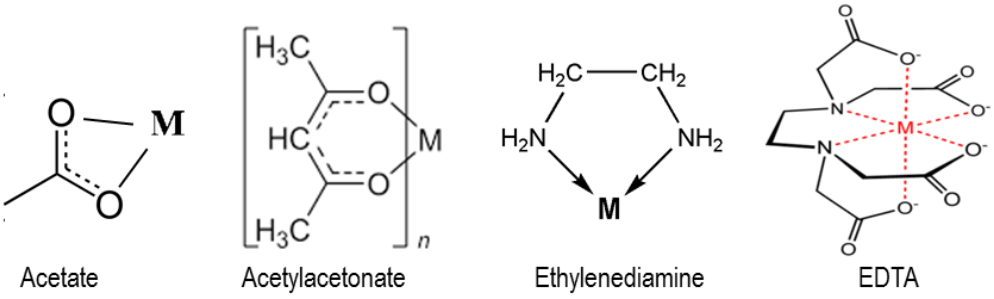

Figure 6. Some of the most typical chelating ligands, showing their coordination to metal ions.

On the other hand, the chelation process does not usually affect to all the elements presents in solution, which limits the range of compositions that can be explored by this method. Moreover, the metal distribution from these heterogeneous precursors is not uniform, resulting in phase segregation in the films

[59]. As the properties and characteristics of solution vary with time due to different reactions (chelation, esterification, polymerization, etc.), the viscosity, an important parameter in deposition, is also affected.

1.1.4. Chemical bath deposition (CBD)

The origin of CBD route dates from 19th century in which the first attempts were described in chalcogenides, particularly in PbS, to form specular films of galena in vessels [60]. More recently, a renewed interest in the synthesis of PbS films by CSD was motivated by the report of its photoconductivity activity [61].

During thin-film formation by CBD, the substrate is immersed in a solution containing the precursors (metal salts, sulfides -thiourea, thioacetamide, thiosulphate or sodium sulfide- or other chalcogenides). The formation of the film occurs by the saturation of the solution until precipitates on the substrate (Figure 7). It has been mostly directed to the synthesis of chalcogenides ME_x (E: S, Se, Te) [62-65] but can be applied also to oxides [66]. The advantages of this method are the mild temperature conditions needed for the synthesis and the possibility of coating large areas. Their main drawbacks are the requirement of relatively large volume of solution and the poor control over the thickness which is ultimately limited by the saturation concentration of the precursor solution.

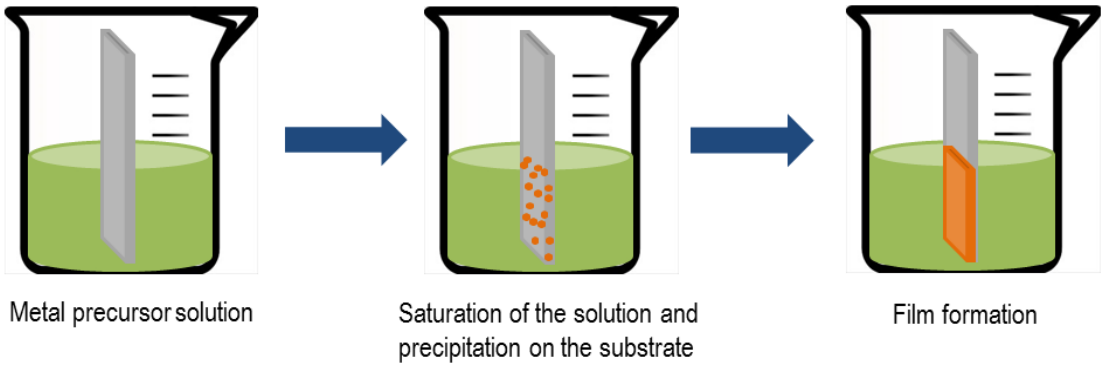

Figure 7. Schematic description of the different steps in CBD. The substrate is immersed in a solution containing the metal precursor. The film formation starts when the solution saturates and precipitates on the surface of the substrate.

1.1.5. Successive Ion Layer Absorption and Reaction (SILAR)

Among CSD techniques, perhaps SILAR [67,68] is the technique with a better control over the film thickness, which is determined by a number of successive depositions. SILAR is a simple and cost-effective technique that can operate at room temperature and ambient pressure. It is mostly employed for deposition of sulfides (Cu_xS, Ag_2S, ZnS, CdS, In_2S_3, SnS_x, PbS, As_2S_3, Sb_2S_3, Bi_2S_3, MoS_2, MnS_x, FeS_2, Co_xS_y, NiS), selenides (Cu_xSe_y, Ag_2Se, ZnSe, CdSe, In_2Se_3, Sb_2Se_3, Bi_2Se_3), and tellurides (Cu_xTe, CdTe, In_2Te_3). Deposition of metal oxides [69] thin films (Cu_2O, ZnO, MnO_2, CeO_2) is also possible by this route. The operation involves the immersion, generally by dip-coating, of the substrate in a solution containing the metal cation and then in another solution containing the chalcogenide leading to sequential reactions on the surface of the substrate (Figure 8). After every immersion the substrate is rinsed in deionized water to prevent cross-contamination. In contrast to CBD, there are no problems of solution stabilization due to precipitation, as both anion and cation precursor solutions are kept separated [70].

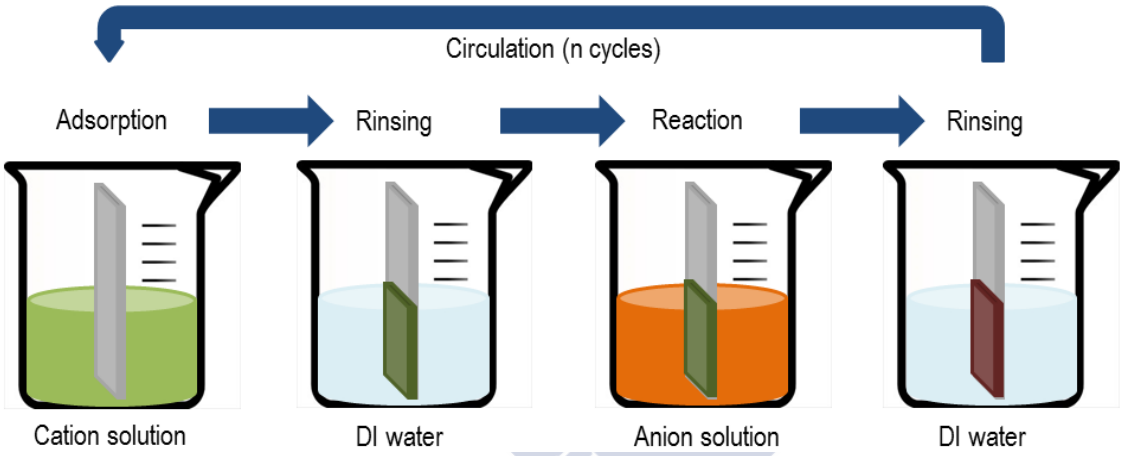

Figure 8. Schematic illustration of the deposition process in SILAR. After each immersion into solutions of reagents the sample is rinsed in deionized water. The thickness is determined by the number of successive immersions (n cycles).

However, the methods described so far result in thicker films of several hundred nanometers, and they are not suitable for producing single-crystalline thin films of a few nanometers. For this reason they are not a competitive option to physical deposition methods.

1.2. Polymer Assisted Deposition (PAD)

Polymer Assisted Deposition is an aqueous-based CSD method employed for the fabrication of thin films. PAD gathers many of the qualities mentioned for the above methods. Dense, crystalline and epitaxial oxide thin-films were initially obtained by Jia *et al*. [71-73] using PAD, showing a large improvement in the crystallinity and structural quality front most of the previously discussed chemical methods.

The processing steps are common to other CSD methods, but with some inherent particular characteristics mainly in the phase of the preparation of the solution, due to the use of a polymer to bind and stabilize the metal precursors. In the following scheme the PAD process is shown in comparison to general CSD methods:

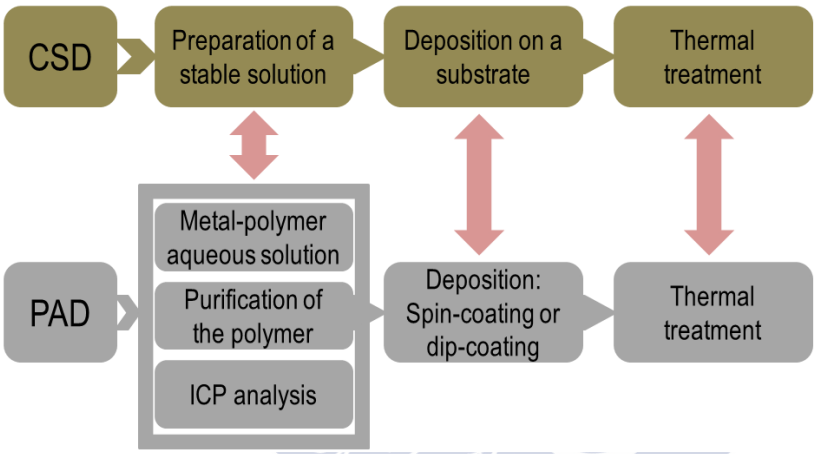

Figure 9. Comparative scheme of PAD route with respect to general CSD methods. The key part for PAD is the preparation of the metal-polymer solution.

Briefly, the description of the process is as follows (Figure 10). The first and main stage for getting inorganic thin films by PAD is to prepare stable polymer aqueous solutions of individual metal ions. Highly soluble metallic salts, such as nitrates, chlorides or acetates are dissolved in water, and stabilized in presence of a polymer. The polymer plays two important roles in the process. Firstly, it controls the viscosity of the solution, which is a fundamental parameter during spin coating or dip coating onto a substrate. On the other hand, using polymers with terminal amino groups ($-NH_2$), such as Polyethyleneimine (PEI) and their derivatives (carboxylated-PEI [PEIC] [74], phosphorylated-PEI [PPEI], sulfonated-PEI [SPEI], acylated-PEI, and hydroxylated water-soluble PEI [75]), promotes direct coordination of the metal-ions and prevents hydrolysis and other undesired reactions. The polymer to

metal interaction is mainly dominated by nucleophilic amine group attraction to cation. In a similar way than a chelate ligand, the high number of bonds in the same molecule strengthens the final complex formation. However, it is not always possible to achieve a satisfactory degree of coordination to metals. When PEI coordination to metal ions is not good enough, a chelating agent can be used to coordinate to metal in solution and then PEI stablishes interactions with the complex. EDTA is the typical ligand employed in PAD, as the negatively charged resulting complex $[EDTA\text{-}M]^{-n}$ can interact electrostatically with positively charged PEI at low enough *pH*. This combination of Metal-EDTA/PEI has been reported to produce stable precursor solutions of at least 45 different elements [72]. The appropriate choice of the metal precursor is very important to avoid problems with the counter anion. For the same reason, and in order to avoid problems of contamination with Na^+ in the films, EDTA and not its conjugate form of Na-salt must be used.

Then the precursor metal-polymer solution is filtrated in order to purify it, and metal concentration is analyzed. This solution can be concentrated to an appropriate molar value prior to deposition by spin coating or any other method suitable to produce a homogeneous polymeric film on a substrate.

The last step in film synthesis by PAD is the thermal treatment of the metal-polymer layer to obtain a crystalline thin film. During the thermal treatment, evaporation of part of the solvent, decomposition of the polymer and crystallization of the final inorganic film occur. Again, polymer plays an important role protecting the metal during early heating stage, especially in multicationic compounds preventing the formation of single metal oxides.

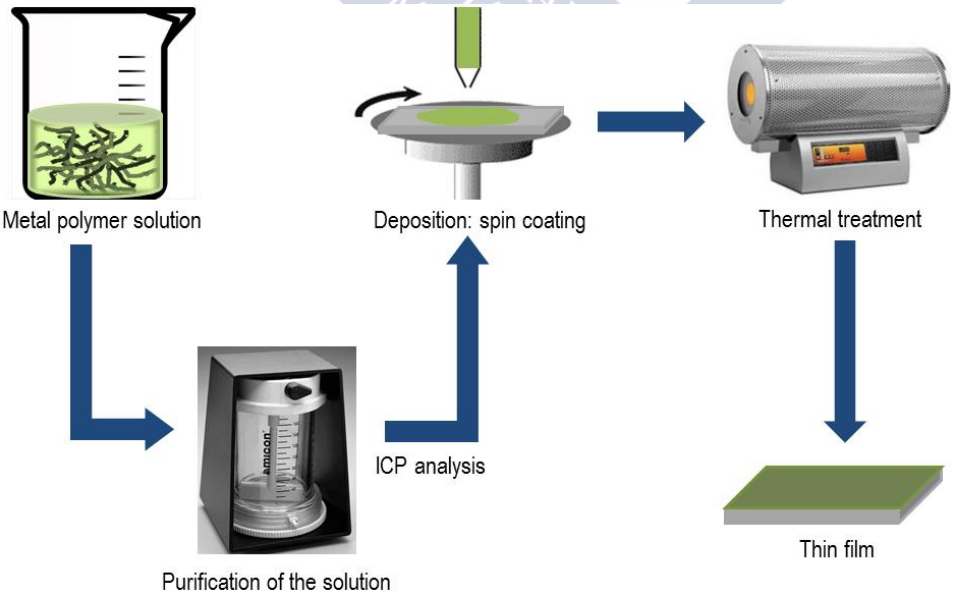

Figure 10. Graphic description of PAD process, showing the stages to reach a film from an aqueous precursor solution.

As we will demonstrate in this thesis, the step of filtration and purification of the polymer precursor solution prior to its deposition on the substrate is of crucial importance in order to obtain homogeneous thin-films.

1.2.1. PAD results

A wide range of oxide thin films have been grown successfully by PAD. Single metal oxides can be directly produced, for example: fluorescent fuel-cell electrolyte Eu_2O_3 [76], high-κ dielectric HfO_2 [77,78], MoO_x [79], photocatalyst TiO_2 [71,80], Tm_2O_3 [81], UO_2 [82,83], thermochromic VO_2 [84-86], electrochromic WO_3 [87,88], luminescent ZnO [89,90], protective ZrO_2 [91]. However, in most of these cases, only polycrystalline films were produced, obtaining similar results to other classical chemical methods like sol-gel.

A major challenge of PAD is the synthesis of complex multicationic metal-oxide films, with a good control of the stoichiometry and thickness in highly crystalline samples. Several multicationic oxide thin films have been synthesized, although a systematic study of their homogeneity and control over thickness has not been done. Some of the materials synthesized are: $La_{0.67}Ca_{0.33}MnO_3$ and $La_{0.67}Sr_{0.33}MnO_3$ [92-95], dielectric titanates $Ba_{1-x}Sr_xTiO_3$ [96-98], ferromagnetic metal $SrRuO_3$ [99], semiconducting ferromagnetic $LaCoO_3$ [100], *p*-type transparent conductive delafossites $CuAlO_2$ [101] and $CuScO_2$ [102], ferrimagnetic spinel $CoFe_2O_4$ [103], red phosphor Eu:YVO_4 [104], $BiVO_4$ [105], high mobility Ti-doped In_2O_3 (TIO) [106], or high-temperature superconducting $YBa_2Cu_3O_{7-x}$ [107-110].

Furthermore, PAD has been extended beyond oxides, for the synthesis of semiconductors, like Ge [111], some nitrides [112,113] (TiN, AlN, VN, GaN [114], superconducting NbN [115], MoN [116], and Mo_2N [117], ternaries nitrides such as $BaZrN_2$, $BaHfN_2$, and $SrTiN_2$ [118,119]) and carbides [120] (NbC [121], SiC (111) [75], UC_2 [122]).Their synthesis is more complex than for the case of oxides as they require a reactive thermal decomposition in different atmospheres: ammonia for nitrides, ethylene for carbides, and forming gas atmosphere for the case of Ge.

In most of these cases no systematic studies about homogeneity and crystal quality of the films have been performed, and so it is difficult to judge the advantages of the method over classical chemical routes.

2. Characterization of the crystal structure of thin films

2.1. Thin films and epitaxy

Thin films are a 2D-nanoscale form of a bulk material with a different surface/volume ratio, where new functionalities are possible. The stabilization of different oxide thin films with a variety of properties, and the possibility of engineering these properties by epitaxial strain have attracted an enormous attention in research community [123]. Epitaxial growth refers to the process of growing a single-crystalline film with a structural coherence, crystallographic orientation and lattice matching to the structure of the crystal substrate. The term “epitaxy” is often abused; a film growth on a different composition substrate is strictly heteroepitaxy, and an oriented film (i.e., the same crystallographic orientation) does not imply necessarily epitaxy.

The strain introduced by the substrate helps to modulate the unit of the upper film cell both in tensile or compressive way. The *mismatch* between the lattice of the substrate and the film can be quantified by a parameter, *f*.

$$f = \left(a_{film} - a_{Substrate}\right) / a_{Substrate} \times 100 \qquad (2.1)$$

Depending on the rigidity of the crystalline structure, the maximum tolerable mismatch for epitaxial growing is around $|f| < 10\%$ [124]. Compression in plane is accompanied of elongation out-of-plane, and vice versa, compensating the cell volume according to the Poisson´s ratio of the material.

Assuming an elastic behavior, and considering uniaxial stress, the relationship between the axial and transversal components of the strain is provided by the Poisson´s ratio, ν:

$$\nu = -\frac{d\varepsilon_{transversal}}{d\varepsilon_{axial}} \tag{2.2}$$

$$\varepsilon_{axial} = \varepsilon_{zz} = -\nu\varepsilon_{xx} = -\nu\varepsilon_{transversal} \tag{2.3}$$

For the case of isotropic thin film within the plane, $\varepsilon_{xx}=\varepsilon_{yy}$ (crystal lattices with tetragonal, rhombohedral, hexagonal, and cubic symmetries) the in-plane (ε_{xx}) and out-of-plane (ε_{zz}) deformation becomes:

$$\varepsilon_{zz} = -\frac{2\nu}{1-\nu}\varepsilon_{xx} \tag{2.4}$$

And the Poisson´s ratio can be easily obtained via in-plane and out-of-plane lattice constants using X-Ray diffraction techniques [125-127]:

$$\varepsilon_{xx} = \frac{a_{film} - a_{bulk}}{a_{bulk}} \tag{2.5}$$

and

$$\varepsilon_{zz} = \frac{c_{film} - c_{bulk}}{c_{bulk}} \tag{2.6}$$

In this way it can be assessed whether the film deposited on a given substrate follows an elastic deformation, given its Poisson´s ratio. In Figure 11 are shown the expected ε_{zz} values for two perovskite-type thin films of $La_{0.7}Sr_{0.3}MnO_3$ (a_{pc}=3.881 Å, ν=0.39) and $LaCoO_3$ (a_{pc}=3.80 Å, ν=0.32), two of the systems studied in this dissertation, as a function of the in-plane strain ε_{xx} produced by the mismatch of different single-crystal substrates.

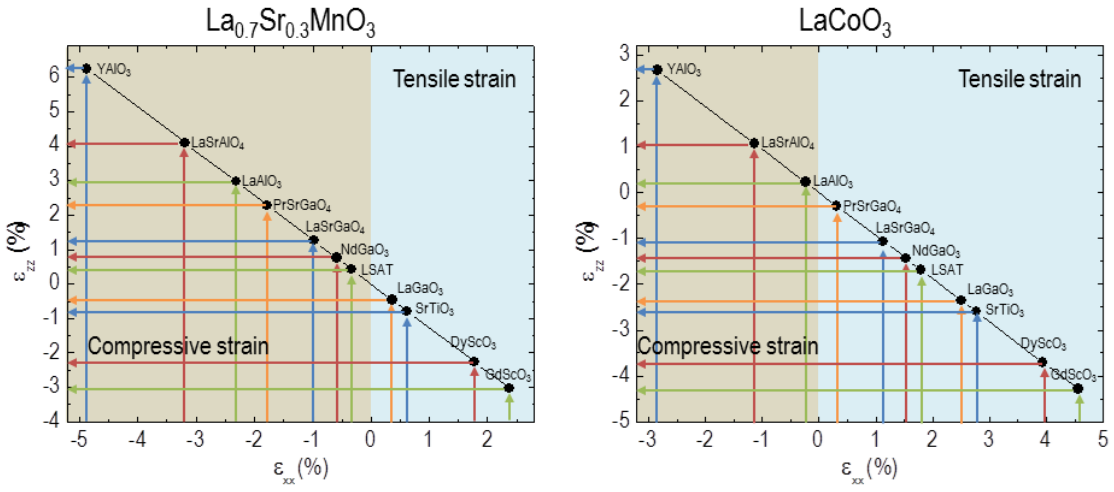

Figure 11. Out-of-plane strain ε_{zz} response in $La_{0.7}Sr_{0.3}MnO_3$ (left) and $LaCoO_3$ (right) perovskites to the in-plane strain ε_{xx} produced by the mismatch with respect to 11 different single-crystal substrates, according with their respectively Poisson´s ratios and assuming an elastic deformation.

Nonetheless, when there is a very large difference between the lattice parameters, it is still possible that an epitaxial growth occurs, since the structure of the film can fit the substrate through different strain relaxation mechanisms. In the case of perovskites (ABO_3) (Figure 12), intrinsic mechanisms like rotations and tilts of BO_6 octahedra, plus distortions of B-O bond lengths, combine with extrinsic effects like introduction of vacancies and dislocations to accommodate epitaxial stress.

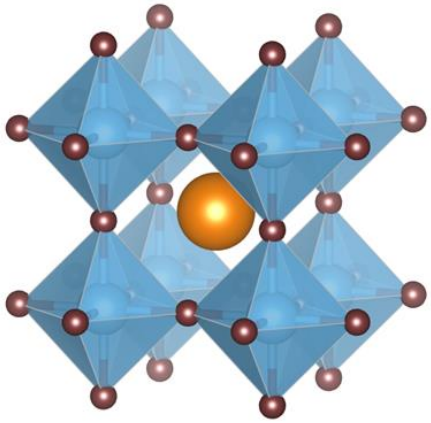

Figure 12. Ideal cubic perovskite structure (ABO_3), showing in blue the BO_6 octahedra. *A* cation occupies the central position of the cube, *B* cations occupy vertices and oxygen anions at the midpoints of the edges. In this structure the ideal bond angles *B-O-B* are 180º.

According to substrate mismatch heteroepitaxial films can grow in three different ways (Figure 13):

1. When the unit cell of the film is smaller than substrate, the film will grow under tensile stress ($f < 0$).
2. When the unit cell of the film is larger than substrate, the film will grow under compressive stress ($f > 0$).
3. Fully relaxed. It happens when there is a too much a mismatch between film and substrate, or even when the film thickness exceeds a certain threshold, beyond which the substrate strain is negligible. In these cases the film structure tends also to relax through dislocations to move closer to bulk values.

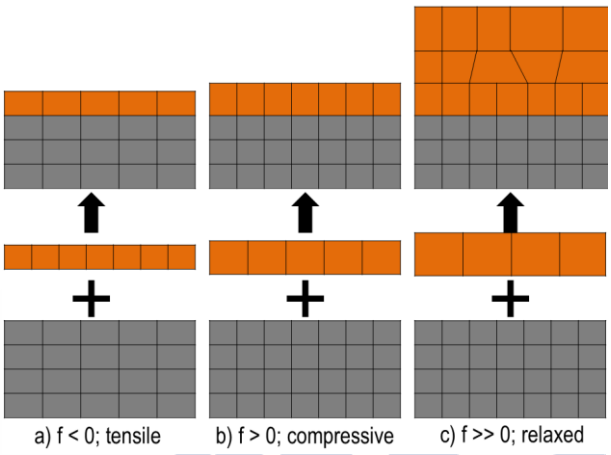

Figure 13. Schematic representation of three ways of epitaxial growing attending to lattice parameter mismatch. a) $a_{film} < a_{substrate}$; b) $a_{film} > a_{substrate}$; c) $a_{film} >> a_{substrate}$.

Many oxides adopt the perovskite structure, in which compressive and tensile strain effect is exemplified in the cartoon of Figure 14. The strain introduced has a deep impact in terms of electronic and magnetic order as it modifies the crystal field of the lattice.

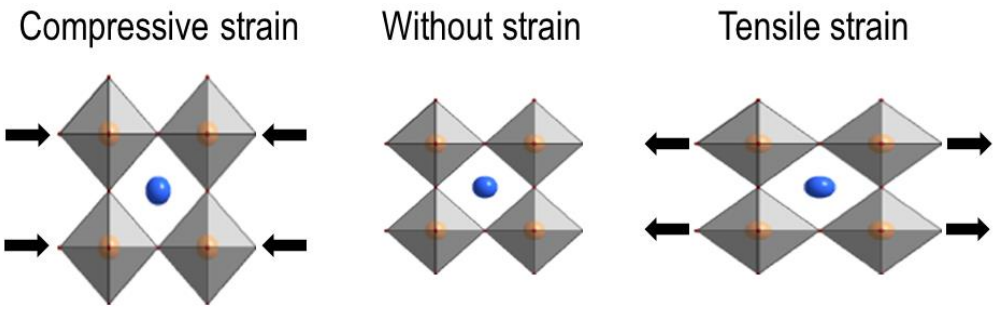

Figure 14. Schematic representation showing the effect of compressive and tensile strain onto perovskite octahedra.

Nowadays there is an increasing offer of commercially available single-crystal substrates, allowing a fine tuning of the degree of strain applied to the films [128,129]. In Figure 15 are shown the most common commercial single-crystal substrates compatible with oxide growth. The synthesis of high-temperature superconductors ($YBa_2Cu_3O_7$, $Bi_2Sr_2CuO_6$, etc.) stimulated the fabrication of many substrates. This is the reason for the abundance in the 3.8-3.9 Å range, but later, the studies on ferroelectric and multiferroic perovskites developed the production of substrates with larger lattice constants, mainly based in rare-earth scandates.

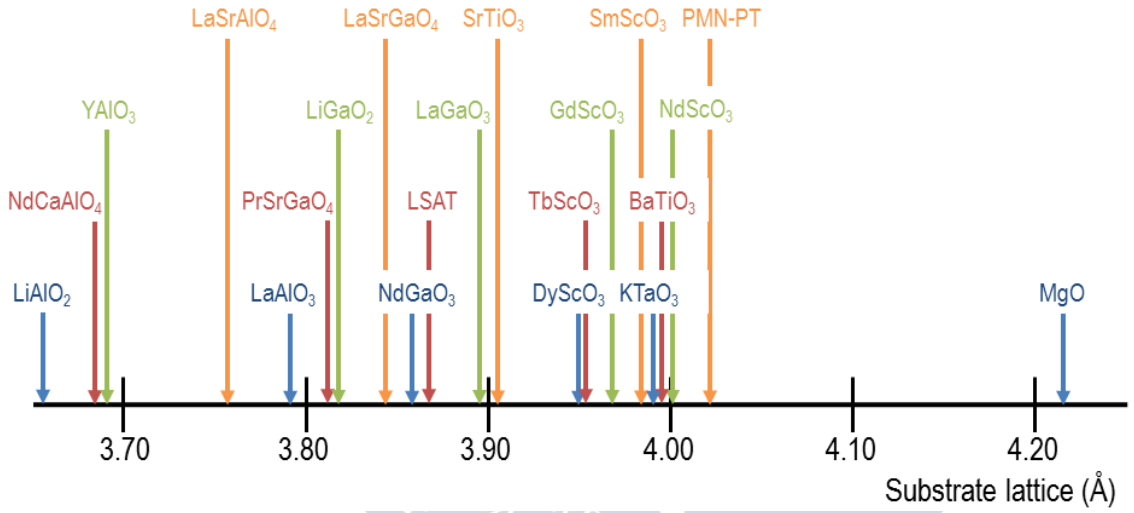

Figure 15. Commercial single-crystal oxide substrates in the range of 3.65 to 4.25 Å of in-plane lattice parameter. Lattice parameter is indicated in pseudo-cubic or pseudo-tetragonal notation in order to homogenize values. This information was obtained from the numerous companies supplying single-crystal substrates: *CrysTec GmbH, Crystal GmbH, MaTeck, MTI Corporation, Sigma-Aldrich*, etc.

2.2. X-Ray Diffraction techniques

X-Ray Diffraction (XRD) is the fundamental characterization technique for the study of the crystalline structure of thin films. The reasons are that the wavelength of X-Rays is in the order of the distance of

crystallographic planes and X-Ray techniques are nondestructive. The Bragg equation describes the conditions for X-Rays to be diffracted by crystal planes in the sample:

$$n\lambda = 2d_{hkl} sen\,\theta \tag{2.7}$$

where λ is the incidence wavelength, d_{hkl} is the distance between planes, and θ is the Bragg angle.

In this thesis, X-Rays experiments were performed with two similar diffractometers: *Empyrean* and *X`Pert Pro* from *PANalytical*, with an Euler cradle and an incidence wavelength of $\lambda\left(K_{\alpha_1}^{Cu}\right)$ = 1.540598 Å. Their basic components are a Copper anode as emission source of X-Rays, a mobile platform for the sample and a *PIXcel 3D* detector module. The optics and configuration will depend on the type of measurement to be performed.

As this equipment is a 4 circles diffractometer (*Omega, 2Theta, Chi, Phi*) with a 5 axis (*x, y, z, Chi, Phi*) sample stage, it is possible adjust the following parameters independently (Figure 16):

- *ω* (*Omega*). Incident angle.
- *2θ* (*2Theta*). Scattering angle, where *θ* is the Bragg angle.
- *ψ* (*Chi*). Tilt angle or polar angle.
- *φ* (*Phi*). Azimuth, i.e. angle of in-plane sample rotation.
- *x, y*. Displacement in the plane of the sample, *x* and *y* directions.
- *z*. Height, vertical displacement of the sample, *z* direction.

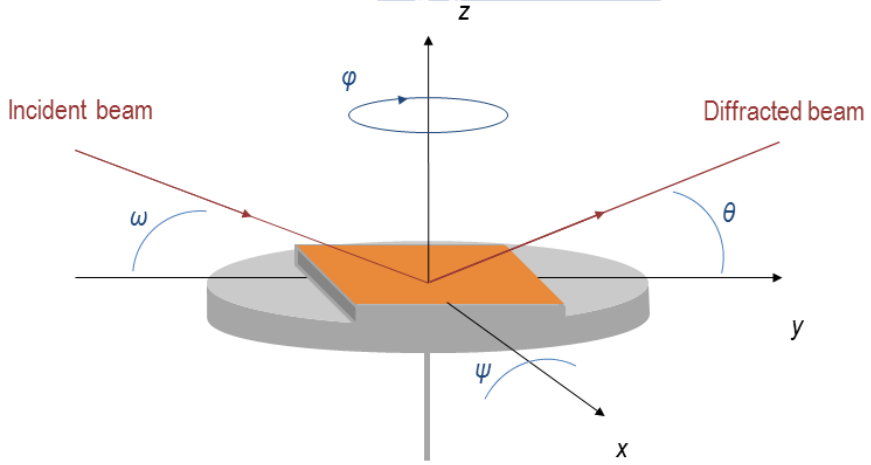

Figure 16. Illustration of the four angles *ω, θ, ψ,* and *φ* in relation to the film, as well as to the *x*, *y*, and *z* axes in the geometry of the Euler cradle in the *PANalytical* diffractometers that were used in this thesis. In this example *ω* and *θ* have the same value corresponding to a symmetric reflection.

Attending to this optics, different configurations of X-Ray source, platform, lattice planes, and detector were applied to the films. These different configurations allow a wide variety of measurements:

***θ/2θ* scan**. In this configuration both incident as exiting beams are symmetric so both ω and θ angles have the same value, and remain coupled during the scan. In this scan only those lattice planes oriented parallel to the surface contribute to a Bragg reflection. Hence, for thin films it provides information about orientation and out-of-plane lattice parameters (Figure 17). Besides, when there is a high crystalline coherence throughout the films Laue oscillations can be observed in the vicinity of the most intense Bragg diffraction peaks (Figure 17.b). Laue oscillations provide information about the size of crystalline ordered film.

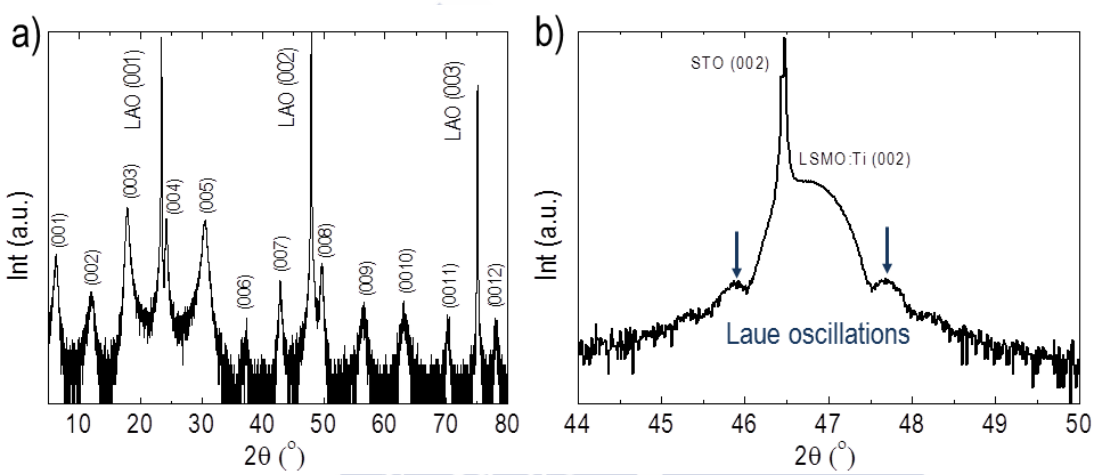

Figure 17. a) XRD pattern of 4-rock salt layer $[Bi_{1.68}Ca_2O_4][CoO_2]_{1.69}$ misfit cobaltate on $LaAlO_3$ (001) substrate synthesized in this thesis. Only the (*00l*) reflections, parallel to surface, are observed, indicating that the film is single phase and aligned along the *c*-axis. From this *θ/2θ* scan is obtained the out-of-plane lattice parameter of this cobalt oxide, *c* =14.89 (2) Å. Further discussion about these results is given in chapter 8. b) XRD pattern of an 18 nm thick $La_{0.7}Sr_{0.3}Mn_{0.95}Ti_{0.05}O_3$ film on $SrTiO_3$ (001) obtained by PAD during this thesis, in which Laue oscillations are observed around substrate and film (002) reflections. Both XRD measurements were carried out in an *Empyrean* diffractometer with a 2-bounce Ge (220) monochromator and a Parallel plate collimator of 0.18º with ¼º slit.

For the easier case of a cubic (or pseudo-cubic) structure the lattice parameter can be directly obtained combining Bragg equation and the interplanar spacing for a given Miller index (*hkl*):

$$d_{hkl} = \frac{a}{\sqrt{h^2 + k^2 + l^2}} \Rightarrow a = \frac{\lambda\sqrt{h^2 + k^2 + l^2}}{2sen\theta} \qquad (2.8)$$

This configuration is the most used in routine characterization of thin films and the optics is variable attending to the characteristics of films, as thickness. Typically, we employed the emission module with a 2-bounce Ge (220) monochromator, a fixed mask slit of 2 mm, ¼º slit and the *PIXcel 3D* detector with a Parallel Plate Collimator (PPC) of 0.18º (Figure 18).

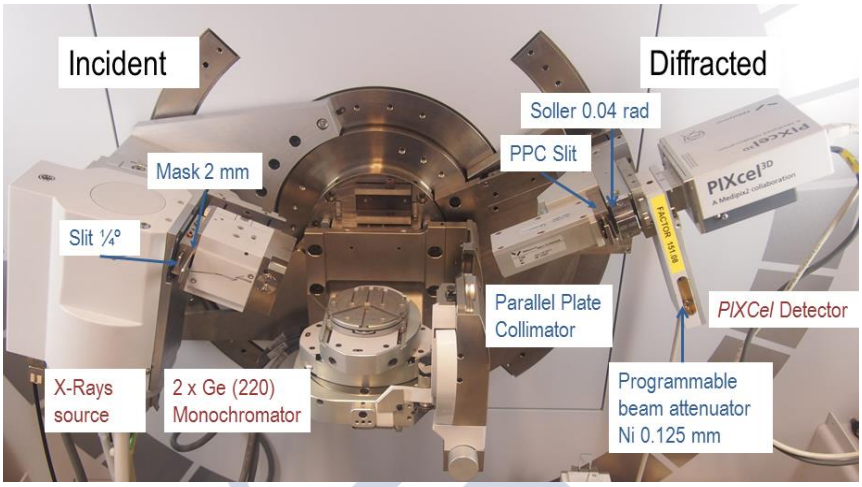

Figure 18. *θ/2θ* configuration in a *PANalytical Empyrean* diffractometer.

For those cases in which a more detailed measurement is required (e.g. around a characteristic reflection but not all the pattern) or when the film is very thin (a few nanometers), a High Resolution Optics is recommended (Figure 19).

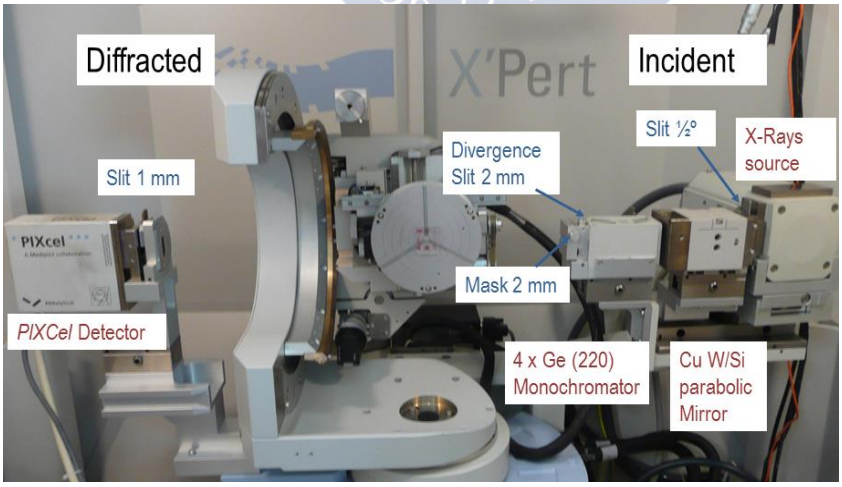

Figure 19. High Resolution configuration in a *PANalytical X`Pert Pro* diffractometer. This optics is especially useful for increasing the signal/noise ratio in ultrathin films. In this optics the alignment of the direct beam must be very accurate to maximize the intensity.

Rocking curve or *ω* scan. It consists in a *ω* (incidence angle) scan around a fixed *2θ* value (diffraction angle) of a particularly intense peak (usually those oriented to the substrate with a low index value). In this configuration *ω* is decoupled to *θ*. It provides information about the degree of crystallinity, texture, and mosaicity, attending to the Full Width at Half Maximum (FWHM). The lower the FWHM value the higher the film crystallinity; for single-crystals the FWHM value is usually less than 0.1º (Figure 20). The optics is very similar to these for *θ*/*2θ* scans.

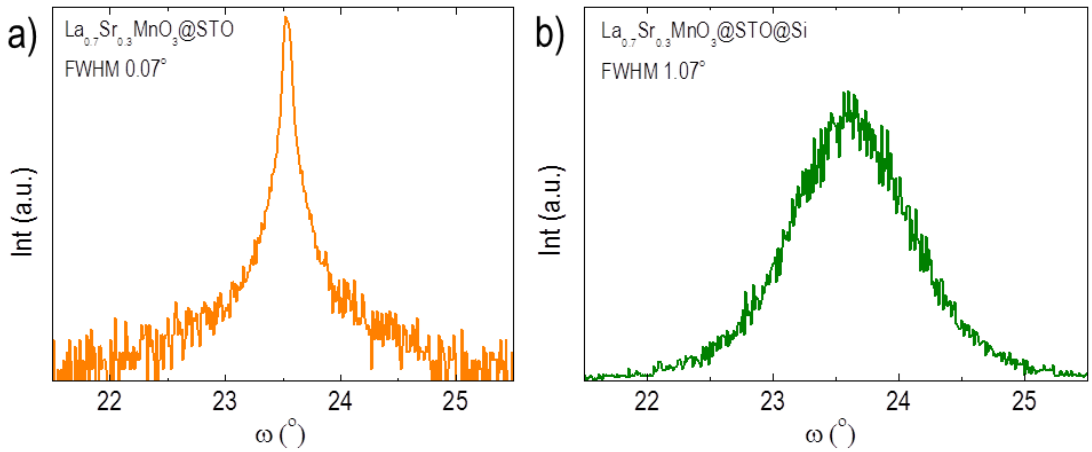

Figure 20. Rocking curves from the (002) $La_{0.7}Sr_{0.3}MnO_3$ peak for a film growth on single-crystal STO (a) and for another integrated on Silicon (b). Both films were deposited by PAD from 0.20 M concentrated solutions. The crystallinity quality of single-crystal film is two orders of magnitude higher with respect to that deposited on Si. It should be noted that single-crystal film is represented in logarithmic scale while that integrated in Si is in linear scale in order to be shown in the same figure. Rocking curve measurements were carried out in an *Empyrean* diffractometer with a 2-bounce Ge (220) monochromator and a PPC of 0.18º with ¼º slit.

Azimuthal or *φ* scan. The measurement consists in a 360º scan in *φ* around an oblique plane that contains both in-plane and out-of-plane components, usually (*h0l*) reflections (Figure 21). That means that the scan is fixed to an asymmetric Bragg peak with a certain tilt (*ψ*). It differs from a pole figure in that this is a mapping on *φ* and *ψ*. In order to compare their relative crystallographic relation (in-plane alignment and crystallographic axis between film and substrate) each azimuthal scan involves two different scans, one for the substrate and another for the film. The optics for this purpose is similar to above examples, with special attention to divergence and detector slits for low intense signals.

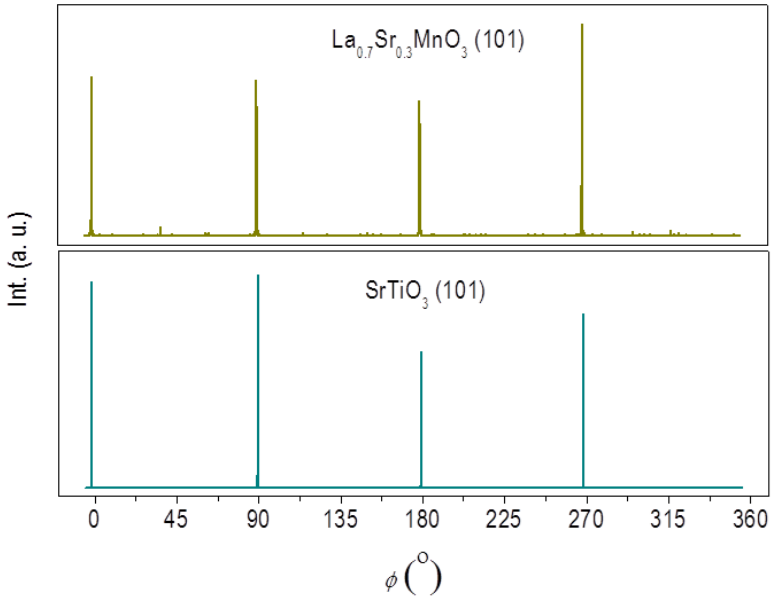

Figure 21. φ scan of the (101) reflection for the STO substrate and a PAD $La_{0.7}Sr_{0.3}MnO_3$ film from 0.20 M concentrated solution. Just 4 sharp peaks spaced 90º are observed in both scans, confirming the cube-on-cube epitaxial relationship due to the same maximum intensity positions. Phi scans were carried out in an *Empyrean* diffractometer with a 2-bounce Ge (220) monochromator and a PPC of 0.18º with ¼º slit.

Reciprocal Space Map (RSM). It displays an image in two dimensions around a reflection containing substrate and film which provides information about out-of-plane and in-plane lattice parameters, and the strain relationship between film and substrate (Figure 22).

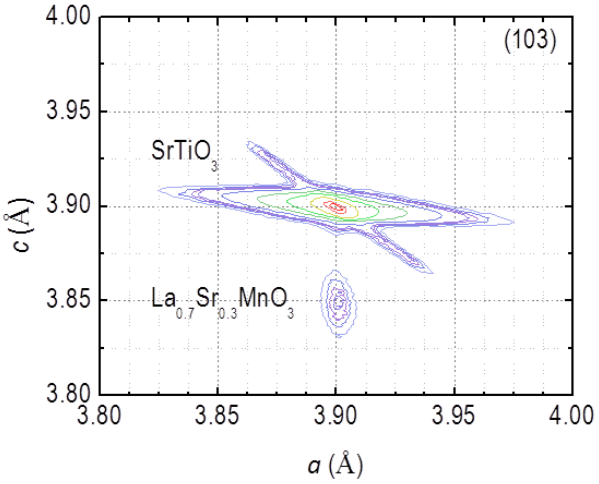

Figure 22. XRD RSM around the (103) reflection for a PAD-deposited $La_{0.7}Sr_{0.3}MnO_3$ film from 0.20 M concentrated solution on STO (001). Reciprocal lattice vectors (Q) were transformed to lattice units

according to equations (2.11) and (2.12). As it can be observed the film is matched to the substrate (same in-plane lattice parameter). Further discussion about these results is given in chapter 5. RSM was carried out in an *Empyrean* diffractometer with a 2-bounce Ge (220) monochromator with ½º slit. The detector was full open (255 channels) in Scanning Mode at Static line (1D) with the *PIXcel* tube with a 7.5 mm Anti-scatter slit.

A RSM records a series of 2θ scans for a given range of values of ω (keeping ψ and φ fixed) around an asymmetric reflection containing substrate and film peaks. The reciprocal lattice vectors parallel to the surface Q_x and perpendicular to the surface Q_z are obtained from the relationship between the incidence and exiting angles through the equations:

$$Q_x = \sin\theta.\sin(\theta - \omega) \tag{2.9}$$

$$Q_z = \sin\theta.\cos(\theta - \omega) \tag{2.10}$$

In a cubic system the out-of-plane (c) and in-plane (a) lattice parameters are calculated directly from the reciprocal lattice vectors by the following equations:

$$a = \frac{\lambda\sqrt{h^2 + k^2}}{2Q_x} \tag{2.11}$$

$$c = \frac{\lambda.l}{2Q_z} \tag{2.12}$$

where λ is the wavelength and h, k, and l are the Miller reflection indexes for a given peak.

Due to these scans are applied to weak diffraction peaks the optics for RSM measurements tends to maximize the signal by increasing both intensity and detector range. An example of a RSM configuration is shown in Figure 23.

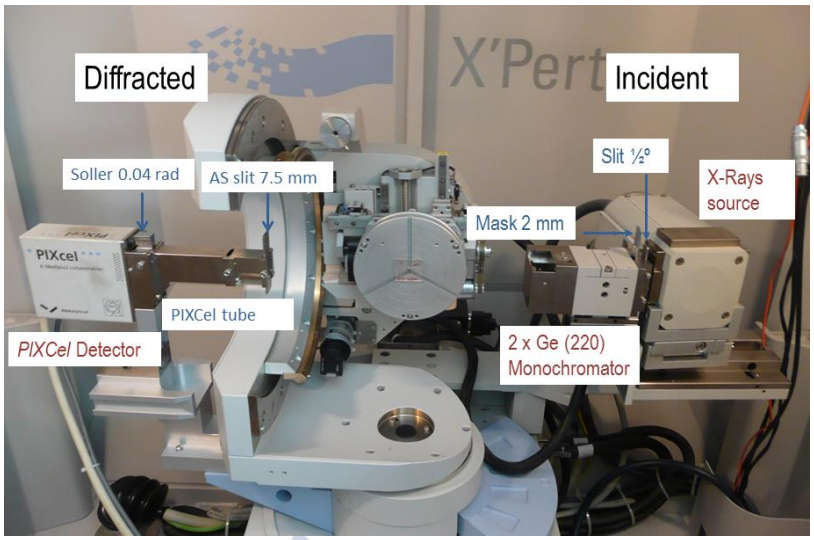

Figure 23. RSM configuration in *PANalytical X`Pert Pro* diffractometer. The detector is activated in Scanning Mode at Static line detector (1D) with the full open detector (255 channels).

RSM can be applied to phase structural distinction by analyzing half-order reflections. Deposition and growing conditions can distort the crystallographic lattice of the film from the typical bulk state. Studying the presence or absence of characteristic reflections for different crystal systems (monoclinic, rhombohedral, cubic, tetragonal, or orthorhombic) by mappings around their theoretical positions is a valuable tool for identifying the crystal structure of a film (Table 1 and Figure 24). Moreover, this RSM study can provide additional information in the form of satellites indicating the existence of diffuse scattering or higher-order periodicity in a film.

(h/2 k/2 l/2)	C2/c	R-3c	c⊥-Pbnm	c//-Pbnm
(1/2 1/2 1/2)	✓	×	✓	✓
(1/2 1/2 3/2)	✓	✓	✓	✓
(1/2 0 1)	×	×	×	✓
(1 0 1/2)	×	×	✓	×

Table 1. Characteristic half-order reflections for monoclinic (*C2/c*), rhombohedral (*R-3c*), and orthorhombic (*Pbnm*) symmetries for $La_{0.7}Sr_{0.3}MnO_3$.

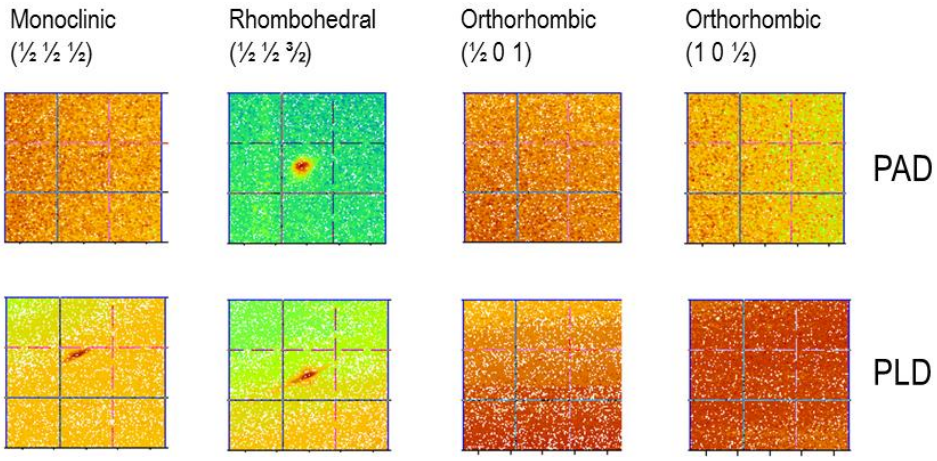

Figure 24. RSMs for some characteristic half-order Bragg reflections in $La_{0.7}Sr_{0.3}MnO_3$ films prepared by PAD (top) and PLD (bottom), respectively. In this example, the presence of a reflection at (1/2 1/2 3/2) in PAD film is compatible with rhombohedral system (R-3c), while in PLD film the observation of a signal around (1/2 1/2 1/2) and (1/2 1/2 3/2) is consistent with a monoclinic C2/c symmetry. Further discussion about these results is given in chapter 5. RSMs were carried out in an *Empyrean* diffractometer with a 2-bounce Ge (220) monochromator with ½ºslit. The detector was full open (255 channels) in Scanning Mode at Static line (1D) with the *PIXcel* tube with a 7.5 mm Anti-scatter slit.

In-plane measurements. With this analysis it is possible to observe those planes perpendicular to surface (*h00*) or (*hk0*) that are not accessible by traditional Bragg-Brentano configuration (Figure 25).

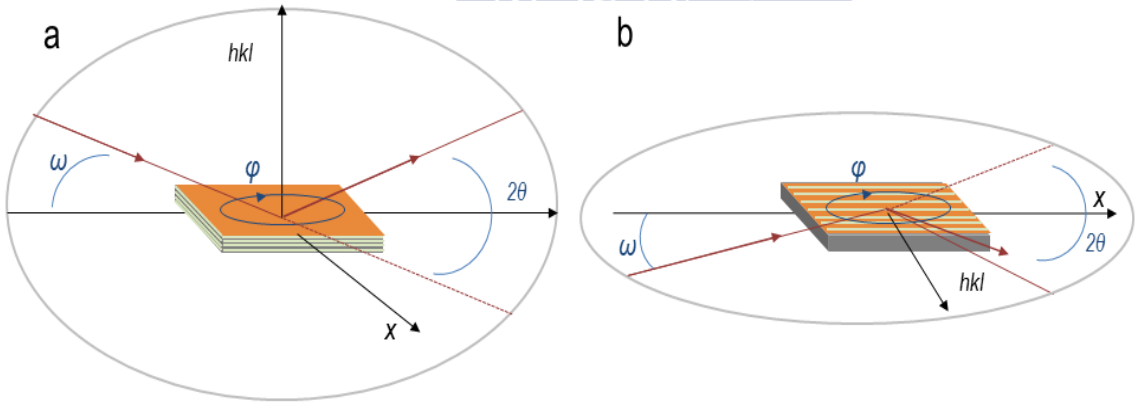

Figure 25. Principal coplanar components in a) Bragg-Brentano and b) In-plane geometries. The plane containing incident and diffracted beams is called diffraction plane. At In-plane geometry *ω* and *φ* can be used indistinctly.

This provides information regarding to the coherence of film growing to respect to the substrate, mosaicity and the presence of any mechanism of strain relaxation.

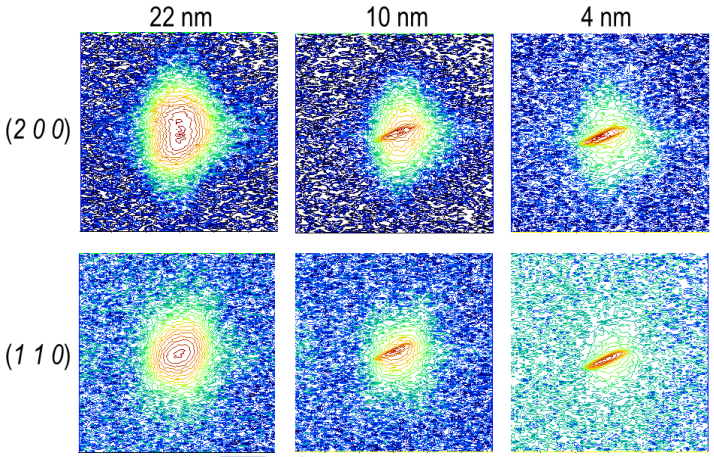

Figure 26. RSMs around (200) (top) and (110) (bottom) Bragg reflections taken at in-plane geometry for $La_{0.7}Sr_{0.3}MnO_3$ films prepared by PAD. The films show a high structural coherence with the substrate, with the same in-plane lattice parameter, along the thicknesses (22, 10, and 4 nm). Further discussion about these results is given in chapter 5. In-plane RSMs were carried out in *X`Pert Pro* diffractometer with a parabolic mirror with ½º slit and 2mm mask fixed slit. PPC of 0.27º with Ni filter was used at diffracted path.

In this configuration both incidence as diffracted beams are parallel to the surface of the sample and the optics must be adapted to the grazing incidence and diffracted conditions. Moreover, in this arrangement the beam depth penetration is limited to 100 nm, in contrast to usual configuration in the 10-100 μm range, and the superficial layers have a higher contribution to diffraction in comparison with the substrate. For that reason a PPC must be used in order to filter the diffracted beam before the entering to the detector (Figure 27).

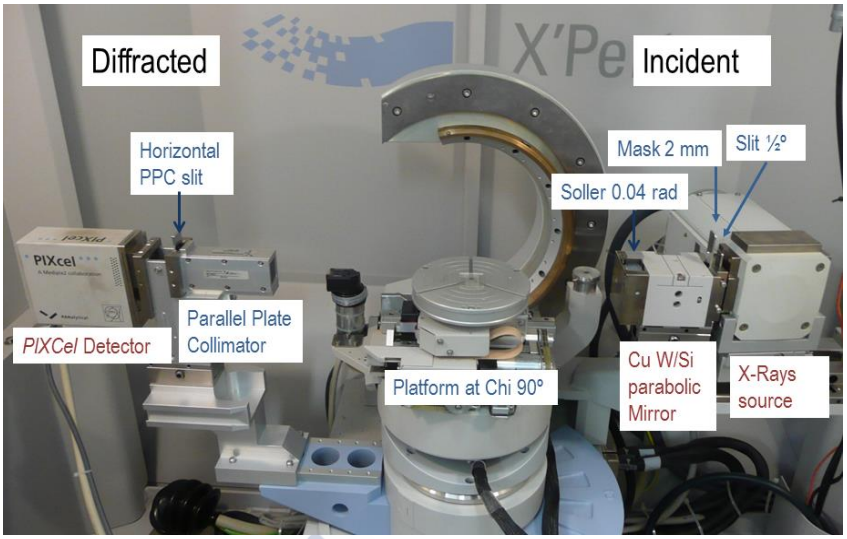

Figure 27. In-plane configuration in *PANalytical X`Pert Pro* diffractometer. PPC module is installed for receiving grazing diffraction. The platform is collocated perpendicular (ψ = 90º) to the convectional position. In this configuration φ can be rotated for larger angles and ω for smaller ones (up to 2º).

X-Ray Reflectivity (XRR). XRR is a characterization technique that uses X-Rays scattering, it does not measure the diffracted signal but the reflected radiation at very small incidence angles. XRR provides information on density, thickness and roughness (surface and interface). Because XRR is not based on diffraction the investigated film may be not only crystalline but also amorphous, what implies the possibility of investigating polymeric layers deposited by PAD previous to thermal treatment. It consists in a $\omega/2\theta$ scan in symmetric configuration, in a similar way to a typical $\theta/2\theta$ scan, but at very small angles. Below a critical incidence angle θ_c the X-Rays are completely reflected leading to a total external reflection, above this critical angle (depending on the material density) the beam penetration increases and due to interference phenomena of the scattered X-Rays the curve shows characteristic intensity oscillations. These oscillations, which are called Kiessig oscillations or Kiessig fringes, come from constructive and destructive interferences of the wavelength and provide information about the film thickness. Specifically, the period of those fringes is inversely related to the film thickness. The slope of the XRR curve is related to the film roughness, so a marked slope means high roughness (Figure 28).

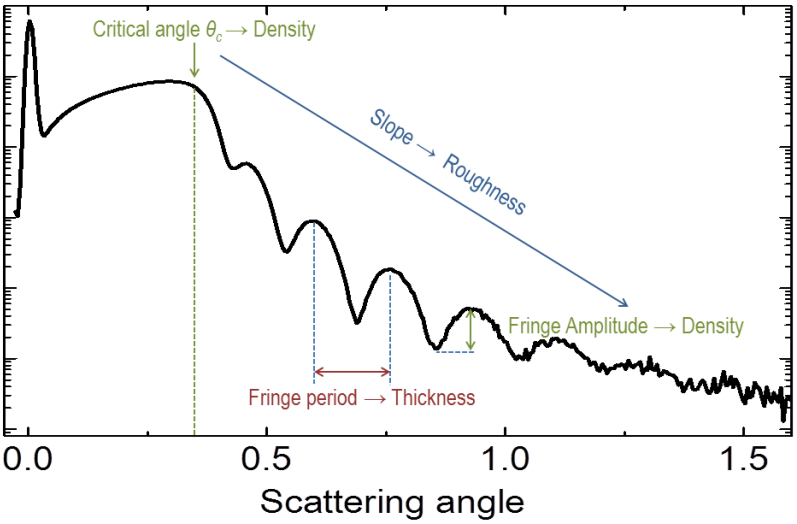

Figure 28. XRR curve showing the structural parameters that can be obtained from a thin film measurement. The data corresponds to a 23 nm thick $BiFeO_3$ film on STO (001) obtained by PAD during this thesis. The XRR measurement was carried out in an *Empyrean* diffractometer with a 2-bounce Ge (220) monochromator and a PPC of 0.18º.

These are the main X-Ray scattering techniques for the characterization of epitaxial thin films and in particular XRR, $\theta/2\theta$ scan, and RSM were used as routine analysis in this thesis. More information for other X-Ray analysis, other applications, and the analysis of polycrystalline or amorphous materials can be found in detail elsewhere [130].

3. Characterization and optimization of the relevant chemical aspects of the precursor solution for the synthesis of thin films

Chemical aspects involving polymer structure and its function are studied in this section. Particularly, we will focus on the structure of PEI, coordination to different metals and complexes, and thermal degradation. The process of preparation of thin film from solution is described, explaining the different steps involved. This process depends mainly on the stabilization of metal polymer solution, which can vary according to the metal properties. Once this part of the procedure is finished, the material to be obtained defines the experimental conditions of synthesis.

3.1. Characterization of Polyethylenimine (PEI)

PEI is a hydrosoluble polymer composed of amine groups with a variable degree of branching and molecular weight. Although in linear PEIs just secondary amines are present (Figure 29.a), most of commercial PEIs are branched polymers with primary, secondary, and tertiary amines in different ratio (Figure 29.b). The amount of respective type of amines is depending on the degree of branching derived from the use of crosslinking agents during the polymerization of aziridine precursor.

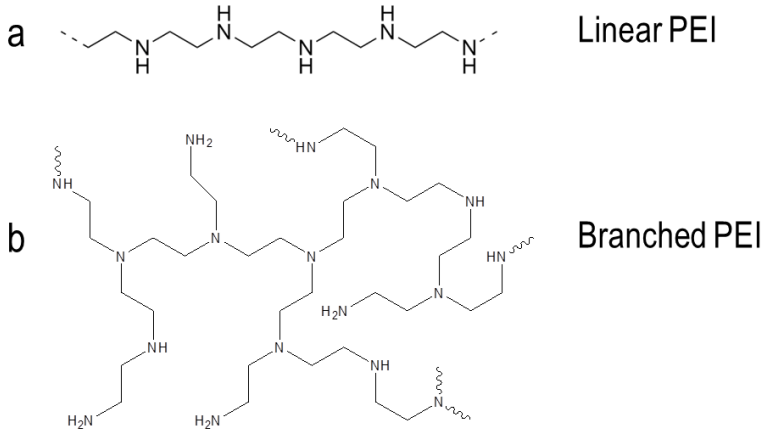

Figure 29. a) Chemical structure of linear polyethylenimine (PEI) and b) simplified structure of a typical branched PEI.

The degree of branching and molecular weight distribution of different commercial PEI was determined by Nuclear Magnetic Resonance ^{13}C-NMR and ^{1}H-NMR. For this study two different commercial PEIs were compared, with different molecular weight and degree of ramification: *Sigma Aldrich* PEI (SA-PEI) Cat. No. 408727 (Lot No. MKBG4206V), commercialized as "branched" and *Supelco Analytical* PEI (SU-PEI), Cat. No. 21195-U (Lot No. 10577).

Even though in principle both ^{1}H NMR and ^{13}C NMR may be used to investigate the molecular architecture, the better separation of the signals in the ^{13}C NMR spectra permitted a more precise quantification of the degree of branching. The 8 different methylene groups in the N-CH_2-CH_2-N repeating units give signals in the range 40-60 ppm, whereas no other significant signals were disclosed (Figure 30). The spectra were recorded using inverse-gated decoupling sequence [131] to avoid any influence of the Nuclear Overhauser Effect (NOE), that transfers nuclear spin polarization from one population to another near via cross-relaxation due to the application of a radiofrequency in the electron spin rate. This sequence enabled the determination of the ratio of the different amine groups from the area of the signals, *S*:

$$1º:2º:3º = (S_7+S_8):(S_4+S_5+S_6)/2:(S_1+S_2+S_3)/3 \quad (3.1)$$

where the index refers to the methylene groups as numbered in Figure 30. The percentage of primary, secondary and tertiary amino groups was: 1º:2º:3º=39:37:24 for SU-PEI and 31:35:34 for SA-PEI. The degree of branching, defined as the ratio of 2º/3º amines (the ratio of linear to branched structures), being 1.54 for SU-PEI and 1.03 for SA-PEI.

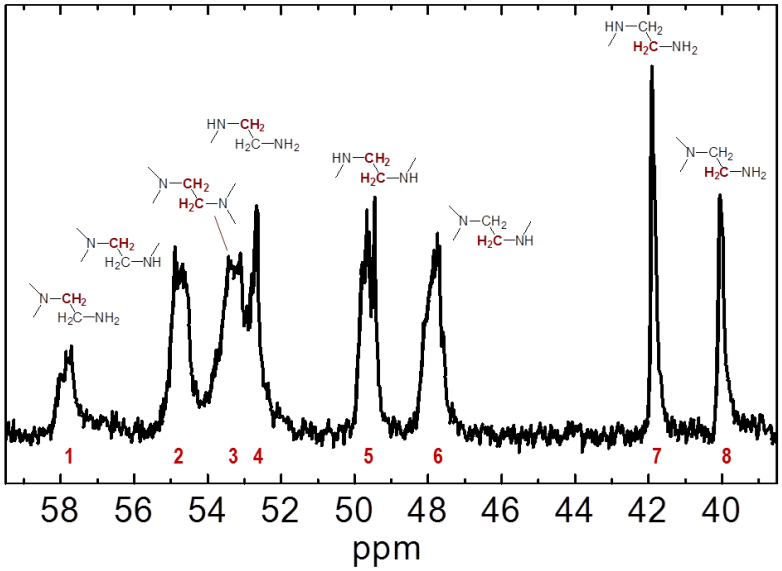

Figure 30. Inverse-gate ^{13}C NMR spectrum of SU-PEI in D_2O. NMR spectra were recorded from 50 mg samples dissolved in 0.8 mL D_2O in a *Bruker DRX-500* operating at 500 or 125 MHz for ^{1}H or ^{13}C NMR, respectively. 1D inverse-gate ^{13}C spectra were acquired under quantitative conditions using a low angle ^{13}C pulse of 30º and an inter-scan delay of 3 s (d_1= 2 s and a free-induction decay acquisition time = 1 s), with 10^4 scans in 8.3 h.

The lower degree of branching for SU-PEI in comparison with those reported for other commercial PEIs [132] may be due to the method of synthesis employed to obtain polymer molecules of higher molecular weight [133], which is related to addition of polyfunctional branching agents (dichloroethane or epichlorohydrin) [134] during their preparation (Figure 31).

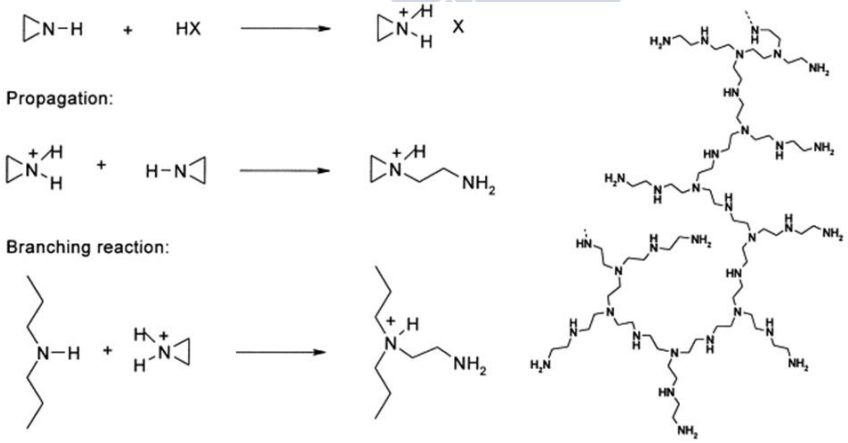

Figure 31. Acid-catalyzed ring-opening polymerization of aziridine leads to branched PEIs. Tertiary, secondary, and primary amines corresponds to branching, chain extension, and termination points, respectively.

Notwithstanding such structural differences from NMR, the chemical behavior of aqueous solutions of both types of PEIs does not reveal significant differences. Acid potentiometric titrations of aqueous solutions of SU-PEI and SA-PEI showed very similar results with three protonation constants; the pK_a for primary, secondary and tertiary amines being ≈10.5, ≈6.4 and ≈4.2, respectively (see Figure 32). Titrations were recorded at room temperature using polymer solutions at initial basic conditions enhanced with the addition of a strong base, NaOH (*pH* 12) and titrated with HCl 1.2 M in 0.006 mL additions. From this analysis is deduced the similar *pH*-dependence behavior of SU-PEI and SA-PEI in metal solution.

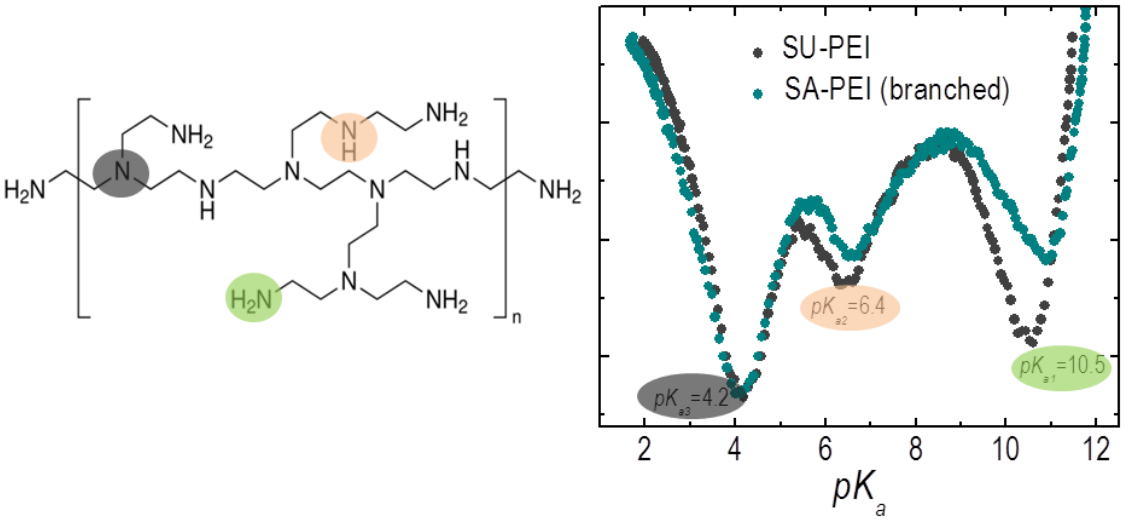

Figure 32. Derivative of the titration curves for both PEIs analyzed in this work representing the position of the three types of amines in polymer structure. Acid titrations were performed from 65 mg samples dissolved in 25 mL H_2O in a *Crison pH*-meter. Before the measurement, *pH* of polymer solutions was increased to 12 (alkaline conditions) by adding NaOH. Titrations were recorded at 25 ºC with HCl 1.2 M.

We want to remark that we have not found any difference in the final results (quality of the films) using either SU-PEI or SA-PEI.

3.2. Metal polymer solutions

To prepare a precursor solution of a given individual cation, the corresponding salt is dissolved in water, along with EDTA and PEI. The *pH* is accordingly adjusted so most of the primary and secondary amine groups of PEI are protonated to form the EDTA-Metal complex.

The electrostatic interactions of the protonated amino groups of PEI with the $[EDTA\text{-}Metal]^{n-}$ complex (Figure 33) are crucial for further successful deposition of an homogeneous film. PEI in protonated conditions can establish hydrogen bonding and electrostatic interactions with an anionic metal complex $[EDTA\text{-}Metal]^{n-}$. The strength of these interactions is weaker than covalent bonds, but the huge number of these weak interactions provides a very stable situation. In this direction, the use of EDTA, the more common chelate ligand, tends to improve the yield in those cases in which a direct bonding between PEI and metal is too weak. Besides, varying the ratio EDTA:PEI is an alternative to modify the *pH* without using additional acids or bases.

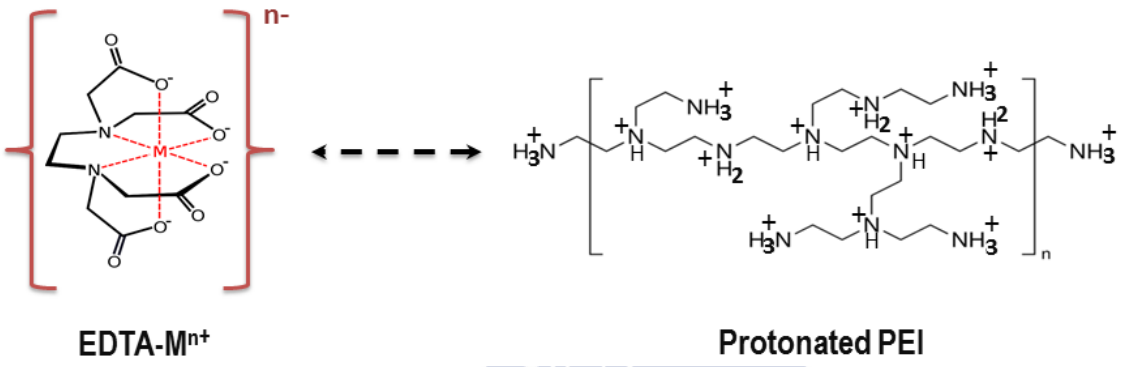

Figure 33. EDTA metal complex and PEI with all amines forms (primary, secondary, and tertiary) protonated.

Most of metal polymer solutions are prepared directly from water soluble metallic salts (nitrate, chloride, acetate, oxalate, etc) dissolved with EDTA and PEI in deionized water. The commercial metal precursors used throughout this thesis are listed in Table 2.

Ion	Precursor	Mm (g/mol)	CAS Number	Appearance
Ca^{2+}	Calcium nitrate. $Ca(NO_3)_2.4H_2O$ (*Alpha Aesar*, 99.0%)	236.15	13477-34-4	Colorless solid
Sr^{2+}	Strontium nitrate. $Sr(NO_3)_2.4H_2O$ (*Fluka*, 99.0 %)	283.69	10042-76-9	White granular solid
Ba^{2+}	Barium nitrate. $Ba(NO_3)_2$ (*Aldrich*, 99.0%)	261.34	10022-31-8	White powder
Ti^{4+}	Titanium tetrachloride. $TiCl_4$ (*Sigma-Aldrich*, d=1.73 g/cm^3)	189.68	7550-45-0	Colorless liquid
V^{5+}	Sodium metavanadate. $NaVO_3$ (*Aldrich*, 99.9 %)	121.93	13718-26-8	Yellow crystalline solid
Mn^{2+}	Manganese nitrate. $Mn(NO_3)_2.6H_2O$ (*Alpha Aesar*, 98.0 %)	286.94	17141-63-8	Pale pink crystals
Fe^{2+}	Iron oxalate. $FeC_2O_4.2H_2O$ (*Aldrich*, 99.99 %)	179.89	6047-25-2	Yellow powder
Fe^{3+}	Iron nitrate. $Fe(NO_3)_3.9H_2O$ (*Aldrich*, 98.0 %)	404.00	7782-61-8	Pale violet crystals
Co^{2+}	Cobalt nitrate. $Co(NO_3)_2.6H_2O$ (*Aldrich*, 98.0 %)	291.03	10026-22-9	Red crystalline
Zn^{2+}	Zinc nitrate. $Zn(NO_3)_2.6H_2O$ (*Sigma-Aldrich*, 99.0 %)	297.49	10196-18-6	White crystals
Ir^{3+}	Iridium chloride. $IrCl_3.xH_2O$ (*Sigma-Aldrich*, reagent grade)	298.58	14996-61-3	Dark green solid
La^{3+}	Lanthanum nitrate. $La(NO_3)_3.6H_2O$ (*Fluka*, 99.0 %)	433.01	10277-43-7	White crystalline solid
Pr^{3+}	Praseodymium nitrate. $Pr(NO_3)_3.6H_2O$ (*Sigma-Aldrich*, 99.9 %)	435.01	15878-77-0	Green crystals
Al^{3+}	Aluminium nitrate. $Al(NO_3)_3.9H_2O$ (*Sigma-Aldrich*, 98.0 %)	375.14	7784-27-2	White crystals
Bi^{3+}	Bismuth nitrate. $Bi(NO_3)_3.5H_2O$ (*Alpha Aesar*, 99.999%)	485.07	10035-06-0	White powder
B^{3+}	Sodium tetraborate. $Na_2B_4O_7.10H_2O$(*Sigma-Aldrich*, 99.0 %)	381.37	1303-96-4	White solid
Ge^{4+}	Germanium dioxide. GeO_2 (*Aldrich*, 99.99 %)	104.64	1310-53-8	White powder

Table 2. Precursors employed during this thesis for obtaining different polymer solutions. The commercial source, as well molar mass, Chemical Abstracts Service (CAS) Number, and appearance of reagents are also indicated.

Usually, PEI is dissolved in water firstly obtaining a basic solution of *pH* ≈10.7. The subsequent addition of EDTA decreases the *pH* to a value which depends on the EDTA:PEI ratio (1:1 *pH*≈6.6; 1:2 *pH*≈9.1). It is important to remark that the order of dissolving the components is very relevant: starting with a basic solution of water PEI favors the solubility of EDTA.

The solution of around 100 mL is kept under continuous stirring and heated at 50ºC during several hours to ensure complete dissolution of the salt, polymer and EDTA. For most of metals, the complexation is very good and they do not show undesired hydrolysis reactions at the final *pH* of the solution. However, there are some cases in which it is very important to control the *pH* to increase the complex stabilization and to prevent hydrolysis of cations. For example, Ti^{4+} has to be maintain initially in acidic conditions (*pH* ≤ 5), carefully controlling the addition to avoid the formation of TiO_2 precipitates.

During the work involved in this thesis we prepared stable precursor polymer-metal solutions of 16 different elements (Figure 34).

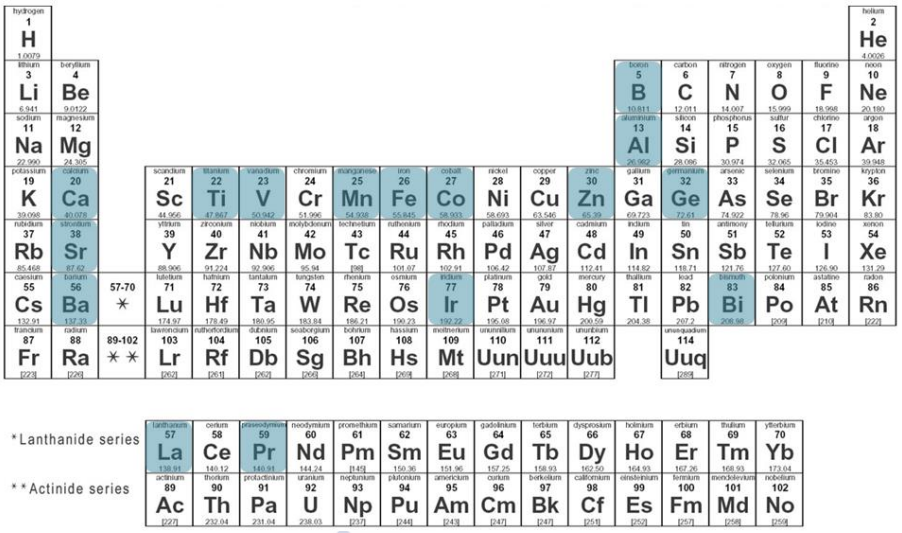

Figure 34. Cations stabilized for PAD process in this thesis (highlighted in blue). Stable solutions of Alkaline earth metals, Transition metals, Lanthanides, Post-transition metals and metalloids were produced.

After preparation of a given solution, they are kept several hours before filtration, just to confirm that no precipitate is formed. The solutions prepared in this way are stable under typical laboratory conditions, which simplify further handling and processing. For this reason the deposition on a substrate can be done easily at room temperature conditions under air in a fume hood.

This stability is very important for a long-time research project, when is preferable to prepare all films with the same batch of precursors solutions. The same is true for investigations about series in a diagram of composition in multi-element compounds, where the doping is made just varying the relationship of elements by adding different amounts of solution.

3.3. Filtration of metal polymer solutions

The solutions prepared as described before must be further purified prior to deposition on the substrate. Spin coating of non-purified solutions would result in a polymeric film full of defects and aggregates, as shown in the Scanning Electron Microscopy (SEM) picture of Figure 35. These aggregates are several microns size, and we observed that they are responsible for the appearance of the imperfections in the

inorganic film after high temperature annealing. These defects destroy the homogeneity of the films and prevent their scalability over large areas.

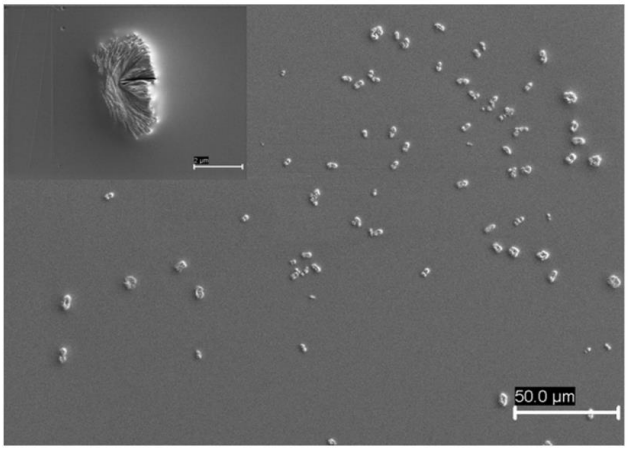

Figure 35. SEM image of the polymeric film, just after spin coating. The presence of large polymeric aggregates is clearly observed. The scale bar in the inset is 2 µm. Images were recorded in a *Zeiss Plus* at 3 keV conditions and 2.5 mm work distance.

Therefore removing these insoluble aggregates is a crucial step for the fabrication of high quality films. In order to remove them, the solutions are filtered using an *Amicon* ultrafiltration cell, with a cutoff filter of 10 kDalton. Uncoordinated cations, anions, and low molecular weight fractions of the polymer are removed in this step in the permeated fraction while the purified retained portion of the solution is employed for the synthesis of films.

Typically, the metal polymer solution contained in 100 mL is transferred to a stirred *Amicon* filtration unit model 8200 with capacity for 200 mL from *Millipore* (Figure 36). In this thesis, were employed separation membranes of 10,000 Dalton of pore size as molecular weight cut-off (MWCO), what means that removes from solution those compounds with molecular weights lower than 10 kDa. The driven force for this purpose is pressure into the cell, which is applied by 30 psi N_2 gas line after closing pressure relief valve allowing that solution overpass membrane filter drop by drop until a final volume of less than 50 mL is reached. The operation is repeated twice again, adding deionized water up to 100 mL before of each filtration. The stirrer speed is controlled by a magnetic stirrer under the cell, usually set at 60 rpm. The filtration ends up to attaining the desired volume, 10 mL of solution for each 1 g. of PEI.

As an alternative for low-volume solution filtration, 15 mL centrifugal filters (Figure 36.c) were employed, especially for *pH*-dependence analysis in which small portions of 5 mL were taken. These filters are

positioned into a centrifuge, in which the centrifuge speed was set at 5000 rpm during 10 min. Then 2 mL of deionized water were added, repeating this filtration procedure twice to ensure that no undesired species remain in the retained portion of the solution.

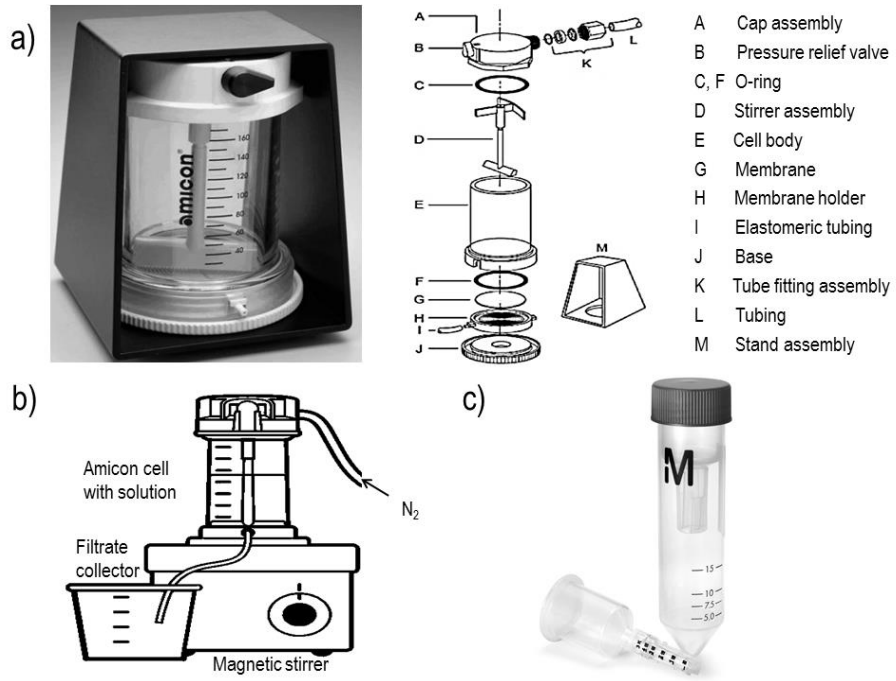

Figure 36. a) *Amicon* stirred cell model *8200* indicating all constitutive elements. b) Apparatus for ultrafiltration of polymer solutions. c) Example of 15 mL capacity *Amicon* centrifugal filter.

On the basis of Size Exclusion Chromatography (SEC), a comparison of retained and permeated portions of the filtered solution is shown in Figure 37. For these measurements a Gel Permeation Chromatograph PL-GPC 50 integrated system (*Agilent*) was used. Two PL aquagel-OH 40 and 30 columns in series (300 x 7.5 mm, particle size 8 μm) were used to optimize the separation conditions. The flow rate was set at 1 mL/min and the analysis were performed at room temperature injecting 0.2-1 % (w/v) sample solutions filtered with 0.45 μm membrane (Millex-GV, *Millipore*). Column calibration was carried out with poly(ethylene oxide) (PEO) narrow distribution standards, using a third order polynomial equation obtained from regression analysis. Various aqueous mobile phases were investigated to reduce enthalpic interactions, i.e. adsorption, of the PEI molecules with the macroporous hydrophobic packing particles. The following eluents were tested, after degassing by ultrasounds: ultrapure water (MilliQ), 0.3 M NaAc (*pH* adjusted to 4.4 with acetic acid), 0.3 M NaAc with up to 30 % v/v ratio of methanol, 0.05 M NH_2PO_4 (*pH* 4.5) and 0.05 M NH_2PO_4/methanol 20% v/v, although only 0.05 M NH_2PO_4 solutions with different amount of NaCl in the range 0.05-0.30 M could suppress either hydrophilic and hydrophobic interactions

between PEI and the stationary phase. Only very low molecular weight fractions were removed in this step, with a nominal number average molecular weights of ≈ 1,000 g/mol, with respect to the values of M_n = 193,000 g/mol for SU-PEI and M_n = 35,000 g/mol for SA-PEI.

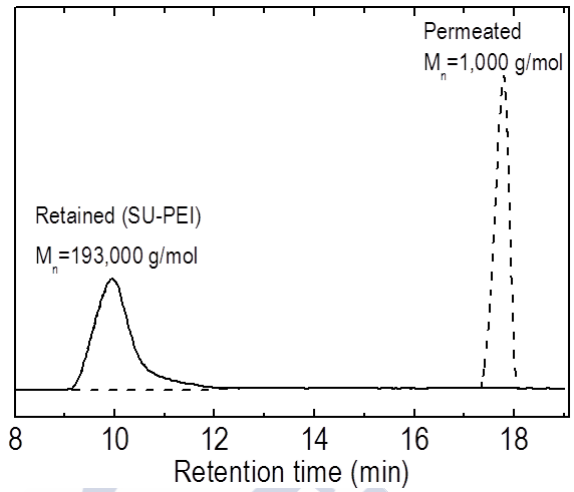

Figure 37. Molecular weight and their distributions were determined by Size Exclusion Chromatography (SEC) in aqueous solutions. SEC chromatograms of retained (solid line) and permeated SU-PEI (dashed line) portions after *Amicon* purification.

On the other hand, more sensitive NMR experiments revealed minor albeit important dissimilarities between the polymeric species retained and permeated through the *Amicon* membrane (Figure 38). Around 10 different peaks may be distinguished in the ^{1}H NMR spectrum of permeated PEI. All of them refer to methylene groups in N-CH_2-CH_2-N units, featuring a structure that mostly contains primary and tertiary amines. This fact indicates the presence of different species than can be isolated from their different molecular size. Moreover, the lower species, permeated, presents a globular structure with a different chemical bond nature than can be isolated from purification process. This different structure has implications in a different behavior in solution and in consequence an inhomogeneous coordination to metals.

Signal assignments in NMR spectra were based on previously reported information [135], and in the case of ^{1}H NMR were also verified by either 2D proton Total Correlation Spectroscopy (TOCSY) or ^{1}H-^{13}C Heteronuclear Single Quantum Coherence spectroscopy (HSQC).

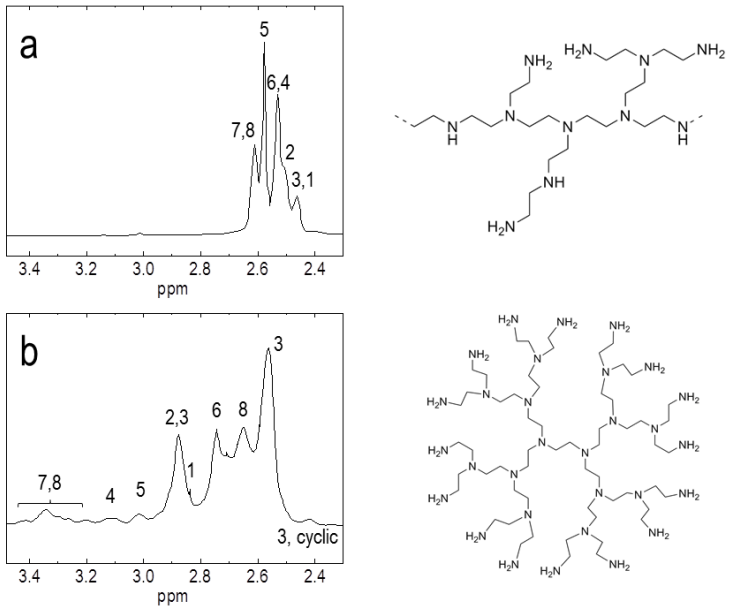

Figure 38. ^{1}H NMR spectra of retained (a) and permeated (b) SU-PEI; signal assignments, by 2D TOCSY and 2D HSQC ^{1}H-^{13}C NMR experiments, respectively, refer to the structural units reported in Figure 30.

Unexpected chemical shift of structurally similar methylene groups, either within the permeated PEI or with respect to those displayed in retained PEI may be ascribed to variable solvent-molecule interactions, and more specifically to the corresponding shielding/deshielding effects, dependent on molecular shapes, branching and dimensions.

To further investigate the dynamic properties of permeated PEI molecules in solution, pulsed-field gradient (PFG) NMR measurements were performed. Firstly, the application of the so-called diffusion filters (see example in Figure 39) entailed in the case of permeated PEI a clear attenuation of signals for spin lock times up to 600 ms. This behavior is related to qualitatively faster relaxation or diffusion rates which confirm that the molecules of PEI in the fraction permeated through the filter from the original solution are formed by smaller molecules in comparison with original PEI. In the unpermeated portion, where high molecular weight macromolecules are expected to predominate, this procedure did not show any significant change in signal intensities.

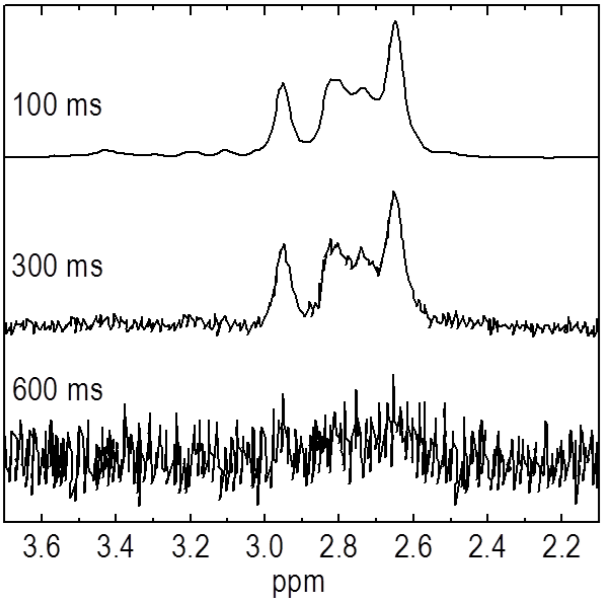

Figure 39. ^{1}H PFG NMR spectrum of permeated PEI for increasing spin lock times. The use of diffusion filters provides a marked improvement in the resolution.

Quantitative information about the molecular weight of these smaller components was obtained from the attenuation of the NMR signal during Diffusion Ordered Spectroscopy (DOSY), through the determination of their diffusion coefficient, *D*. The degree of attenuation is a function of the magnetic gradient pulse amplitude, *G*, and occurs at a rate proportional to *D*, which may be estimated by, e.g., the Stejskal-Tanner equation [136]:

$$S(G) = S_0 e^{-\gamma^2 G^2 \delta^2 D\Delta'} \tag{3.2}$$

where S_0 denotes the signal intensity without gradients, γ is the nuclear gyromagnetic ratio, δ is the gradient pulse duration, and Δ' is the "corrected" diffusion time. In the simplest pulse sequences Δ' is simply the interval between the two field gradient pulses, or more generally $\Delta' = (\Delta - \delta/3)$. On the basis of the experimental evidence, a power law correlation between *D* and the molecular mass *M* can be formulated to describe the behavior of a homogeneous family of molecules over a wide range of molecule sizes [137]

$$D = AM^{-\alpha} \tag{3.3}$$

A and α are constants that correlate to different families of polymers. On the other hand, the Stokes-Einstein equation for a spherical particle in solution of radius R_H

$$D = \frac{\kappa T}{6\pi\eta R_H} \tag{3.4}$$

where η is the solvent viscosity, and the Flory equation, where the gyration radius of a molecule is related to its molecular mass through the inverse of the fractal dimension d_f of the homogeneous molecular family:

$$R_H \propto M^{1/d_f} \tag{3.5}$$

Therefore, the molecular mass can be determined following [138]:

$$M \approx \left(\frac{c_r}{D_r} \right)^{d_f} \tag{3.6}$$

where $D_r = D/D_{ref}$ is the relative diffusion (D and D_{ref} are the diffusion coefficients observed for the molecule of interest and for a reference molecule), and c_r is a calibration constant. Both d_f and c_r depend on the molecular family being studied and have to be determined experimentally. For the determination of molar masses in our system, we used previously determined values, namely those measured for generic small molecules in D_2O (c_r = 5.17, d_f = 1.836 and semiheavy water HDO as reference) and for globular proteins (c_r = 7.2, d_f = 2.56 and tris(hydroxymethyl)aminomethane as reference) for the estimation of permeated SU-PEI and unfiltered SU-PEI, respectively.

In Figure 40, a series of NMR diffusion spectra of permeated PEI acquired as a function of the gradient strength are shown. The intensity of all the signals follows the same exponential decay, indicating that only one type of molecular species is present. From its fitting to eq. 3.2, the value of the coefficient was estimated as D = 109 $\mu m^2 s^{-1}$, which applying eq. 3.6 results in $M \approx$ 5,000 g/mol. Similar measurements for unfiltered PEI unveiled the sample as a two components mixture with a very small component, i.e. the permeated fraction, and a second component with D = 21 $\mu m^2 s^{-1}$ and $M >$ 200,000 g/mol.

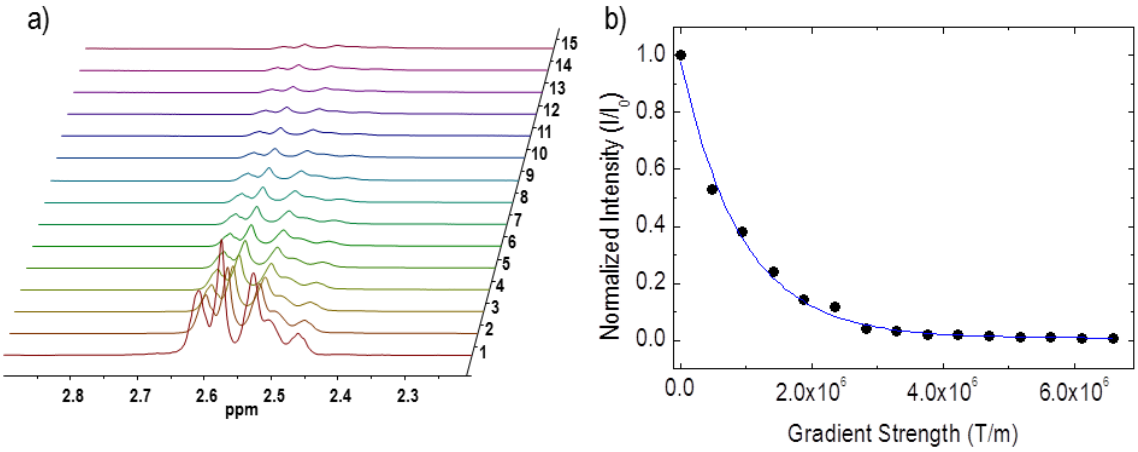

Figure 40. a) Array of ^{1}H PFG NMR spectra of permeated PEI measured with linearly increasing field, and b) logarithmic plots of the signal intensities as a function of the gradient amplitude at 25 ºC, for an observation time of Δ = 200 ms and gradient pulse width of δ = 4 ms.

From these experiments, a molecular mass of ≈5,000 g/mol was obtained for the permeated molecules of PEI. The apparent inconsistency between this value and that obtained by SEC (< 1,000 g/mol) is intrinsic in the basis of the chromatographic separation process. Since in hyperbranched polymers the molecular hydrodynamic volume does not grow linearly with the molecular weight, the values determined by SEC inevitably appear underestimated in comparison with those calculated by DOSY, appropriately calibrated for small molecules.

Therefore, we have identified the presence of low molecular weight fractions of the polymer in the permeated solution during the *Amicon* filtration process. It is very important to note that these molecules show a different molecular architecture, and for that reason different chemical properties (*pKa*, solubility, coordination, etc.) that larger fractions of PEI with higher molecular weight (retained during the *Amicon* purification).

The origin of these relatively small molecules is probably due to the method of synthesis and therefore they must be present in most commercial PEI with high molecular weight. As we have just shown, elimination of these small molecules prior to deposition of the film is crucial for the scalability of the method, in order to obtain homogeneous films, free of defects over large areas.

Finally, Fourier Transform Infrared spectroscopy (FT-IR) also detected rather similar structural features in all the fractions of filtered PEI (Figure 41). The nature of the bands observed in the permeated portion is

very similar to the retained. Some differences are visible only in the fingerprint region between 500 and 1200 cm^{-1}.

FT-IR experiments were performed in a *Thermo Nicolet FT-IR Nexus* instrument equipped with a *Smart Endurance* device for Attenuated Total Reflectance (ATR) measurements and a deuterated triglycine sulfate (DTGS) detector. This detector is very sensitive at room-temperature for mid-infrared range measurements owing to the employment of temperature-sensitive ferroelectric crystals of DTGS. The absorption of the IR changes the temperature and hence the polarizability of the crystals, what generates a charge that is detected by two parallel electrodes. The ATR enables that samples can be examined directly in solid (KBr pellets) or liquid (solved in chloroform –IUPAC name trichloromethane– $CHCl_3$) state.

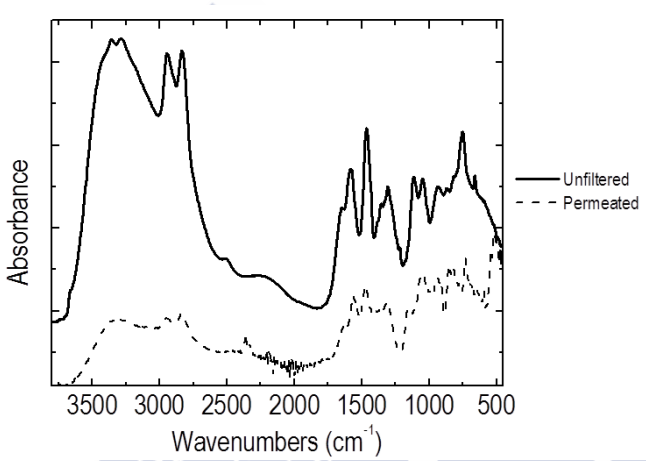

Figure 41. FT-IR spectra of unfiltered (solid line) and permeated SU-PEI (dashed line). IR absorption spectra in ATR mode were collected with a *Thermo Nicolet FT-IR Nexus* instrument equipped with a *Smart Endurance* device, and a DTGS detector, at a 4 cm^{-1} resolution for 128 scans.

3.4. Coordination of PEI to metals and complexes

In order to follow the coordination of metallic species to PEI and to determine their total concentration in the purified solutions, we performed UV-Vis spectroscopic analysis. An example is shown for V^{5+} in Figure 42, representative of results for other ions, to determine V^{5+} coordinated to EDTA, PEI, and EDTA-PEI. Experiments were performed in an UV-Vis Spectrophotometer *Varian Cary 100 Bio* from *Agilent* at 25 ºC

with 3 mL of solution of [V^{5+}] = 8 mM. Although there is some variation in the spectra, a quantitative determination cannot be made due to the fact that both species absorb in the same range.

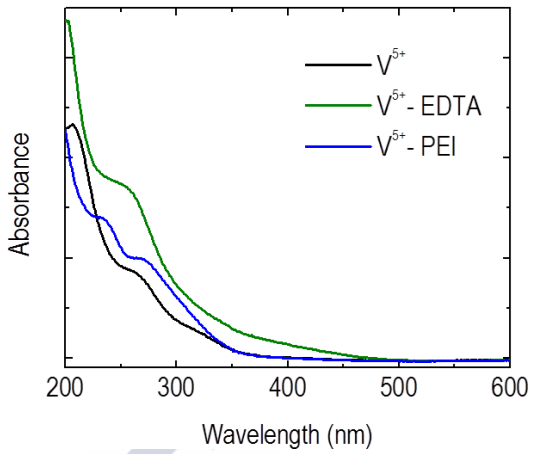

Figure 42. UV-Vis spectra of V^{5+} in water (black), coordinated to EDTA (green), and coordinated to PEI (blue). The experiment was recorded in an UV-Vis Spectrophotometer *Varian Cary 100 Bio* from *Agilent* at 25 ºC with 3 mL of 8 mM in V^{5+}.

For that reason we followed the coordination of metallic species to the polymer and their total concentration in solution by Inductively Coupled Plasma Atomic Emission Spectroscopy (ICP-AES), as we will describe below.

ICP analysis were performed with two different spectrometers: a *Varian Liberty 200* located at Instituto de Cerámica de Galicia of USC and a *PerkinElmer Optima 4300 DV* located at USC facilities at CACTUS-Lugo. The samples were prepared in 10 mL vials diluted 100 times from initial solutions in order to prevent saturation in the detector (loss of linearity of the calibration curve). The concentration of ions in the solutions was always well above the theoretical detection limits (TDL) for each element.

Metal	Ca	Sr	Ba	Ti	V	Mn	Fe	Co	Zn	Ir	La	Pr	Al	Bi	B	Ge
TDL (ppb)	10	4	1.3	3.8	5	1.4	4.6	6	1.8	27	10	37	28	24	4.8	40

This chemical analysis offers a simple way to study the efficiency of the interaction of PEI to metals and to anionic complexes just comparing the yield between retained and permeable portions during *Amicon* filtration. The efficiency of PEI to coordinate different metals was quantified through the degree of retention of metal ions after ultrafiltration of the solutions.

In order to calculate the degree of retention, the retained and permeated volumes must be taken into account, besides the molar concentration, so that the ratio between the number of moles (*n*) is obtained.

$$Retention = \frac{n_{retained}}{n_{retained} + n_{permeated}} = \frac{[Retained].V_{ret}}{[Retained].V_{ret} + [Permeated].V_{perm}} \quad (3.7)$$

The higher the formation of the metal complex polymer species the higher the degree of retention, because in order to remain into the retained portion of the filtered solution, the metal or the complex metal necessarily must be coordinated to PEI. The degree of retention after ultrafiltration, as well *pH* of metal polymer solutions are summarized in Table 3 and plotted in Figure 43 for different ions prepared in this thesis. In this table are also indicated the ratio in solution between metal and EDTA expressed in molar ratio, and the EDTA:PEI mass ratio.

Category	Cation	*pH*	Retention (%)	M:EDTA molar ratio	EDTA:PEI mass ratio
Alkaline earth metals	Ca^{2+}	4.36	69,27	1:1	1:1
	Sr^{2+}	6.20	81.30	1:1	1:1
	Ba^{2+}	7.38	93.67	1:1.35	1:1
Transition metals	Ti^{4+}	7.11	77.87	1:2	1:1
	V^{5+}	10.21	67.52	No EDTA	-
	Mn^{2+}	4.68	50.64	2:1	1:1
	Fe^{2+}	4.77	77.06	1:1.4	1:1
	Co^{2+}	8.01	89.67	1:1	1:2
	Zn^{2+}	3.67	94.69	1:1	1:1
	Ir^{3+}	5.16	73.30	1:1	1:1
Lanthanides	La^{3+}	8.69	94.66	1:1	1:2
	Pr^{3+}	8.41	77.61	1:1	1:2.5
Post-transition metals	Al^{3+}	5.44 / 8.31	97.88 / 95.87	1:2	1:1 / 1:2
	Bi^{3+}	8.67	65.95	1:1	1:2
Metalloids	B^{3+}	9.29	66.77	No EDTA	-
	Ge^{4+}	6.99 / 8.51	75.10 / 74.71	1:0.6 / 1:0.7	1:1 / 1:1.6

Table 3. Degree of retention of different ions at their corresponding *pH* in solution. The proportion of EDTA with respect to metal, and the proportion of EDTA to PEI, are also indicated.

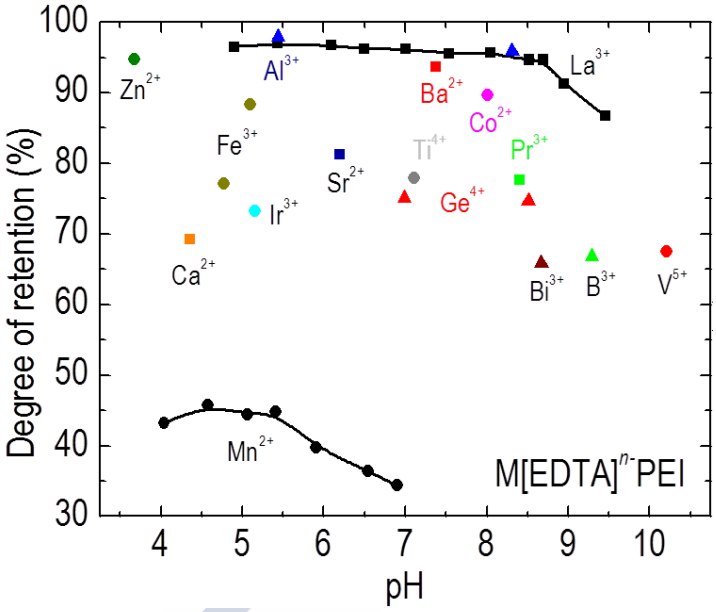

Figure 43. Degree of retention of different ions prepared in this thesis. Most of cations yielded degrees of retention higher than 60 %. For La^{3+} and Mn^{2+} are also shown their degree of retention as a function of *pH*.

As it can be seen most of elements employed in this work show a satisfactory behavior in polymer solutions, yielding high degrees of retention. Furthermore, most of the solutions are stable for months and even years, due to the affinity of EDTA for metals and of PEI to EDTA-metal complexes. The reason in terms of chemical interaction is that EDTA contents four carboxylate and two amine groups capable to bind to a metal, which in terms of chemical hardness [139] are considered quite soft, very appropriate for most of metals.

For some metals, several *pH* restrictions must be respected in order to prevent metal hydrolysis. For instance, La^{3+} hydrolysis occurs at *pH* ≈8.5 [140] while a *pH* ≈7 is enough to hydrolyze Mn^{2+}. This fact has to be considered also when mixing individual solutions of different metals to prepare a solution for the synthesis of a multicationic film.

The importance of using a chelating agent for improving the metal coordination and therefore its retention in a filtrated solution is evidenced by the results of La^{3+}. The hydrolysis of La^{3+} occurs at *pH* ≈8.5, so just dissolved along PEI (*pH* > 10), it remains insoluble. Decreasing *pH* does not imply directly coordination of PEI to La^{3+} until an anionic complex is formed.

In order to corroborate this behavior, La^{3+} polymer solutions were prepared with hexa-dentate (EDTA-6D), and also with other aminocarboxylic chelates, tetra-dentate diethylenetriaminepentaacetic dianhydride

[141] (cDTPA-4D) and octa-dentate diethylenetriaminepentaacetic acid [142] (DTPA-8D), along EDTA (Figure 44). The presence of N and O as donor groups with unshared pairs of electrons in their structures favors the formation of electrostatic interactions with PEI.

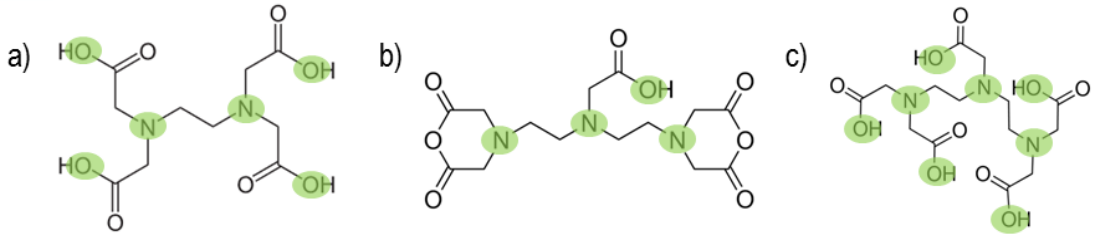

Figure 44. Chelating agents used for coordination to La^{3+}: a) ethylenediaminetetraacetic acid (EDTA), 6D; b) diethylenetriaminepentaacetic dianhydride (cDTPA), 4D; c) diethylenetriaminepentaacetic acid (DTPA), 8D.

La^{3+} is a polycoordinationable cation in which the most common coordination numbers are 8 with cubic arrangement in $[La(bipyO_2)_4]^{3+}$ and 9 with triply capped trigonal prismatic arrangement in $[La(H_2O)_9]^{3+}$ or $LaCl_3$, and any perovskite oxide. However, complexes are also known in which lanthanum presents coordination numbers smaller than 8, and larger than 9 [143]. These three chelating agents show good yielding in solution and very similar degrees of retention for La^{3+} (Table 4). The similar degree of retention of these three ligands in La^{3+} cation is explained by the capability of 4D to bind in different configurations and of 8D to be particularly useful for binding lanthanide ions.

La^{3+} to	*pH*	Solution	Retention (%)
PEI	10.28	precipitates	-
PEI	8.79	precipitates	-
PEI	7.64	precipitates	-
PEI	5.81	precipitates	-
EDTA-6D:PEI	8.27	stable	95.64
cDTPA-4D:PEI	7.87	stable	96.10
DTPA-8D:PEI	7.95	stable	95.98

Table 4. La^{3+} polymer solution prepared at different *pH* just with PEI and with three different aminocarboxylic chelating agents (EDTA, cDTPA, and DTPA).

The effect of *pH* on the coordination of the different complexes of La^{3+} to PEI is shown in Figure 45. The enhancement of electrostatic interactions, particularly hydrogen bonds, takes places at lower values of *pH*,

where most of amines of PEI are protonated. Although the efficiency in retention for La^{3+} is high in a wide range, it decreases above *pH*≈8.5.

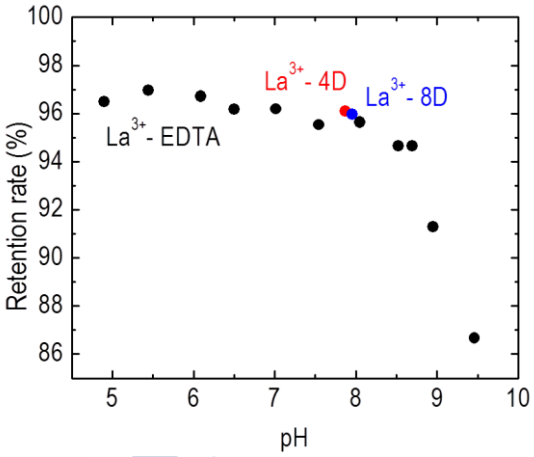

Figure 45. *pH* dependence of the degree of retention for the complex [La(EDTA)]-PEI. The degree of retention of cDTPA and DTPA complexes to La^{3+} is also shown.

3.5. Final mixtures and adjustments of solutions previous to deposition

The purified solutions of each individual cation are then mixed, when is required, according to the final desired stoichiometry.

PAD can be used for the synthesis of poly-cationic compounds because polymer coordination prevents any undesired reaction in the solution due to differences in chemical reactivity among metals. Different *pH* values can alter coordination conditions or even lead to hydrolysis in some cases. Therefore, it is a good practice to ensure that the solutions show similar *pH* values before mixing, in order to prevent a destabilization of the final mixture.

In this thesis were prepared different multicationic materials such as $La_{1-x(}Ca,Sr)_xMnO_3$, $LaCoO_3$, $Ca_3Co_4O_9$, $Sr_3Co_4O_9$, $[Bi_{1.74}Sr_2O_4][CoO_2]_{1.82}$, $[Bi_2Ba_{1.8}Co_{0.2}O_4][CoO_2]_2$, $[Bi_{1.68}Ca_2O_4][CoO_2]_{1.69}$, $BiFeO_3$ and $SrIrO_3$.

3. Characterization and optimization of the relevant chemical aspects of the precursor solution for the synthesis of thin films

Below we show the characteristic data for mixing of individual solutions with a given molar concentration for obtaining 15 mL of the solution for $La_{0.7}Sr_{0.3}MnO_3$ in a concentration of 106 mM:

Cation	Stoichiometry	Molar concentration (mM)	Volume (mL)
$[La^{3+}]$	7/10	96.105	5.993
$[Sr^{2+}]$	3/10	51.016	4.839
$[Mn^{2+}]$	1	175.064	4.700

And for $La_{0.7}Sr_{0.3}MnO_3$ with 5 % of Ti^{4+}. In this case the final volume was 7.16 mL and total molar concentration $[M]_T$=99 mM. For the formation of this particular film, the solution was concentrated to 200 mM reaching a final volume of 3.50 mL prior to spin-coating. The *pH* values of the initial solutions for each individual cation are also indicated.

Cation	Stoichiometry	Molar concentration (mM)	Volume (mL)	pH
$[La^{3+}]$	70/100	158.304	1.604	5.07
$[Sr^{2+}]$	30/100	51.016	2.133	4.96
$[Mn^{2+}]$	95/100	172.260	2.000	5.42
$[Ti^{4+}]$	5/100	12.671	1.431	6.41

The different precursor solutions are transferred by using micropipettes with low-retention tips for a higher accuracy. After mixing the final solution is usually evaporated or diluted for increasing or decreasing the molar concentration.

Once a stable metal polymer solution is prepared, its viscosity can be adjusted, both increasing it by evaporating water above a hot plate at 70-80 ºC or decreasing it by diluting with deionized water. The molecular weight and the degree of branching of polymer also have some influence on the viscosity. It must be remembered that viscosity is an important parameter in spin/dip-coating at the time of varying the thickness layer.

The dynamic viscosity η of the solutions was measured at 20 ºC with a *DMA 4100M Anton Paar* density-meter, with a microviscometer module *Lovis 2000 ME*, of 1.59 mm capillary diameter, and 1.5 mm steel ball of ρ=7.68 g/cm^3.

The values of viscosity for the solutions used in this thesis were adjusted in the range of $\eta \approx$3-4 mPa.s in order to obtain optimal deposition conditions for the spin coating. Notice that the dynamic viscosity of water at 20ºC is η=1.002 mPa.s, while the permeated portions have values of η=1.01-1.08 mPa.s, close to water. Also highly concentrated solutions (up to 0.4 M) with values of η=6 mPa.s were applied by spin coating for growing thicker films, of 50 nm in a single coating.

3.6. Preparation of the substrate

Before deposition, the appropriate substrate must be selected in terms of structure, lattice parameter matching, and orientation. Also, preconditioning of the substrates plays an important role in two directions: increase the adherence of solution (in aqueous solutions hydrophilicity) and obtain a flat surface with homogeneous termination if required for a particular experiment (like for instance TiO_2 in $SrTiO_3$ substrates).

Ensuring a good adherence of the solution to the substrate is crucial to ensure a complete and homogeneous coating of the substrate surface, preventing the appearance of holes and variations of thickness.

For instance, in the case of cubic Silicon substrate (a=5.431 Å), hydrophilicity can be increased on top of SiO_2 native layer, by promoting the silanol (Si-O-H) group formation [144].In Si soft oxidant treatment in diluted aqueous solution of ammonium hydroxide and hydrogen peroxide (H_2O:NH_4OH:H_2O_2 in 7:4:1) at 47 ºC [145] allows to reduce the contact angle (θ_c) from 70º to 45º for the sake of a better wettability (Figure 46).

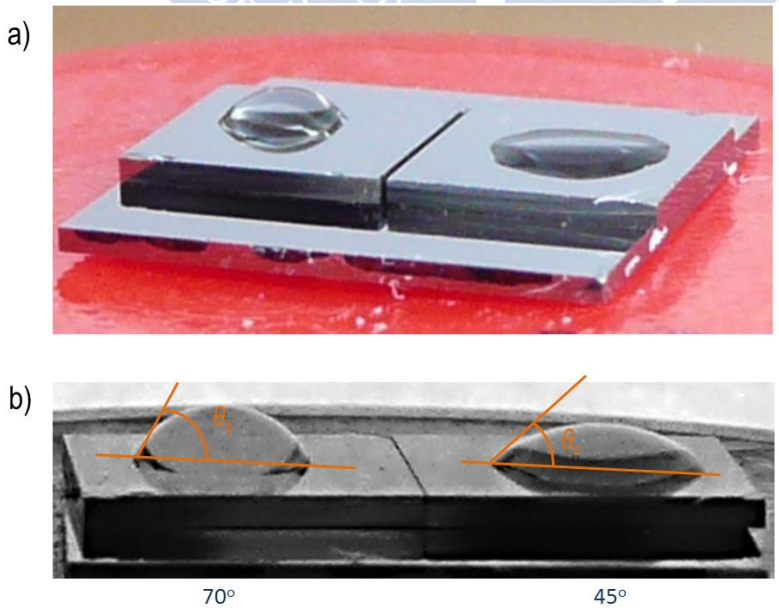

Figure 46. a) Silicon substrate without treatment for hydrophilization (left) and hydrophilizated (right). b) Determination of the contact angles between the solid surface (substrate) and the tangent of drop in contact with air.

With regard to oxide single-crystal substrates, there are several treatments for reaching the best platform to grow epitaxial thin films. The pretreatment depends on every substrate but in general a high temperature annealing is necessary for surface reconstruction in combination with a selective wet etching. In particular, perovskites (ABO_3) are a broad family of materials with variable composition and lattice parameter, ideal for being used as single-crystal substrates, and their surface can be modulated to perform the best interface possible. Perovskite structure can be described as a combination of alternating layers of AO and BO_2 in the [001] direction, and both terminations exist in most cases at the surface in equal proportion, giving surface steps of half or one unit cell height.

In the case of STO, the homogenous termination on a TiO_2 surface will favor the preferential deposition of AO (*A*-site) layer of the perovskite (ABO_3) film, thus forming an epitaxial TiO_2-AO interface.

The preparation of substrate surface [146] before of film deposition demanded the interest of researches with special emphasis on cubic $SrTiO_3$ (STO, a=3.905 Å), the most popular single-crystal substrate. The use of hydrofluroric acid (HF) and its derivatives is well-known for acid chemical etching of STO surface [147] even for polar (111) orientation [148]. However, a safer and softer wet-etching is preferable. In this sense, other soft surface treatment methods for STO combining solution and annealing have been developed [149]. Specifically for STO (001), flat and homogeneous surface termination in TiO_2 were obtained by preferential acid chemical etching of SrO by treating the as-received substrate in deionized water at 70 ºC and then in aqua regia (HCl-HNO_3 3:1), with a subsequent annealing at 1000 ºC in air for 30 min. [150]. As it can be observed from Atomic Force Microscopy (AFM) images (Figure 47), the roughness of the surface so obtained is very flat, with values of root mean square roughness R_q = 0.13 nm. Moreover, the line profile indicates that the height of terraces is in coincidence with the size of STO lattice parameter ~ 0.4 nm proving the single-terminated surface.

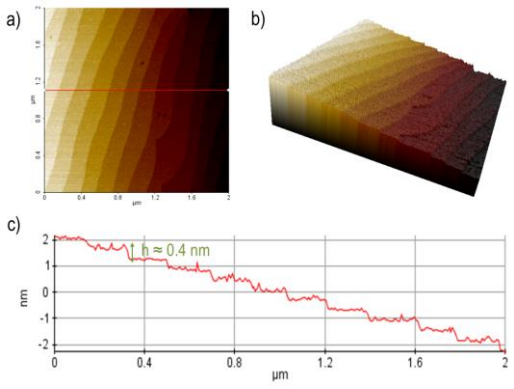

Figure 47. a) 2x2 µm² AFM topography image of TiO_2 terminated STO (001) substrate from *CrysTec GmbH*. b) 3D image of the same sample for visualizing more clearly flat terraces in perspective. c) Line profile along the terraces, demonstrating that their height is very close to lattice parameter of ~ 0.4 nm.

Alkaline chemical etching was also explored for obtaining flat surface both on STO and on rhombohedral $LaAlO_3$ (LAO, a_{pc}=3.791 Å). The objective of the wet etching is the selective etching of one cation in function of their different solubility, what varies in function of the solvent, temperature and time. Etching relies on thermodynamic and kinetic differences to form first, and then to dissolve selectively the corresponding hydroxides between the two cations of the perovskite structure, $A(OH)_n$ and $B(OH)_m$.

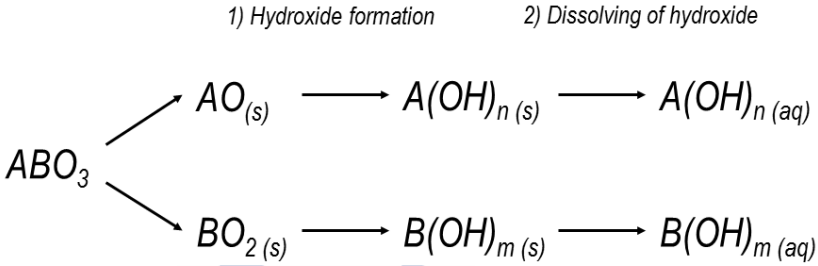

With this purpose as received substrates were immersed into a saturated solution of KOH in isopropanol during 10 min in an ultrasonic bath at 40 ºC, rinsed in deionized water and further annealed at 1000 ºC in air during 30 min. This treatment was followed after every single step in order to observe their individual effect. Just annealing promotes the surface reconstruction of terraces, but however it has an effect of segregation of several nanometers-size particles of SrO and La_2O_3 on the surface of STO and LAO substrates, respectively (particularly enhanced in the latter case) (Figure 48). Hence, any thermal treatment of films over non-prepared substrates will entail this type of defects.

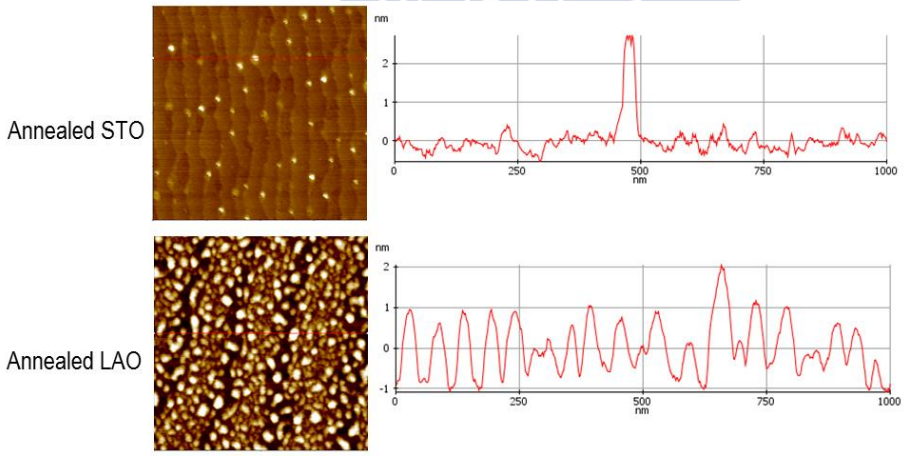

Figure 48. 1x1 µm² AFM topography images of annealed STO (up) and LAO (down) substrates from *Crystal GmbH*. Their respectively line profiles are shown at right.

That means annealing is a requirement, but also the wet etching is needed in order to dissolve selectively these oxides from the surface. The combination of basic etching and annealing produces very flat surfaces free of defects with the same R_q of acid etching (Figure 49).

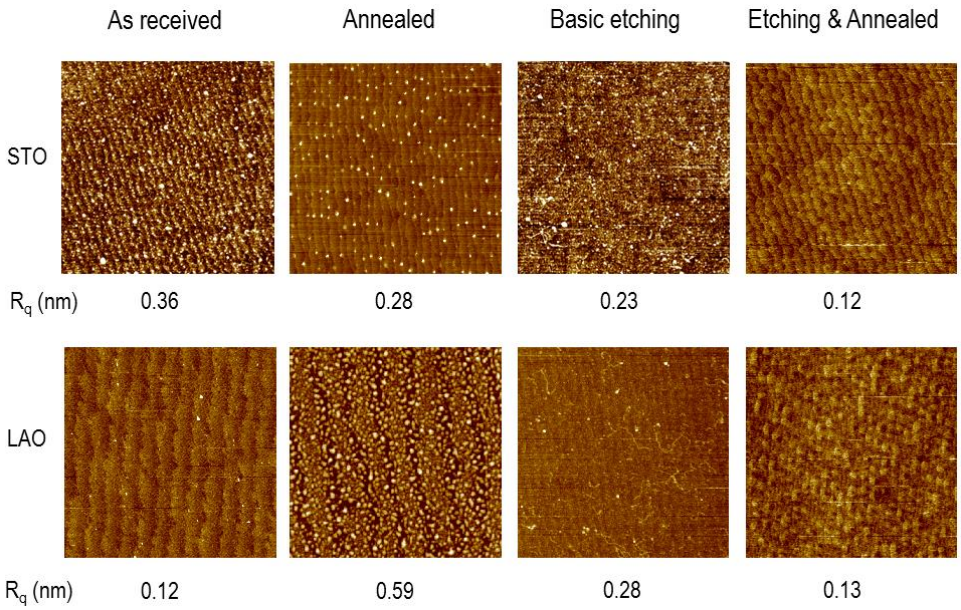

Figure 49. 2x2 µm² AFM topography images of STO (up) and LAO (down) substrates from *Crystal GmbH*. The values of R_q are indicated for as received substrates, annealed, just alkaline etching, and totally treated by basic etching and annealing.

With this treatment flat terrace-terminated surfaces are obtained in STO (Figure 50 top), while in LAO the unit cell terraces are not clearly visible in their flat surface (Figure 50 down).

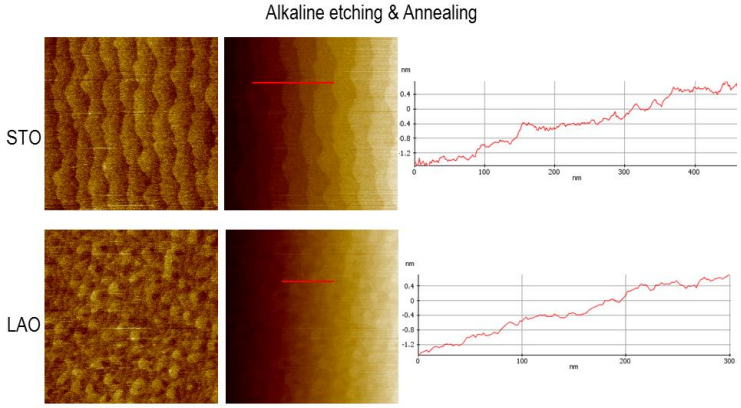

Figure 50. 1x1 µm² AFM topography images of alkaline treated STO (up) and LAO (down) substrates from *Crystal GmbH*. In the center are shown tilted images in order to appreciate clearly the line profiles (right).

Other substrates (no perovskite-like) as cubic Yttria-Stabilized Zirconia (YSZ, a=5.12 Å) does not required complex processes; annealing at 1000ºC in air during 30 min. is enough to achieve a satisfactory surface reconstruction (Figure 51).

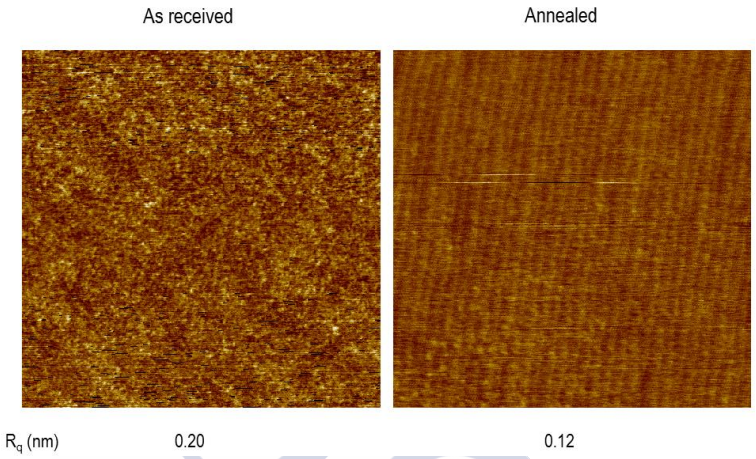

Figure 51. 2x2 µm² AFM topography images of YSZ substrate from *CrysTec* before and after annealing. R_q values are slightly affected but the surface morphology is notoriously improved.

Scanning Probe Microscopy (SPM) is the most powerful tool to study the surface of substrates and films. The first SPM invented was the Scanning Tunneling Microscope (STM) in 1982 [151], that measures the tunneling current between a sharp metallic tip and a conducting sample when are close enough but not in contact, providing the sample´s topography at the nanometer scale, the electrical properties by the quantum tunneling effect, and the electronic structure. However, STM cannot measure non-conducting materials, and Atomic Force Microscopy (AFM) [152] was developed to measure any sample regardless of its electrical properties. Instead of a conducting tip, AFM uses a flexible force sensor, so-called cantilever, with an integrated tip that measures the interaction (attractive and repulsive) forces on the order of pN between probe and sample, giving as a result information about the topography and other parameters with atomic resolution. Nowadays common integrated tips have radius of curvature lower than 10 nm and are fabricated in Si or Si_xN_{1-x}, but their characteristics and functionalization, as well as for cantilever, depend on the type of SPM technique. The variations on the bending of the cantilever due to the tip-sample interactions are detected by an mechanic-optical system, as the deflection is quantified by the measurement of a laser beam reflected from the backside cantilever onto the position sensitive photo detector (PSPD). In order to perform the scan, the sample is fixed on a piezoelectric tube-shaped scanner

that can be moved in the horizontal (*x, y*) and in the vertical direction (*z*), while the scan is performed line by line. The electronic controller of the AFM has a Digital Signal Processor (DSP) that collects the signal from the PSPD and controls the scanning system through a high voltage unit by a feedback loop (Figure 52.a).

The interaction forces between probe and sample come from different origins, mainly depending on the spatial separation between tip and surface. Short range forces are predominant when tip and sample are almost in contact, due to the overlapping of electron wave function and from the repulsive interaction of the ions. At very close distances are also found friction forces. Van der Waals forces are dipole-dipole interactions of weak intensity than electrostatic forces arising from Coulomb potential. Basically, when the distance between the tip and the surface becomes very short the interaction force is repulsive due to electrostatic repulsion dominates, and when the distance is longer enough the interaction force is attractive due to the long-range forces. The variety of interactions in AFM yields to three different modes of scanning between tip and sample attending to their distance: Contact Mode (repulsion between tip and sample is maintained constant), Intermittent Contact or Tapping Mode (tip oscillates into attractive and repulsive region), and Non-Contact Mode (oscillating tip is situated 5-15 nm above sample given information about morphology, amplitude, phase from frequency of oscillation) (Figure 52.b).

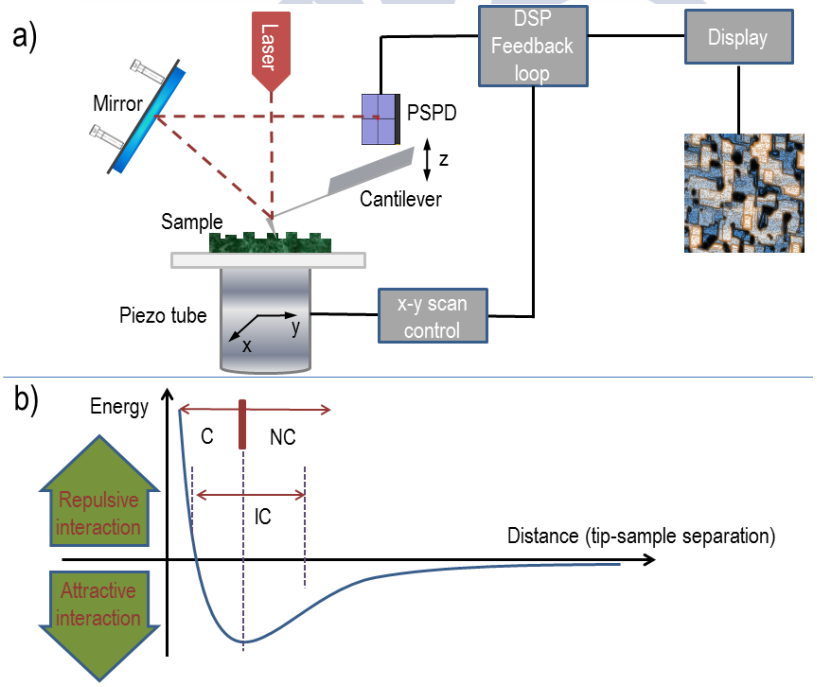

Figure 52. a)Schematic representation showing the characteristic parts of a conventional AFM. b) Relation of Potential energy with Distance tip-sample, indicating the repulsive and attractive interactions. The modes of STM measurement are also shown: Contact (C), Non-Contact (NC), and Intermittent Contact or Tapping (IC).

From AFM images we obtained the topographic image and surface roughness of the samples prepared in this thesis. The roughness is typically expressed by the root mean square roughness R_q, that represents the standard deviation of surface heights:

$$R_q = \sqrt{\frac{1}{N}\sum_{i=1}^{N}\left(z_i - \bar{Z}\right)^2} \tag{3.8}$$

where z_i is the height in a given point of the scan, N the number of points of measurement and $\bar{Z}$ is the arithmetic average height

$$\bar{Z} = \frac{1}{N}\sum_{i=1}^{N} z_i \tag{3.9}$$

3.7. Deposition of metal polymer layer: spin coating

Spin coating is a very common deposition technique in Nanotechnology, particularly in the field of photolithography for extending photosensitive resins (photoresist). Although is a very easy and affordable deposition technique its efficiency is very low, in the sense that less of 5 % of solution remains on the substrate [153].The thickness of the deposited film is inversely proportional to the square root of the angular speed $t \propto \frac{1}{\sqrt{\omega}}$. Therefore, knowing the rheological properties of the solution is possible to estimate the thickness (t) of a polymeric film deposited by spin coating. There are several theoretical models [154] to this respect, in which the most important parameters are the inherent viscosity η and the concentration of the polymer C. According to this, the best results are achieved with $\eta.C$ product close to 1, while higher values tends to increase the roughness and lower values tends to produce inhomogeneous coatings and edge defects.

For our work, the metal-polymer solutions prepared as explained before, with optimal conditions of viscosity and concentration were dispensed onto a substrate controlling several parameters, mainly the speed (rpm), time, acceleration, and volume deposited of the solution.

During this thesis was employed a spin-coater *WS-650-23 NPP* model from *Laurell* (Figure 53.a) that enables to perform different deposition programs. The substrate is vacuum-fixed to the holder of the spin-coater, the solution is dropped onto the substrate by using a micropipette and is properly extended to cover the whole surface before starting the acceleration ramp. Then the substrate is rotated at a given acceleration, speed and time for spreading completely the solution due to the centrifugal force generated by rotation. During the deposition most of solution is flung off from substrate as well as evaporation takes place throughout the process (Figure 53.b).

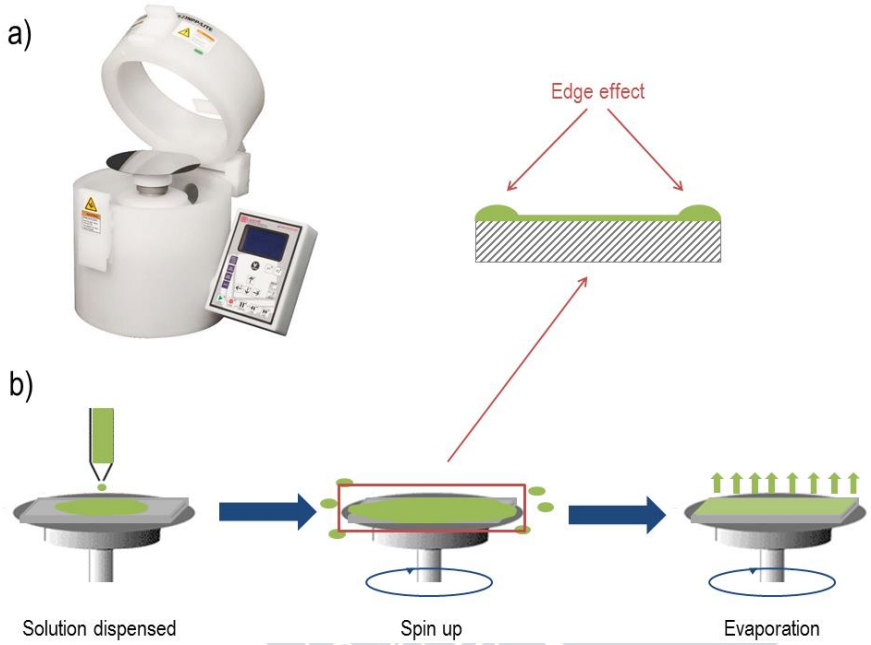

Figure 53. a) Spin-coater *WS-650-23 NPP* model from *Laurell* used in this work. b) Steps involved in deposition: fluid is dropped onto a substrate, rotation spreads solution while evaporation occurs. Borders introduce defects at the edges of the substrate.

The quality of the deposition depends on several factors: solution (volume, viscosity, surface tension), substrate (roughness, hydrophobicity, size, shape), spin-coater parameters (speed, acceleration, time) and environment (humidity and temperature), which must be properly identified and optimized for a good and reproducible deposition.

As a general rule, decreasing size in non-circular substrates implies to increase the ratio of defects in the surface, as edge effects tend to have a larger effect. The edge bead is due to fluid properties and the friction with air at the border of the substrate, where the solution is dried firstly. Many other defects can occur: bubbles, swirling or spiraling pattern, streaks, uncoated areas, pinholes, etc. These defects are due

to different causes: substrate in movement, faulty tip, incorrect deposition of the solution, acceleration too high, dust on surface of substrate, air bubbles, particles in solution, etc. [155]. Therefore, the deposition process must be done with exhaustive care because it is this step what defines to a great extent the uniformity of the final inorganic film.

In this thesis most of substrates employed have dimensions of 5x5 mm^2, so deposition conditions were optimized for this size. The volume of solution dispensed was around 30-50 μL, spreading onto the stationary substrate covering all surface. The acceleration applied during the spin up stage was 250 rpm/s, up to reach the final speed that ranges from 3,000 to 4,500 rpm depending on the viscosity (higher viscosity higher speed). The spinning is maintained during 20 s, and again the acceleration in the final ramp is 250 rpm/s.

Using these conditions results in smooth and homogeneous polymeric coatings of the substrate, whose thickness was proved by X-Ray Reflectivity, as shown in Figure 54.

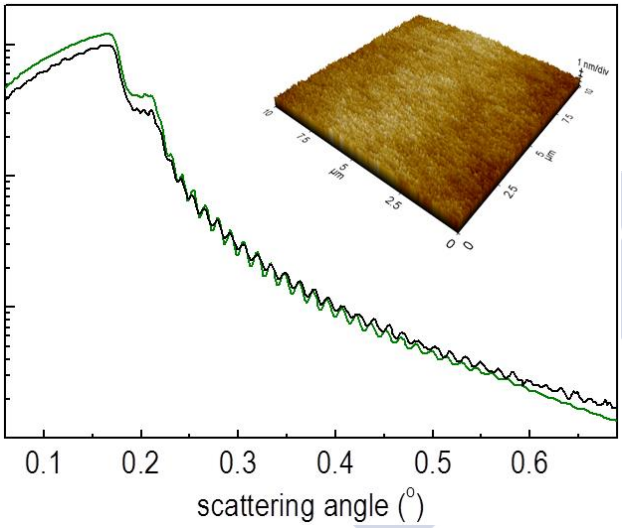

Figure 54. XRR curve of the polymeric film deposited by spin coating at 4,500 rpm during 20 s from 80 μL of a 0.20 M solution containing La^{3+} and Mn^{2+} on a 1x1 cm^2 silicon substrate. The fitting (green line) gives a thickness and density of the layer ≈265 nm and ≈1.5 g/cm^3, respectively. The inset shows the AFM topography (5×5 μm^2) of the polymeric film, very smooth (roughness ≈ 0.4 nm) and free of defects.

3.8. Thermal treatment

The homogeneous polymeric film is subsequently annealed at high temperature in order to obtain the final inorganic film. The thermal treatment of the metal polymer layer onto the substrate is the last step in the process of PAD. We followed the thermal decomposition of the polymer by thermogravimetric analysis (TGA). TGA provides a material characterization through mass loss as a function of increasing temperature, and provides valuable information about degradation mechanism and thermal stability of the macromolecule. The thermobalance employed in this thesis, a model *Q5000 IR* from *TA Instruments*, allows to follow the decomposition of the polymer under similar conditions to actual annealing of the films. This model can operate at different atmospheres (air, nitrogen, oxygen, etc.), controllable heating rates, reaching up to 1000ºC. TGA results are strongly depending on the atmosphere, heating rate, as well as on mass and morphology of the sample. The more rapid the heating rate the higher the degradation temperature obtained. In the case of polymers, it is particularly recommended to use always similar material quantities, since most mass tends to increase artificially the temperature of degradation. During all TGA analysis, approximately 25 mg of polymer were calcined in each test.

TGA curves of PEI, as well as retained and permeated portions in solution reveal almost coincident degradation pathways in air (Figure 55), which entail chemically similar polymer structures despite the large difference in molecular dimensions. The results are practically identical for both commercial polymers, although the decomposition occurring at slightly higher temperatures for SA-PEI. The curve of the permeated portion through the *Amicon* filter demonstrates again that a small fraction of polymer permeates through the membrane.

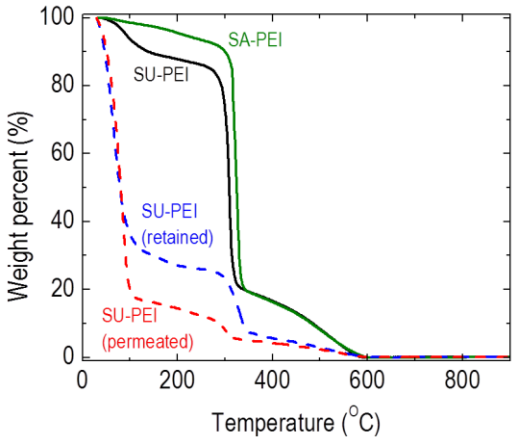

Figure 55. Thermogravimetric decomposition of SA-PEI and SU-PEI fractions in air. The TGA measurements were performed with a *Q5000 IR* thermobalance (*TA Instruments*), operating under air flow, at a scanning rate of 20ºC/min.

As it is shown in Figure 55, there is a strong degradation of the polymer below 400ºC, with a loss of about 80% of the mass. After this PEI is completely eliminated in a second process around 575°C.

In combination with TGA, which does not provide identification of chemical phases, FT-IR spectroscopy analysis was also conducted in order to follow the type of thermal decomposition that takes place in the polymer.

In Figure 56 are shown the spectra for samples after different thermal treatments in air. PEI undergoes an oxidant decomposition, observing at 300°C the band of carbonyl bond formation *ca* 1700 cm^{-1}, overlapped to amine bending at 1642 cm^{-1} [156]. For the rest, changes during degradation were very light. Above 400°C only a greyish residue is observed, where the band of C-C can be distinguished. The assignment of peaks for PEI is listed in Table 5.

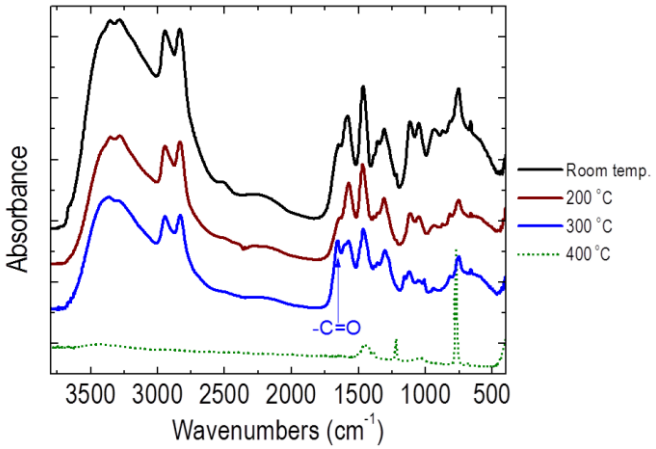

Figure 56. FT-IR spectra of SU-PEI dissolved in trichloromethane at different temperatures. IR absorption spectra in ATR mode were collected with a *Thermo Nicolet FT-IR Nexus* instrument equipped with a *Smart Endurance* device, and a DTGS detector, at a 4 cm^{-1} resolution for 128 scans.

Wavenumbers (cm^{-1})	Assignment
3300	OH, NH (stretching)
2942, 2849	CH (stretching)
1642	NH_2 (bending)
1586	NH (bending)
1463	CH_2 (bending)
1353, 1304	CH (bending)
1116, 1051	C-C, C-N (stretching)

Table 5. FT-IR spectra assignment of characteristic IR absorptions present in PEI.

A physical description of PEI at this degradation pathway after removing from the furnace also provides information about its nature. At room temperature is almost transparent with a viscous appearance. At 200°C changes color to yellow, but it is still gummy. At 300°C the color is orange but it is more rigid. In these conditions the PEI is still soluble in $CHCl_3$ but at 400°C is an insoluble brittle black ash. Above 575ºC the polymer completely disappears through a complete oxidative degradation with no remains of carbon.

Thermal stability of PEI is a great advantage, with a controllable decomposition until the film is formed and preventing the formation of individual oxides when a multicationic compound is required. Annealing above 600ºC produces a complete decomposition of the polymer in volatile species, without any remain of organic material in the sample. EDTA is also fully decomposed at these temperatures [157].

Furthermore, the slow decomposition of the polymer, at a final temperature close to the crystallization temperature of the inorganic film from an amorphous precursor, promotes the formation of the inorganic film at a very slow rate, close to thermodynamic equilibrium conditions, and promotes high crystallinity and quality.

We can distinguish among three main different growth modes for thin films [158], attending to their macroscopic deposition onto the substrate (Figure 57):

- Frank-van der Merwe (two dimensional layer by layer). This is the most desirable growth mode to achieve homogeneous thickness over the substrate. The substrate is completely covered for the first layer because the stronger attraction of deposited atoms for substrate than for among them. In this case, the second layer does not start until the first one is complete. As a result ultraflat thin films are obtained owing that film follows the morphology of substrate.
- Volmer-Weber (islands or three-dimensional). It is the opposite case to layer by layer growth. The interaction among the film atoms is stronger than with the substrate, yielding to the nucleation of cluster forming islands, so the substrate is not completely covered. This is often when film and substrate are very dissimilar materials (oxides and semiconductors/metals). As a result, these films present high roughness.
- Stranski-Krastanov (layer and islands). It is the intermediate case, and is the more common. The film growth starts as a layer by layer deposition, but after a critical thickness in which the binding energy with the surface decreases to a certain threshold, islands are formed.

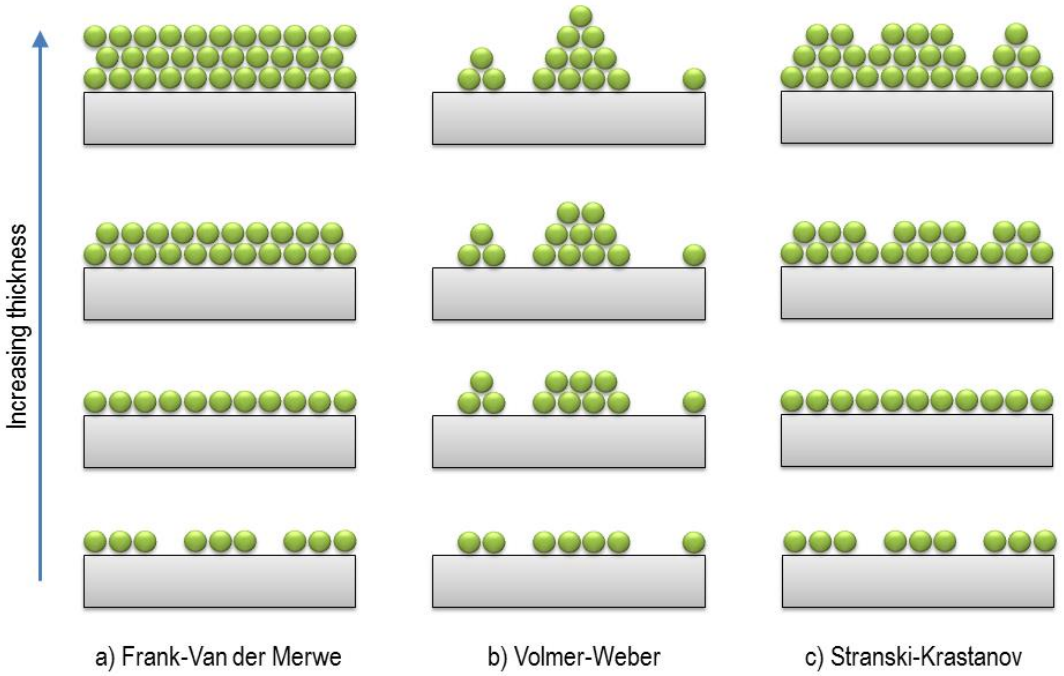

Figure 57. Schematic illustrations of the three primary growth modes for thin films: a) Fran-Van der Merwe, b) Volmer-Weber, and c) Stranski-Krastanov.

These three growth-mode models are based on thermodynamic considerations, in good agreement with quasi-thermodynamic equilibrium conditions imposed by PAD. Here, the interplay among surface energies of the film E_f, substrate E_s, and interface E_i determine the type of growth mode. The variation of the energy of the system is given by:

$$\Delta E = E_{film} + E_{interface} - E_{substrate} \tag{3.10}$$

The more negative this energy variation, the more favorable will be the layer by layer growth. Hence, in this playground is understood the importance of parameters such as surface termination and lattice mismatch, as well as other degrees of freedom to reduce the energy penalty.

In Figure 58 it is shown the actual process of thermal annealing of the films carried out in a tubular furnace.

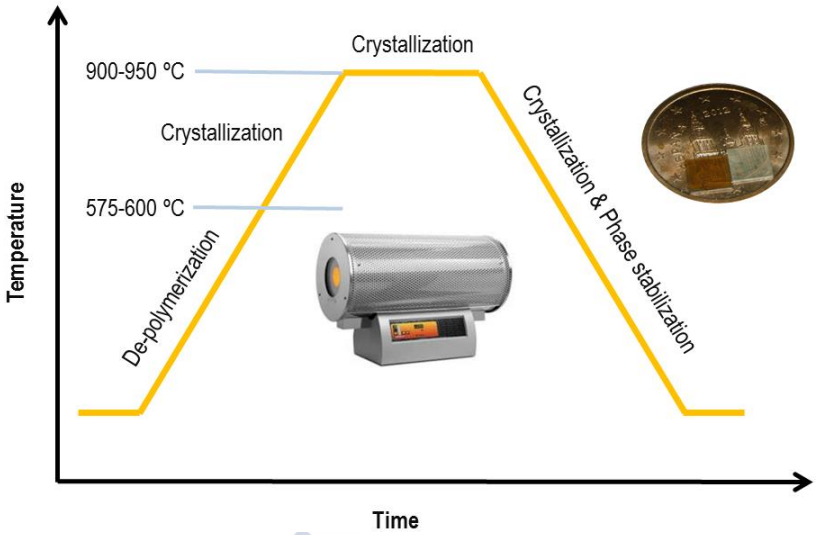

Figure 58. Schematics of the thermal treatment in PAD carried out to obtain thin films.

Given that during heat treatment two materials with differing thermal expansion coefficients are in contact is highly recommended to use slow heating and cooling ramps (< 3°C / min) to avoid cracks in the film during this bottom-up growing. In the next table are listed the thermal expansion coefficient of some typical substrates (data obtained from *CrysTec GmbH* data-sheets) and materials growth in this thesis.

Substrate		Material	
$(LaAlO_3)(Sr_2AlTaO_6)_{0.7}$	8.2	$LaMnO_3$	11.2 [159]
$SrTiO_3$	9.0	$La_{0.7}Sr_{0.3}MnO_3$	11.8 [159]
$Y:ZrO_2$ (YSZ)	9.2	$La_{0.7}Ca_{0.3}MnO_3$	10.5 [159]
$LaAlO_3$	10.0	$LaCoO_3$	15-20 [160]
$GdScO_3$	10.9	$BiFeO_3$	6.5-13 [161,162]
MgO	14.0	$SrIrO_3$	10 [163]

Table 6. Thermal expansion coefficients, α (10^{-6}/K), around temperature ranges for annealing conditions for single-crystal substrates and for some of materials synthesized in this thesis.

Moreover, structural transitions can occur in substrates within annealing temperature as in the case of room temperature rhombohedral $LaAlO_3$, in which a rhombohedral to cubic transition takes places at 544ºC.

Each material needs particular annealing conditions in terms of temperature, time and atmosphere. As in any chemical synthesis, metal precursors and gases are the reagents used in PAD and must be of the highest possible purity as they are going to react on the surface of the substrate at certain temperature forming a chemical product. Annealing is the step where the quasi-thermodynamic equilibrium growth imposed by PAD defines the film structure and properties.

4. Synthesis of multicationic thin films

The family of manganites [164], in particular $La_{1-x}Ca_xMnO_3$ [165] and $La_{1-x}Sr_xMnO_3$ [166] are an excellent playground in order to test the stoichiometric control of PAD. Their rich structural, magnetic, and transport properties, which make them so attractive for a large number of applications, are also very sensitive to minor variations to the cation ratio. Along this chapter are explained the synthesis and characterization of manganites thin films by PAD process with different composition and thickness.

4.1. $La_{1-x}Ca_xMnO_3$

Prior to growth epitaxial thin films on single-crystal substrates, we deposited $La_{1-x}Ca_xMnO_3$ films on Si (111) as polycrystalline films varying thickness and composition [167]. This effort in an accessible substrate, allowed us to define the synthesis conditions (solution concentration, spin coater parameters, temperature, time, etc.) to be used in further experiments in oxide single crystal substrates.

While the parent compound of the series, Mott insulator $LaMnO_3$ is antiferromagnetic (T_N ~ 140 K), Ca^{2+} (hole) doping increases conductivity and induces a ferromagnetic behavior reaching a maximum Curie temperature around 265 K at $x < 0.5$. However, above $x > 0.5$ antiferromagnetism predominates again up to x=1 (see Figure 66.a).

Structurally, the in-plane pseudocubic lattice parameters of this series ranges from 3.73 Å in x=1 ($CaMnO_3$) to 3.99 Å in x=0 ($LaMnO_3$), so most of these films but $LaMnO_3$ would be under tensile strain on STO. Their bulk lattice parameters as well as in-plane mismatch to STO are compiled in Table 7.

Manganite	*a* (Å)	*b* (Å)	*c* (Å)	a_{pc} (Å)	c_{pc} (Å)	*f* (%)
$CaMnO_3$	5.264	5.278	7.455	3.727	3.727	-4.55
$La_{0.25}Ca_{0.75}MnO_3$	5.354	5.352	7.548	3.785	3.774	-3.07
$La_{0.5}Ca_{0.5}MnO_3$	5.424	5.435	7.645	3.839	3.822	-1.69
$La_{0.67}Ca_{0.33}MnO_3$	5.462	5.477	7.719	3.868	3.860	-0.95
$La_{0.75}Ca_{0.25}MnO_3$	5.481	5.499	7.751	3.882	3.876	-0.59
$LaMnO_3$	5.537	5.747	7.693	3.990	3.846	+2.18

Table 7. Bulk lattice parameters (*a*, *b*, and *c*); in-plane (a_{pc}) and out-of-plane (c_{pc}) pseudocubic lattice parameters; and mismatch (*f*) with respect to STO for $La_{1-x}Ca_xMnO_3$ manganites.

The pseudocubic lattice parameters from this orthorhombic system are obtained by using the following equations:

In plane $$a_{pc} = \frac{\sqrt{a_o^2 + b_o^2}}{2} \quad (4.1)$$

Out-of-plane $$c_{pc} = \frac{c_o}{2} \quad (4.2)$$

And mismatch to substrate is obtained by using equation (2.1).

$La_{1-x}Ca_xMnO_3$ films (x=0, 0.25, 0.33, 0.50, 0.75 and 1) were synthesized on STO (001) following the process described in chapter 3. Deposition of 0.4 M solutions was performed at 4,500 rpm during 20 s, with annealing at 950ºC under O_2 flow (15 mL/min) during 2 hours.

According to XRD analysis the films so obtained are single-crystalline oriented without secondary phases. Only (00*l*) reflections are observed, with FWHM values lower than 0.1º in all films. φ scan and RSM confirm the epitaxial matching of films to STO. This XRD analysis is illustrated for $LaMnO_3$ (LMO) in Figure 59.

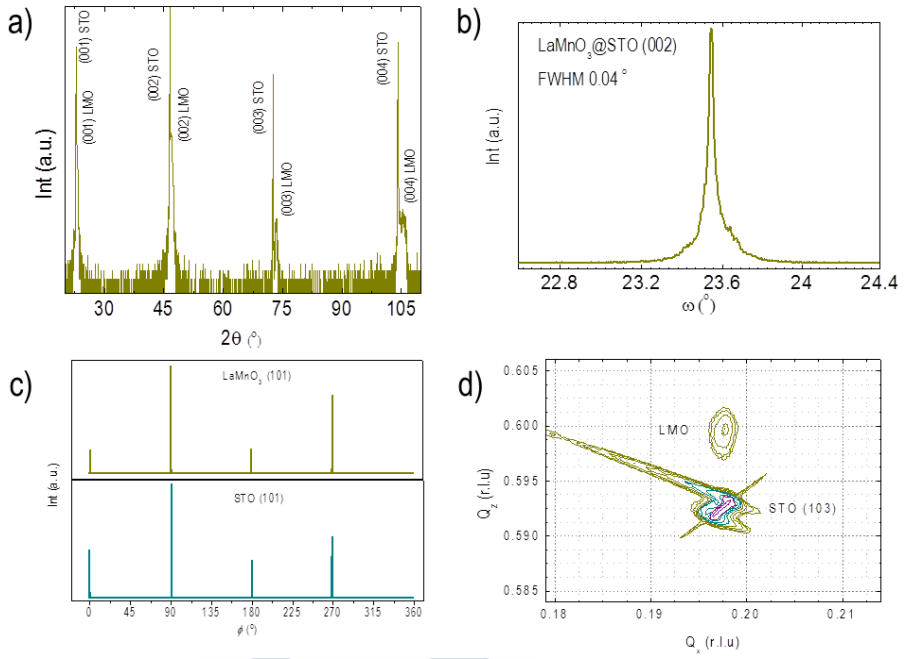

Figure 59. a) XRD pattern, b) Rocking curve, c) *φ* scan, and d) RSM of LMO on STO (001) prepared by PAD. These analyzes were performed in an *Empyrean* diffractometer according with the optics explained in section 2.2.

The evolution on the stoichiometry was studied by XRD analysis on (002) reflection (Figure 60.a), and by Energy-Dispersive X-Ray (EDX) spectroscopy on Ca emission band K_α at 3.69 keV (Figure 60.b). The results reveal that content in Ca^{2+} in films is consistent from calculated from ICP in deposited solutions.

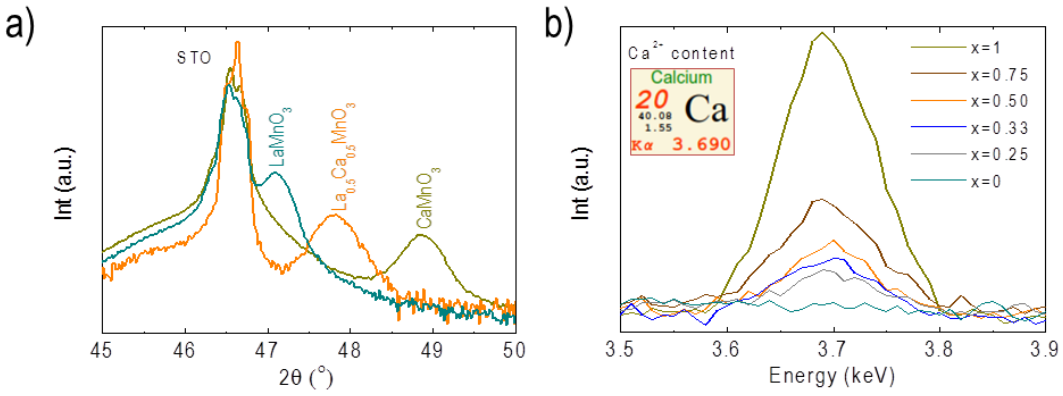

Figure 60. a) XRD pattern around (002) reflection for $La_{1-x}Ca_xMnO_3$ films with Ca^{2+} content (x) of 0, 0.5 and 1 taken in an *Empyrean* diffractometer according with the optics explained in section 2.2. b) Ca element EDX analysis at 3.69 KeV for $La_{1-x}Ca_xMnO_3$ films carried out in a SEM *Zeiss Plus* in 0-20 KeV range at 8.5 mm work distance with an *Oxford Inca* EDX microanalysis.

In these EDX analysis Ca, and not La, was selected because is not overlapped with other elements. Emission signal of La is found too close of Ti from STO substrate leading to inexactitude in quantitative determination (Figure 61).

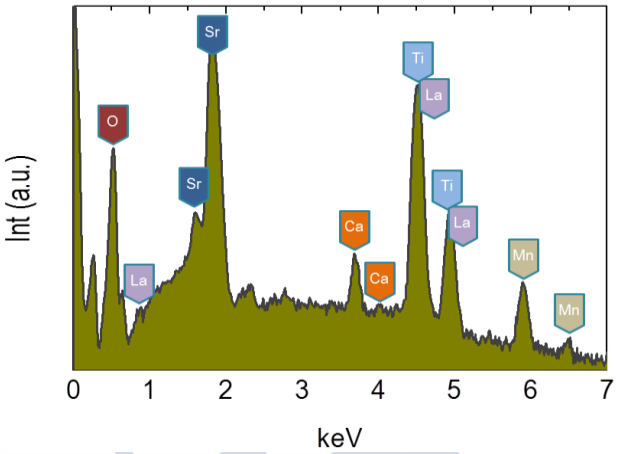

Figure 61. EDX spectrum for $La_{0.25}Ca_{0.75}MnO_3$ film on STO, where the corresponding emission bands of each element are indicated. As it can be observed La main signal is overlapped with Ti.

The lattice parameters for $La_{1-x}Ca_xMnO_3$ films as a function of Ca^{2+} content obtained from XRD and EDX are represented in figure 62. They are in a good agreement with respect to those reported in bulk [168-171] demonstrating a high structural coherence.

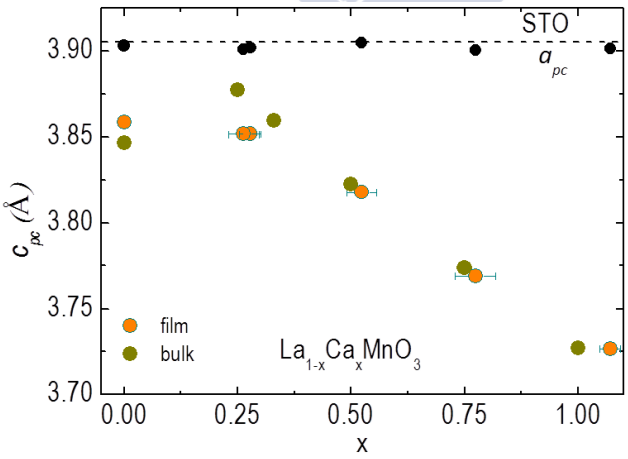

Figure 62. Out-of-plane lattice parameter as a function of Ca^{2+} content of $La_{1-x}Ca_xMnO_3$ films in comparison to bulk. The in-plane lattice parameter remains constant matched to STO.

In addition to structural quality these films cover homogenously the whole surface of the substrate. In the Figure 63 are shown two examples observed by SEM images at 25,000 X magnification. The morphology is coherent with an ordered growth of the film, similarly to an intermediate Stranski-Krastanov regime, in which the substrate is totally covered. Also in these images, markedly in LMO, La rich white dots entails a La segregation during film growth related to accommodation to STO substrate.

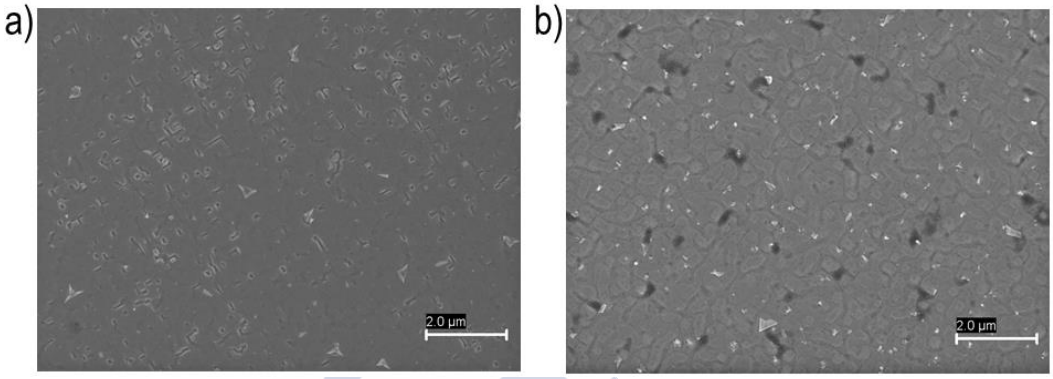

Figure 63. SEM images of a) $La_{0.75}Ca_{0.25}MnO_3$ and b) $LaMnO_3$ films taken in a *Zeiss Plus* at 3 keV conditions and 2.5 mm work distance.

Transmission Electron Microscopy (TEM) confirms the crystalline quality of films. TEM is a powerful tool that provides a detailed characterization of the crystalline quality at atomic resolution. It can provide crystallographic and composition information.

Preparation of transparent specimens for the electron beam, lamellae, is the most important part in TEM characterization. The thickness of the lamella, ≈ 150 nm thick, is crucial in order to obtain a high resolution image. There are two main ways to prepare thin films specimens, plan-view (milling of the substrate) and cross-section. The latter is the most interesting because allows to observe the interface with the substrate. On the other hand, the obtaining of lamella can be done either by combining mechanical and ion milling or just by using Focused Ion Beam (FIB). FIB is a very sophisticated tool but can induce amorphization in some samples. The mechanical milling is very laborious and delicate, sequentially varying the type of disc according to roughness of the polish sample. The first part of this preparation involves cutting the film at half (or smaller portions) and pasting both halves film-faced through an epoxy resin (e.g. M-BOND 650), that are pressed over a hot plate at 100ºC during a whole day. Then, this pasted sample is cut in smaller pieces of 650 µm width with a diamond saw or wire. Finally, lamellae are polished in both faces, firstly mechanically by diamond discs starting with a disc of 9 µm rough, and finally in a Precision Ion Polishing System (PIPS) mounted into a Cu disc at 5 keV following the thinning in a camera (Figure 64). Polishing

depends on hardness of each material (e.g. $LaAlO_3$ is harder than $SrTiO_3$), what affects to the time and conditions of the process.

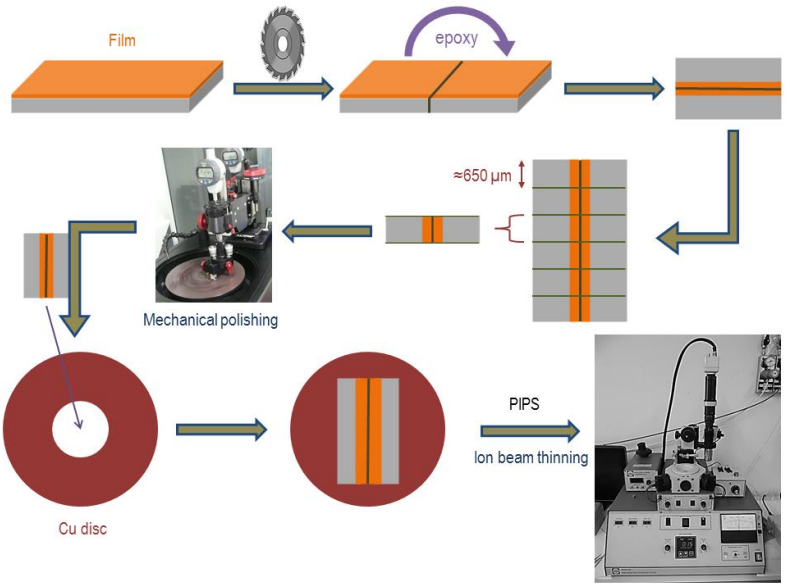

Figure 64. Flow chart for obtaining a cross-section specimen for TEM from a film by combining mechanical and ion beam thinning.

As it can be observed in Figure 65 from a cross section lamella from a LMO sample, the octahedral ordering of PAD film is perfectly crystalline, with an abrupt interface comparable to classical physical deposition methods.

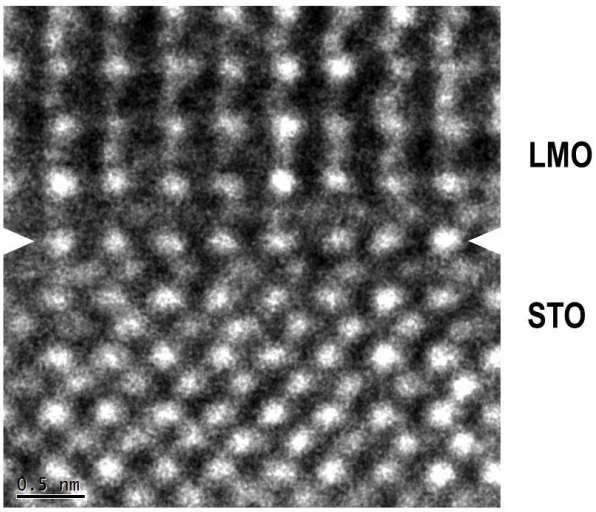

Figure 65. High-resolution cross-sectional TEM image of a LMO film deposited by PAD on STO (001).

Attending to the phase diagram of $La_{1-x}Ca_xMnO_3$ (Figure 66.a) we focused on the characterization of the magnetic and transport at x<0.5, where interesting properties such as ferromagnetism, metallicity and magnetoresistance are. The magnetization increases in this range as a function of Mn^{3+} content as in the bulk due to double exchange mechanism between Mn^{3+} and Mn^{4+} [172]. However, the large value of M and T_C in $LaMnO_3$ represents an unexpected result both well above of their bulk value. The hysteresis loops also show an increasing coercive field inversely proportional to the Mn^{3+} content.

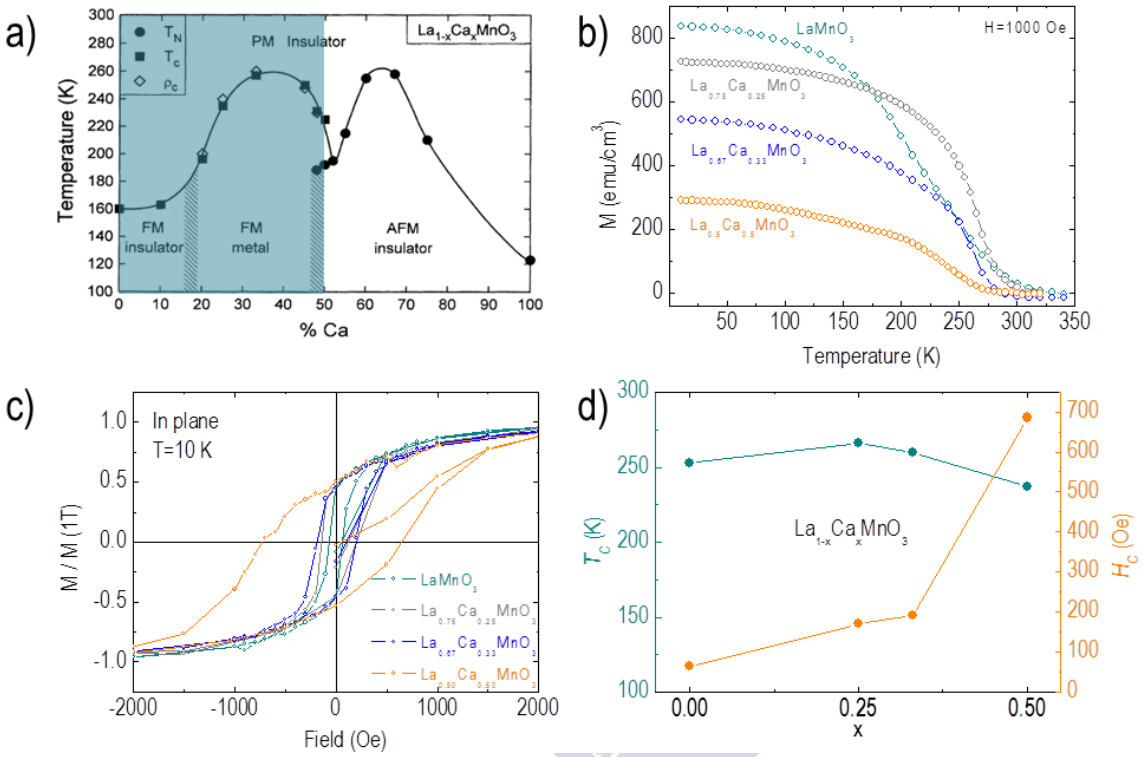

Figure 66. a) Magnetic and electronic transport phase diagram of $La_{1-x}Ca_xMnO_3$, taken from [165]. b) Temperature dependence of the magnetization and c) hysteresis loops for $La_{1-x}Ca_xMnO_3$ films. d) Curie temperature and Coercive field as a function of the Ca content for the same films.

The hysteresis loops at 10 K with applied magnetic field parallel and perpendicular to the film are shown in Figure 67. From these measurements, the magnetization is in the plane of the film.

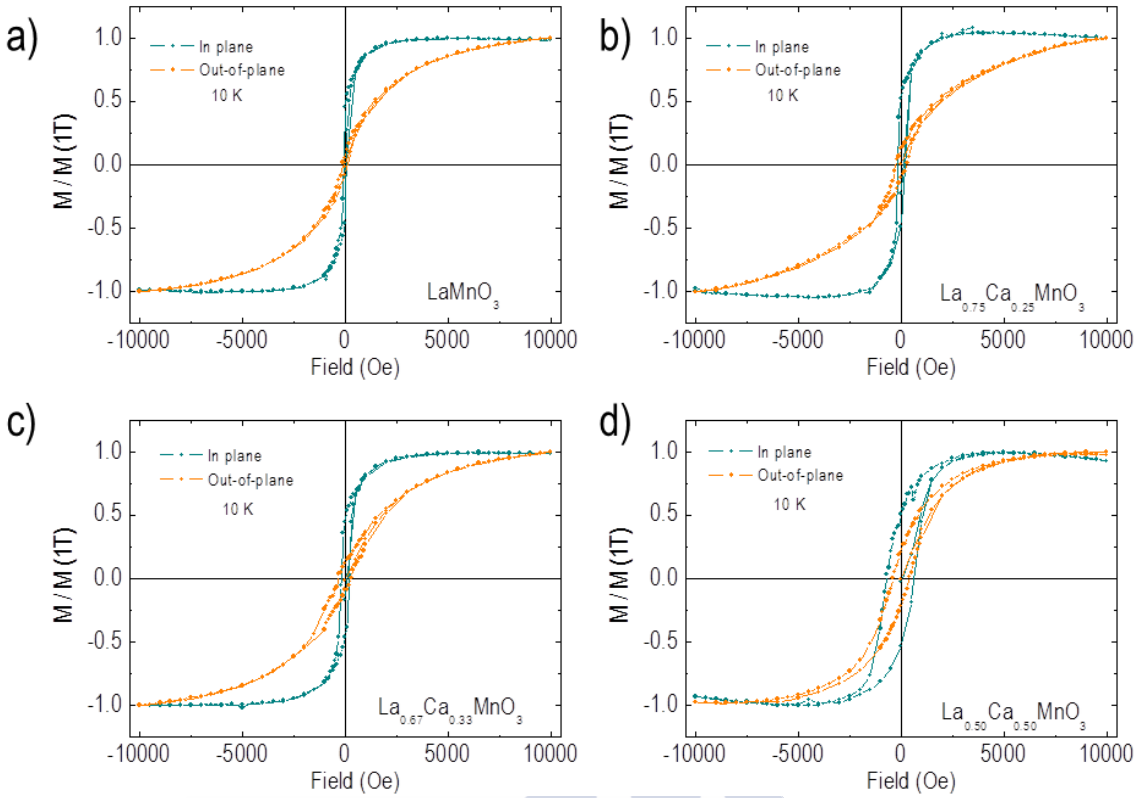

Figure 67. In plane (cyan) and Out-of-plane (orange) hysteresis loops for a) $LaMnO_3$, b) $La_{0.75}Ca_{0.25}MnO_3$, c) $La_{0.67}Ca_{0.33}MnO_3$, and d) $La_{0.5}Ca_{0.5}MnO_3$ films.

The magnetic characterization of the samples in this thesis was carried out in a Superconducting Quantum Interference Device (SQUID) magnetometer type (Magnetic Property Measurement System (MPMS) *EverCool* from *Quantum Design*. The DC magnetic field can be run from -7 to 7 Tesla and the temperature from 1.9 to 400 K with a measurement resolution of 10^{-6} emu (10^{-9} A.m^{-2}).

The electronic transport measurements confirms the bulk-like behavior in all series, except again for $LaMnO_3$, which shows a metallic behavior ($d\rho/dT>0$) with a metal-insulator transition close to room temperature.

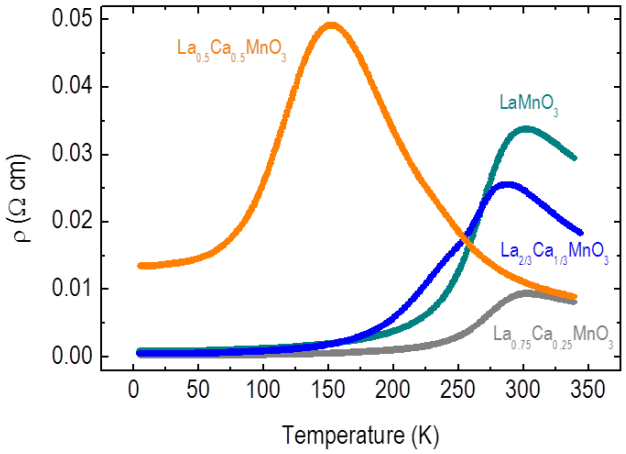

Figure 68. Temperature dependence of the resistivity for $LaMnO_3$, $La_{0.75}Ca_{0.25}MnO_3$, $La_{0.67}Ca_{0.33}MnO_3$, and $La_{0.5}Ca_{0.5}MnO_3$ films.

The magnetoresistance at H=1.2 T is shown in Figure 69. In the case of LMO MR reaches approximately 10 % at 300 K applying a magnetic field of 1.2 T. By applying a magnetic field the resistivity decreases, markedly close to ferromagnetic transition temperature in which this field orders the magnetic moments.

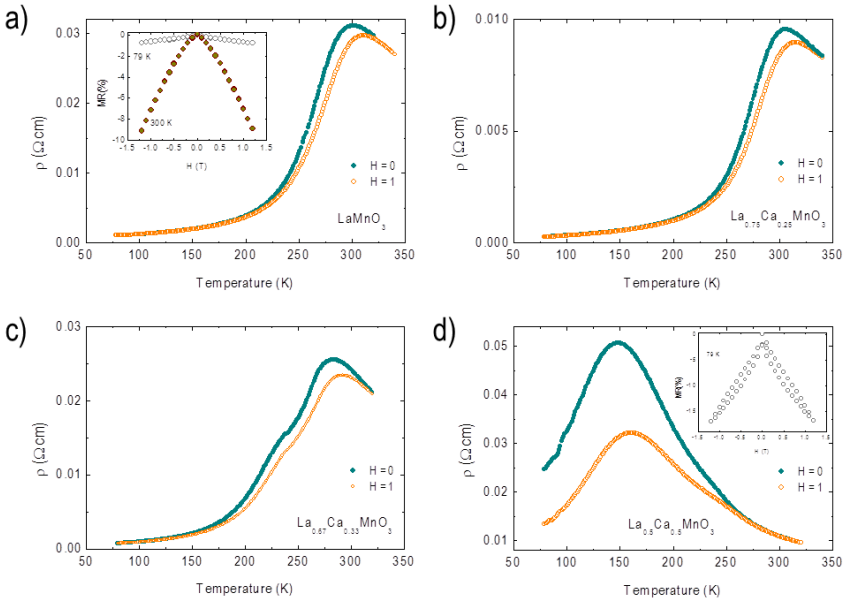

Figure 69. Temperature dependence of the resistivity at H = 0 T (cyan) and at H =1 T (orange) for a) $LaMnO_3$, b) $La_{0.75}Ca_{0.25}MnO_3$, c) $La_{0.67}Ca_{0.33}MnO_3$, and d) $La_{0.5}Ca_{0.5}MnO_3$ films. In inset the magnetoresistance for LMO at 79 and 300 K, and for $La_{0.5}Ca_{0.5}MnO_3$ at 79 K.

Electrical resistivity measurements were performed in a four-contact configuration in order to eliminate any external contribution such as impedance of wires or contact resistances. In order to obtain this configuration, the films were properly lithographied by using Ar etching during 10 min. at 160 μA and 9.5 KeV. The useful area was protected with a molybdenum stencil mask with 300 x 1,500 μm dimensions (Figure 70.a). In order to achieve a good ohmic contact, Cr/Au (5 nm/20 nm) pads were coated over the sample by sputtering at 200 μA and 6 KeV before soldering gold wires (Figure 70.b). Etching and coating were performed in a *Gatan* Precision Etching and Coating System (PECS). After this preparation the samples were annealed during 1h at 400 ºC under O_2 atmosphere (15 mL/min) in order to prevent any possible transport contribution of STO due to oxygen vacancies doping [173] generated during etching process.

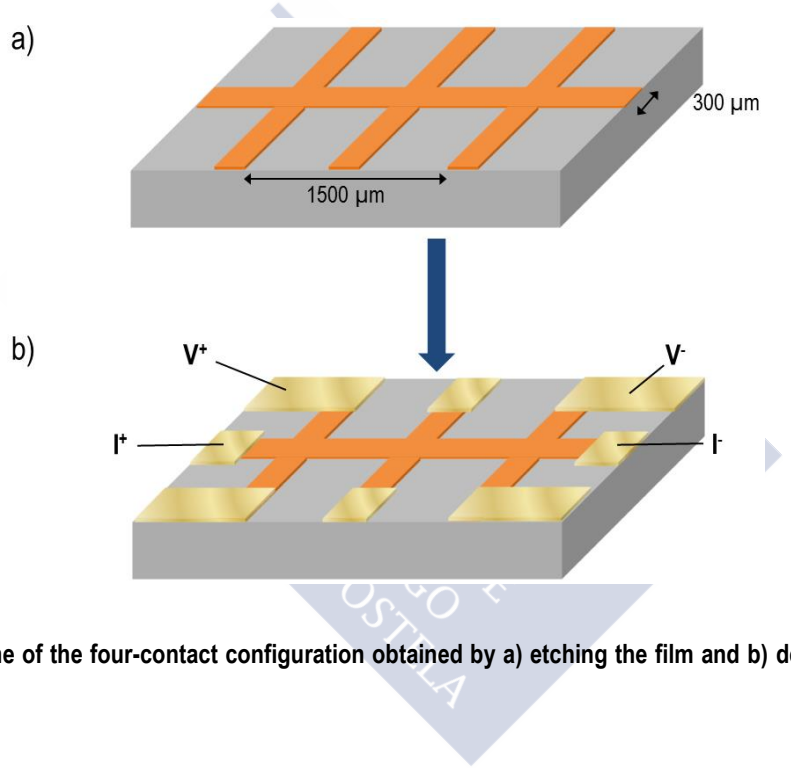

Figure 70. Scheme of the four-contact configuration obtained by a) etching the film and b) depositing Cr/Au contact pads.

In this configuration, a current *I* is passed across the patterned film, and the voltage difference ΔV between two points of the sample is measured in order to obtain the resistance:

$$R = \frac{\Delta V}{I} = \frac{V^+ - V^-}{I} \qquad (4.3)$$

From the experimental measurement of the resistance the resistivity can be obtained taken into account the geometrical parameters;

$$\rho = R\frac{A}{L} = R\frac{t.w}{L} \tag{4.4}$$

where *L* is the distance between voltage contacts (1,500 µm), and *A* the transverse section to the current, defined by the thickness of the film (*t*) and the width of the channel (300 µm).

The MR (with the magnetic field applied parallel to the electric current) is expressed as:

$$\%MR = \frac{\rho(H) - \rho(0)}{\rho(0)}.100 \tag{4.5}$$

where *ρ(H)* and *ρ(0)* are the electrical resistivity under field and without field, respectively.

Optic photolithography was also used in PAD films to obtain other configurations and combined with dry or wet etching. With this purpose a *Midas MDA-400 LJ* mask aligner was employed along with photoresist (*AZ 7210* or *AZ 3027*), and *AZ 726 MIF* developer. The first step in this process is the deposition of the resin on the sample by spin-coating to achieve a 1 µm thick resist layer at 4000 rpm during 30 s. Then this layer is baked in a hot plate during 1 min, between 90-110ºC depending on the resist. A mask is properly aligned on the sample to perform the selected pattern and exposed under a UV lamp at 17 mW/cm^2 during 30 s. Another baking can be done before of 60 s developing step. Finally the specimen is dry etched with Ar or wet etched in an acid solution. In wet etching, acid concentration and time have to be controlled to prevent excessive etched of film. In our case, very dilute solutions of 0.05 M HCl during 1-2 min were adjusted to remove 20-50 nm thick films. By this process well defined patterns were obtained (Figure 71).

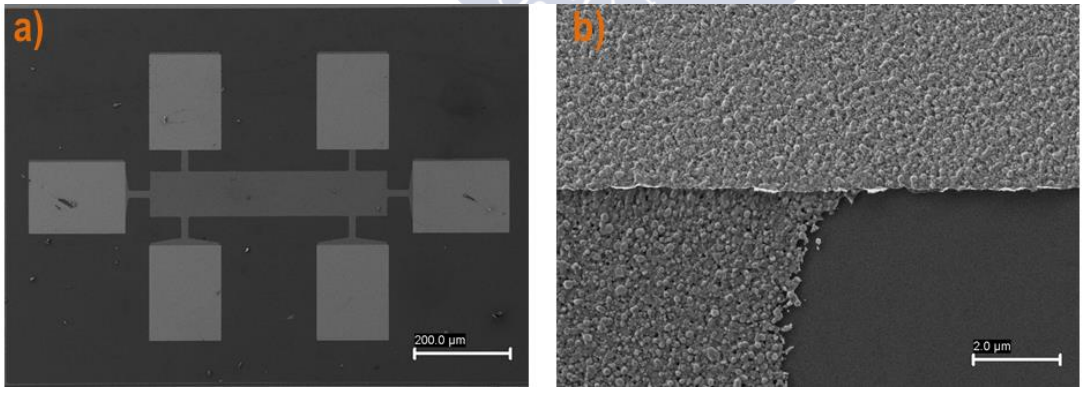

Figure 71. a) SEM image of a Hall bar patterned by wet etching. b) 25,000 X magnified SEM image of the same pattern to show in detail the etched zone limiting to Au pad.

USC
UNIVERSIDADE
DE SANTIAGO
DE COMPOSTELA

5. Comparison of the structural and magnetic properties of thin-films deposited by PAD and PLD

The aim of this chapter is to demonstrate that PAD can modulate the structural and physical properties of thin films. Growth of the film in PAD occurs in quasi-equilibrium thermodynamic conditions, in contrast to physical methods, like PLD or sputtering, determined by kinetic aspects far from thermodynamic equilibrium.

In the next paper, we study this effect on $La_{0.7}Sr_{0.3}MnO_3$ (LSMO). LSMO is the most common oxide used for spin-injection in oxide-based spintronic devices, and magnetic anisotropy determines to a large extend its functionality. We show that the magnetic anisotropy can be modified by controlling the deposition conditions. The strain relaxation determines the rotation patterns of MnO_6 octahedra in LSMO.

We followed this analysis by structural distinction from XRD and by magnetic anisotropy from ferromagnetic resonance (FMR) experiments. FMR increases the sensitivity by orders of magnitude and gives access to the study of the magnetic properties of ultrathin films, allowing to study subtle structural distortions difficulty to distinguish by X-Ray analysis.

This study demonstrates that the structural and magnetic quality of the films deposited by PAD is comparable to obtained by PLD, with the advantage that no high vacuum is required for deposition.

5.1. Submitted to Journal of Physics D: Applied Physics

Thermodynamic conditions during growth determine the magnetic anisotropy in epitaxial thin-films of $La_{0.7}Sr_{0.3}MnO_3$

José M. Vila-Fungueiriño

Cong Tinh Bui

B. Rivas-Murias

E. Winkler

J. Milano

J. Santiso

F. Rivadulla

Thermodynamic conditions during growth determine the magnetic anisotropy in epitaxial thin-films of $La_{0.7}Sr_{0.3}MnO_3$.

J. M. Vila-Fungueiriño,[1] Cong Tinh Bui,[1] B. Rivas-Murias,[1] E. Winkler,[2] J. Milano,[2] J. Santiso,[3] and F. Rivadulla[1,*]

[1] *Center for Research in Biological Chemistry and Molecular Materials (CIQUS), University of Santiago de Compostela, 15782 Santiago de Compostela, Spain*

[2] *Centro Atómico Bariloche, CNEA-CONICET, 8400 S.C. de Bariloche, Río Negro, Argentina*

[3] *Catalan Institute of Nanoscience and Nanotechnology (ICN2), CSIC and The Barcelona Institute of Science and Technology, Campus UAB, Bellaterra, 08193 Barcelona, Spain*

(Dated: March 4, 2016)

The suitability of a particular material for use in magnetic devices is determined by the process of magnetization reversal/relaxation, which in turn depends on the magnetic anisotropy. Therefore, designing new ways to control magnetic anisotropy in technologically important materials is highly desirable. Here we show that magnetic anisotropy of epitaxial thin-films of half-metallic ferromagnet $La_{0.7}Sr_{0.3}MnO_3$ (LSMO) is determined by the proximity to thermodynamic equilibrium conditions during growth. We performed a series of X-ray diffraction and ferromagnetic resonance (FMR) experiments in two different sets of samples: the first corresponds to LSMO thin-films deposited under tensile strain on (001) $SrTiO_3$ by Pulsed Laser Deposition (PLD; far from thermodynamic equilibrium); the second were deposited by a slow Chemical Solution Deposition (CSD) method, under quasi-equilibrium conditions. Thin films prepared by PLD show a in-plane cubic anisotropy with an overimposed uniaxial term. A large anisotropy constant perpendicular to the film plane was also observed in these films. However, the uniaxial anisotropy is completely suppressed in the CSD films. The out of plane anisotropy is also reduced, resulting in a much stronger in plane cubic anisotropy in the chemically synthesized films. This change is due to a different rotation pattern of MnO_6 octahedra to accomodate epitaxial strain, which depends not only on the amount of tensile stress imposed by the STO substrate, but also on the growth conditions. Our results demonstrate that the nature and magnitude of the magnetic anisotropy in LSMO can be tuned by the thermodynamic parameters during thin-film deposition.

PACS numbers:

I. INTRODUCTION

Recent developments in thin-film growth showed the enormous potential of epitaxial stress to tune the properties of thin films at a very fundamental level. In perovskite oxides, ABO_3, strain accommodation occurs through a complex rotation and deformation of corner sharing BO_6 octahedra[1–3]. This changes the delicate balance of bond-distances and angles and therefore the relative orbital occupation supporting a given magnetic or electrical interaction[4–10]. Interfacial phenomena like heterogeneous catalysis reactions[11], and electronic reconstructions occurring at functional interfaces[12], are also influenced by these effects.

An interesting example given its scientific relevance is the case of half-metallic ferromagnet $La_{0.7}Sr_{0.3}MnO_3$ (LSMO). Growing epitaxial LSMO on cubic (001) $SrTiO_3$ (STO) results in an orthorhombic (with a monoclinic distortion) unit cell of the magnetic oxide[1,13] . Biaxial tensile stress (a=b>c) imposed by the cubic substrate to the incommensurate rhombohedral lattice of bulk LSMO induces an equal in-(out-) phase rotation of the MnO_6 octahedra along the a-(b-) axis, and no rotation along the c-axis ($a^+a^-c^0$ in the Glazer notation[14]). Sandiumenge et al.[3] proposed a complex relaxation pattern in which several phases with different symmetry can be distinguished in epitaxial LSMO below 25 nm. These authors identified a critical thickness $\approx$ 2 nm for the build up of a shear strain field, which induces a rhombohedral twined structure and a progressive compression of the c-axis up to $\approx$10 nm. Beyond this thickness, an elastic deformation of the lattice without any perturbation of the octahedral tilting sets up to $\approx$25 nm. Vailionis et al.[15] confirmed that the mechanism of strain relaxation changes along the film thickness, due to a combined effect of symmetry mismatch close to the interface, and lattice mismatch in the "bulk" of the film. They showed that in the first $\approx$two unit cells, stress suppresses octahedral rotations and expands the c-axis parameter; farther away from the interface, tilting of MnO_6 octahedra reduce the c-axis parameter consistent with in-plane tensile strain.

An important question is whether this complex relaxation pattern is intrinsic to the accommodation of biaxial tensile stress in LSMO, or if it can be modified by growing the films under very different conditions, thus allowing the system to explore different relaxation paths. After all, previous studies were performed on samples synthesized by PLD and sputtering, far from thermodynamic equilibrium. Here we describe a comparative X-ray diffraction (XRD) and Ferromagnetic resonance (FMR) study of LSMO thin films deposited on STO by Pulsed Laser Deposition (PLD; far from thermodynamic equilibrium), and by a slow chemical deposition method (CSD; close to thermodynamic equilibrium). Our results

demonstrate that magnetic anisotropy in LSMO depends on the conditions during film growth. As a result, a different patter of rotation of MnO_6 octahedra is accomodated in epitaxial films synthesized by CSD.

II. EXPERIMENTAL DETAILS

Thin films of LSMO of different thicknesses were grown on (001) TiO_2-terminated $SrTiO_3$ (STO) substrates. For the PLD filmms we used an excimer laser (F-Kr, 248 nm) operating at 5 Hz and a fluence of 0.8 J/cm^2. The films were deposited at 800 °C and 200 mTorr of O_2. For chemically grown films (CSD), a precursor solution was spun-coated on similar substrates, and annealed at high temperature, as described in[16]. The thickness of both type of films was determined by X-ray reflectivity and TEM analysis of cross-section lamellae. X-band($\omega/2\pi$ ~9.4 GHz) FMR experiments were performed in a Bruker-X spectrometer at different temperatures, with the magnetic field applied rotating paralell to the film-plane.

III. RESULTS AND DISCUSSION

In Figure 1 we show a summary of structural results representative of the quality of the samples studied in this work. X-ray reciprocal space maps (RSM) around the (103) reflection of the perovskite for ≈ 20 nm thick films show that they grow with in-plane lattice parameters well matched to the STO substrate, and without evidence of lattice relaxation (Figure 1a), c)). This is true for every film studied in this work, irrespective of the thickness or the deposition method (CSD or PLD). A high-resolution cross-section TEM image of a thin film of LSMO synthesized by CSD is shown in Figure 1b). The image is representative of the good crystalline quality and abrupt interfaces of all the CSD films reported in this work.

The dependence of the lattice parameters on the thickness is shown in Figure 1d). The c-axis length shows a non-monotonic dependence with the film thickness, passing through a minimum between 10 and 15 nm. Similar behavior was previously reported by Sandiumenge et al.[3] for LSMO films synthesized by rf-sputtering. These authors suggested that t_m marks a crossover from a monoclinic to a homogeneously strained rhombohedral phase. Our results show that the existence of this minimum occurs for PLD and CSD samples, therefore suggesting a universal relaxation mechanism depending only on the total strain imposed by the substrate. However, the incommensurability of rhombohedral LSMO to the cubic (001) surface of STO has been suggeseted to result in an orthorhombic symmetry with a monoclinic distortion ($P2_1/m$)[13]. In order to identify the crystal structure in our films, we have performed a careful XRD analysis around different half order reflections. (H/2, K/2, L/2) reflections are characteristic of a monoclinic or triclinic symmetry, with H=K=L being an extinction for the rhombohedral R-3C group. For the 20 nm thick sample prepared by PLD, we observed a clear signal around the (1/2,1/2, 1/2) and (1/2, 1/2, 3/2) reflections, as shown in Figure 2. These are consistent with a rhombohedral (R-3c) phase, with a monoclinic distortion. Although the (1/2,0,1) and (1,0,1/2) reflections have not been observed in our films, a orthorhombic phase cannot be completely discarded due to the small intensity characteristic of these reflections, particularly in thin-films. On the other hand, half order reflections at L=3/2 and absence at L=1/2 in films prepared by CSD are consistent with a dominant rhombohedral (R-3c) phase. Also, from the analysis of in-plane (200) and (110) peaks, a fully structural coherence with the substrate is observed along the whole thickness of the films prepared by CSD (see Figure 3). No satellites peaks or diffuse scattering associated to twinnigs or strong mosaicity are observed in these samples.

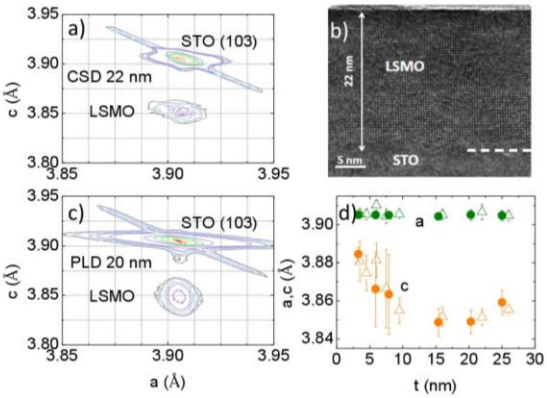

FIG. 1: X-ray maps around the (103) Bragg reflection of the perovskite for two LSMO thin-films deposited on STO by CSD (a) and PLD (c). TEM image of a cross-section lamella of a LSMO thin-film synthesized by CSD (b). The evolution of lattice parameters for several samples of different thicknesses are shown in (d).

Given the equal in-plane tensile stress impossed by the substrate along the a/b directions, these structural results therefore suggests a different rotation pattern of the MnO_6 octahedra to accommodate the tensile stress in samples synthesized by CSD with respect to PLD. We want to remark that this result is reproducible in different samples prepared from CSD under similar conditions.

The structural difference reported in Figure 2 is also manifested in the magnetic properties of the CSD and PLD films (see Figure 4). The magnetic moment at saturation and the Curie temperature (T_c) of ≈ 20 nm thick films are close to the bulk values (590 emu/cm^3 and 350 K) and are very similarity in both sets of samples, discarding any significant variation in their stoichiometry.

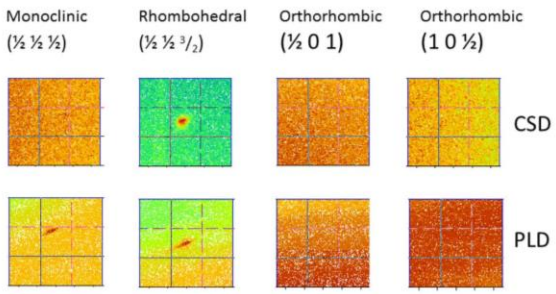

FIG. 2: Half-order Bragg reflections for thin films prepared by CSD (22 nm, top) and PLD (20 nm, bottom) respectively. Different reflections characteristic of different crystallographic phases are analyzed.

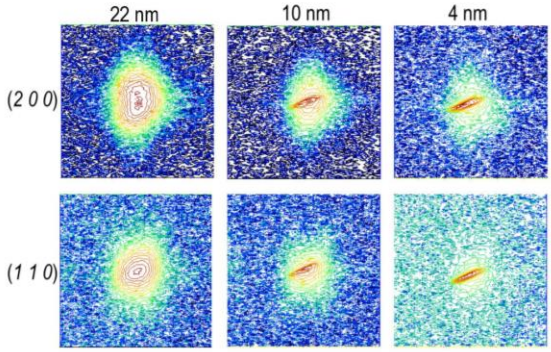

FIG. 3: In plane (200) and (110) Bragg reflections for thin films of LSMO prepared by CSD, with different thickness.

However, the coercive field (H_c) shows a completely different behavior: while the samples synthesized by PLD show a very small, bulk-like, $H_c \approx$ 50-100 Oe, it increases by an order of magnitude in the films synthesized by CSD. Therefore, the change in H_c probably implies different magnetocrystalline anisotropy between the CSD and PLD films. This could be due to differences in the strength of Mn-O-Mn exchange interactions along different directions of the crystal, as a result of the structural differences identified before. However, to give a definitive proof of this subtle structural distortion in thin-films prepared by different methods is very challenging using conventional laboratory XRD equipment.

To avoid this difficulty, the evolution of the structural

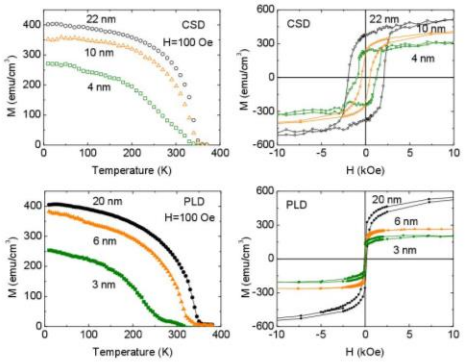

FIG. 4: Temperature and field dependence (at 10 K) of the magnetization for CSD (top) and PLD (bottom) thin films. The hysteresis loops were measured at 10 K with the magnetic field in the film plane along the (100) axis of STO. Saturation of the magnetization occurs at H<1.5 T.

parameters with thickness was studied indirectly by ferromagnetic resonance. FMR is a technique very sensitive to small variations in the magnitude of the different magnetic anisotropy terms. Different rotation patterns of the MnO_6 octahedra along different directions of the crystal will change the orbital overlap and, through spin-orbit coupling also change the magnetocrystalline anisotropy of the films. We will show that these changes measured by FMR can be correlated with the structural distortions in the films.

The angular dependence of the resonance field (H_r) in a FMR experiment can be evaluated at the magnetization equilibrium angles, θ_0 and ϕ_0 for the different orientation of the magnetic field[17]:

$$\left(\frac{\omega}{\gamma}\right)^2 = \frac{1}{M^2 \sin^2\theta}\left[\frac{\partial^2 F}{\partial\theta^2}\frac{\partial^2 F}{\partial\phi^2} - \left(\frac{\partial^2 F}{\partial\theta\partial\phi}\right)^2\right]_{\theta_0,\phi_0} \quad (1)$$

where ω is the angular frequency, M is the saturation magnetization, F is the free energy of the system and $\gamma = g\mu_B/\hbar$, where g is the gyromagnetic factor and μ_B is the Bohr magneton. Based on the structural results, three different anisotropy terms were included in the free energy expression: a biaxial in plane anisotropy constant K_4^{IP}, an in plane uniaxial anisotropy constat K_u, and a perpendicular out of plane anisotropy constant K_{out} along [001][18]:

$$F = -\mu_0 \mathbf{H}.\mathbf{M} + \frac{\mu_0}{2}M^2\cos^2\theta - \frac{K_4^{IP}}{4}\sin^4\theta\sin^2 2\phi - K_{out}\cos^2\theta + K_u\sin^2\theta\cos^2(\phi - \frac{\pi}{4}) \quad (2)$$

where the first and second terms correspond to the Zeeman and demagnetization energy, respectively. The

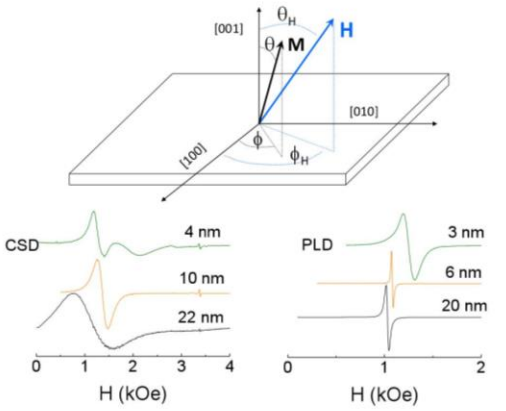

FIG. 5: Top: Scheme of the coordinate system used in Eq.1 and 2 related to the crystal axis of the STO substrate. Bottom: FMR lines for thin-films of LSMO of different thickness, synthesized by CSD (left) and PLD (right). The experiments were performed at 200 K.

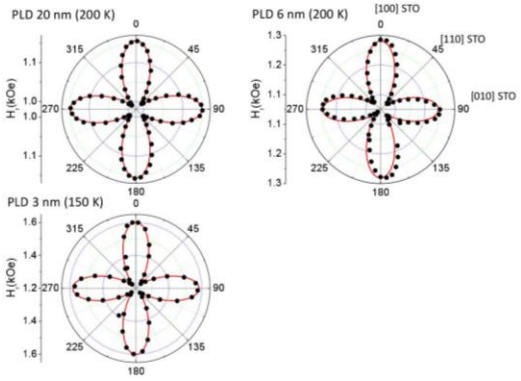

FIG. 6: In-plane angular dependence (ϕ_H=0-360°, θ_H=90°) of the PLD films resonance field, H_r. The spectra were acquired at 200 K, except for the thinnest sample that was taken at 150 K to ensure a good magnetization of the sample. The continuous lines correspond to the best fit numerically obtained from Eq. 1 and 2 (see text).

vacuum permeability is given by μ_0, and θ and ϕ are the polar and azimuthal angles of the magnetization vector, according to the scheme of Figure 5. In this way the values of K_4^{IP}, K_u, and K_{out} can be determined from fittings of experimental $H_r(\theta,\phi)$ curves by solving self-consistently Eq. (1) and (2).[19]

Following the formalism explained above, the thickness dependence of the magnetocrystalline anisotropy in our films were obtained from FMR experiments with H rotating in the plane of the films, i.e. ϕ_H=0-360°, θ_H=90°. The experiments were performed at 200 K, except for the thinner samples, which were taken at 150 K to ensure that the samples are completely magnetized at the resonance field. The FMR spectra show a single Lorentzian line in all cases, except for thinner CSD films (see Figure 5). In this case two broad overimposed lines precludes the accurate analysis of their resonance field, so we excluded these samples from the discussion.

The angular dependence of $H_r(\phi_H, \theta_H$=90°) is shown in Figures 6 and 7. All samples show a clear biaxial anisotropy with the easy axis along the < 110 > direction of STO (the diagonal directions of the (001) substrate), and the hard axis coinciding with the < 100 > directions of STO (the sides of the substrates), which is in agreement with previous reports[20,21]. Note that contrary to magnetization, in a FMR experiment the maximum and minimum of H_r mark the hard and easy magnetization axis directions, respectively. The fitting to Eq. (1) and (2) is also shown as continuous lines over the experimental data. To improve the accuracy of the fitting, the values of the saturation magnetization were obtained from the experimental M(H) measurements in each sample, at the same temperature as the FMR experiments. Also the $g-$factor was set to $g = 2.0$, as generally observed in bulk $La_{0.7}Sr_{0.3}MnO_3$[22,23].

The anisotropy constants obtained from the fittings are listed in Table I. All PLD films, irrespective of their thickness, are characterized by a biaxial anisotropy constant $K_4^{IP} \approx 2\,kJ/m^3$, plus an order of magnitude smaller uniaxial anisotropy K_u. The existence of these two anisotropy terms was previously reported from magnetization measurements in LSMO under tensile strain by several authors[1,20,24,25]. The monoclinically distorted unit cell of LSMO results from a different rotation pattern of the MnO_6 octahedra along the < 110 > axis ($a^+a^-c^0$). This produces an important difference in the magnitude of the orbital overlap along the equivalent < 110 > easy axis directions, introducing the extra uniaxial anisotropy term. We also identified fro this analysis an important out of plane anisotropy constant K_{out}. This term may have its origin in the contribution of different factors, like magnetocrystalline anisotropy[18,26], interface effects[27], domain shape[28], or most probably in this case, interfacial stress[29]. Although this effect is normally neglected, we show here that it can be an appreciable contribution in epitaxially stressed films.

On the other hand, the situation is completely different in the films synthesized by CSD: the value of K_4^{IP} is much larger in these films compared to PLD, and most important, the uniaxial anisotropy term vanishes, $K_u \approx 0$. The out of plane anisotropy constant K_{out} is also much smaller than in the PLD films, reflecting a different contribution from interfacial epitaxial stress. A larger in-plane cubic anisotropy is in qualitative agreement with larger in-plane coercivity, as observed in Figure 4. However, the estimated $H_C \sim 2K_{ip}^4/M$ for these films is in the 80-200 Oe range, smaller than observed, which calls for

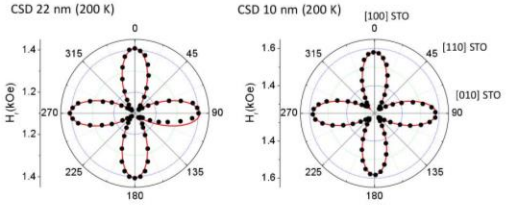

FIG. 7: In-plane angular dependence (ϕ_H=0-360°, θ_H=90°) of the CSD films resonance field, H_r. The spectra were acquired at 200 K. The continuous lines correspond to the best fit numerically obtained from Eq. 1 and 2 (see text).

TABLE I: Anisotropy energies obtained from the fits of the FMR curves and the corresponding saturation magnetization for the PLD and CSD films.

	t	K^4_{ip}	K_u	K_{out}	M
	nm	kJ/m^3	kJ/m^3	kJ/m^3	emu/cm^3
PLD					
	3	2.0(2)	0.10(1)	30(3)	200
	6	1.3(1)	0.25(3)	60(6)	260
	20	2.3(2)	0.10(1)	40(4)	580
CSD					
	10	3.5(3)	0	10(1)	440
	25	4.5(5)	0	5.0(5)	590

further relevant effect of magnetic inhomogeneities which could act as pinning centers for domain walls[30]. This is also consistent with the much wider FMR lines observed in CSD with respect to PLD films.

Following the argument before, the absence of K_u in CSD films indicate a similar orbital overlap along the $< 110 >$ axis, which in turn requires an equivalent rotation of the MnO_6 octahedra along the a and b axis. The most plausible possibility is $a^+a^+c^0$ (Glazer tilt system number 16), compatible with unit cell parameters a=b>c under tensile stress (tetragonal, space group $I4/mmm$) and our previous X-ray analysis (see Figure 2). The results of CSD are then consistent with an elastic deformation of LSMO, without any significant anisotropy in the octahedral tilting along the direction of the easy axis.

The arrangements of MnO_6 octahedra compatible with the analysis of the experimental FMR and XRD in epitaxial films of LSMO synthesized by PLD and CSD are shown in Figure 8.

In summary, we have demonstrated that the characteristic in-plane uniaxial component of the magnetic anisotropy can be completely suppressed in chemically

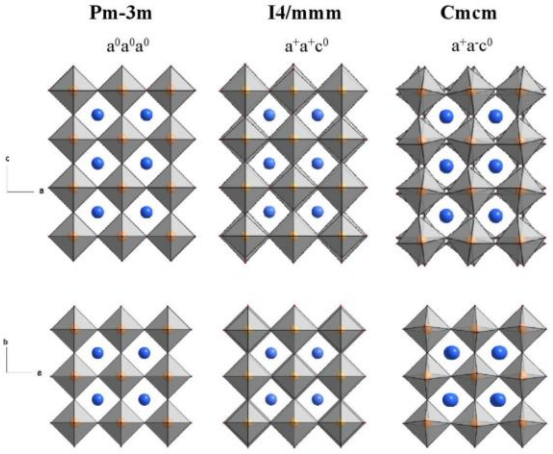

FIG. 8: Rotation patern of the MnO_6 octahedra for the space groups adopted by the epitaxial LSMO thin-films synthesized by PLD ($Cmcm$) and CSD ($I4/mmm$). The situation for cubic STO is also included ($Pm-3m$), for comparison.

prepared thin-films of LSMO. This implies different mechanisms of octahedral rotation to accommodate the biaxial tensile stress, depending on the growth conditions. Magnetic anisotropy determines the switching and relaxation of magnetization, and therefore the results presented here are not only interesting from a fundamental point of view, but they must be considered for applications of half-metallic ferromagnet LSMO in different types of devices. Finally, we would like to remark the enormous possibilities offered by the sensitivity of FMR for the indirect study of subtle structural changes in ultrathin films, using conventional laboratory equipment.

Acknowledgments

This work was supported by the European Research Council (ERC StG-259082, 2DTHERMS), Xunta de Galicia (2012-Projet No. CP072) and by the Ministry of Science of Spain (Project No. MAT2013-44673-R). J. M. V. F. also acknowledges the same organization for an FPI grant. E.W. and J.M. thank UNCuyo Argentina for Grant No C011.

* Electronic address: f.rivadulla@usc.es

[1] A. Vailionis, H. Boschker, W. Siemons, E. P. Houwman,

D. H. A. Blank, G. Rijnders, and G. Koster, Phys. Rev. B **83**, 064101 (2011), URL http://link.aps.org/doi/10.1103/PhysRevB.83.064101.

[2] A. Y. Borisevich, H. J. Chang, M. Huijben, M. P. Oxley, S. Okamoto, M. K. Niranjan, J. D. Burton, E. Y. Tsymbal, Y. H. Chu, P. Yu, et al., Phys. Rev. Lett. **105**, 087204 (2010), URL http://link.aps.org/doi/10.1103/PhysRevLett.105.087204.

[3] F. Sandiumenge, J. Santiso, L. Balcells, Z. Konstantinovic, J. Roqueta, A. Pomar, J. P. Espinós, and B. Martínez, Phys. Rev. Lett. **110**, 107206 (2013), URL http://link.aps.org/doi/10.1103/PhysRevLett.110.107206.

[4] J. Heidler, C. Piamonteze, R. V. Chopdekar, M. A. Uribe-Laverde, A. Alberca, M. Buzzi, A. Uldry, B. Delley, C. Bernhard, and F. Nolting, Phys. Rev. B **91**, 024406 (2015), URL http://link.aps.org/doi/10.1103/PhysRevB.91.024406.

[5] D. Pesquera, G. Herranz, A. Barla, E. Pellegrin, F. Bondino, E. Magnano, F. Sánchez, and J. Fontcuberta, Nature Communications **3**, 1189 (2012).

[6] L. Qiao, J. H. Jang, D. J. Singh, Z. Gai, H. Xiao, A. Mehta, R. K. Vasudevan, A. Tselev, Z. Feng, H. Zhou, et al., Nano Letters **15**, 4677 (2015).

[7] L. Marín, L. A. Rodríguez, C. Magén, E. Snoeck, R. Arras, I. Lucas, L. Morellón, P. A. Algarabel, J. M. De Teresa, and M. R. Ibarra, Nano Letters **15**, 492 (2015).

[8] R. Aso, D. Kan, Y. Shimakawa, and H. Kurata, Advanced Functional Materials **24**, 5177 (2014), ISSN 1616-3028, URL http://dx.doi.org/10.1002/adfm.201303521.

[9] C. Aruta, G. Ghiringhelli, V. Bisogni, L. Braicovich, N. B. Brookes, A. Tebano, and G. Balestrino, Phys. Rev. B **80**, 014431 (2009), URL http://link.aps.org/doi/10.1103/PhysRevB.80.014431.

[10] Z. Xiaofang, C. Long, L. Yang, S. Christian M., D. Shuai, L. Hui, Z. Xiaoqiang, C. Shengqi, Z. Lirong, Z. Jing, et al., Nature Communications **5**, 4253 (2014), URL http://www.nature.com/ncomms/2014/140709/ncomms5283/full/ncomms5283.html.

[11] J. Suntivich, H. A. Gasteiger, N. Yabuuchi, H. Nakanishi, J. B. Goodenough, and Y. Shao-Horn, Nature Chemistry **3**, 546 (2011).

[12] D. Doennig and R. Pentcheva, Scientific Reports **5**, 7909 (2015).

[13] H. Boschker, M. Huijben, A. Vailionis, J. Verbeeck, S. van Aert, M. Luysberg, S. Bals, G. van Tendeloo, E. P. Houwman, G. Koster, et al., Journal of Physics D: Applied Physics **44**, 205001 (2011), URL http://stacks.iop.org/0022-3727/44/i=20/a=205001.

[14] A. M. Glazer, Acta Crystallogr. Sect. B **28**, 3384 (1972).

[15] A. Vailionis, H. Boschker, Z. Liao, J. R. A. Smit, G. Rijnders, M. Huijben, and G. Koster, Applied Physics Letters **105**, 131906 (2014), URL http://scitation.aip.org/content/aip/journal/apl/105/13/10.1063/1.4896969.

[16] J. M. Vila-Fungueiriño, B. Rivas-Murias, B. Rodríguez-González, O. Txoperena, D. Ciudad, L. E. Hueso, M. Lazzari, and F. Rivadulla, ACS Applied Materials & Interfaces **7**, 5410 (2015).

[17] J. Smit and H. Beljers, Philips Res. Rep. **10**, 113 (1955).

[18] M. Barturen, J. Milano, M. Vásquez-Mansilla, C. Helman, M. A. Barral, A. M. Llois, M. Eddrief, and M. Marangolo, Phys. Rev. B **92**, 054418 (2015), URL http://link.aps.org/doi/10.1103/PhysRevB.92.054418.

[19] C. Vittoria, *Microwave properties of magnetic films* (World Scientific, 1993), ISBN 9781118211494.

[20] K. Steenbeck and R. Hiergeist, Applied Physics Letters **75**, 1778 (1999), URL http://scitation.aip.org/content/aip/journal/apl/75/12/10.1063/1.124817.

[21] F. Tsui, M. C. Smoak, T. K. Nath, and C. B. Eom, Applied Physics Letters **76**, 2421 (2000), URL http://scitation.aip.org/content/aip/journal/apl/76/17/10.1063/1.126363.

[22] G. Alejandro, M. Otero-Leal, M. Granada, D. Laura-Ccahuana, M. Tovar, E. Winkler, and C. M. T., Journal of Physics: Condensed Matter **22**, 25602 (2010).

[23] V. A. Ivanshin, J. Deisenhofer, H.-A. Krug von Nidda, A. A. Loidl, A.and Mukhin, and M. V. Balbashov, A. M.and Eremin, Physical Review B **61**, 6213 (2010).

[24] H. Boschker, M. Huijben, A. Vailionis, J. Verbeeck, S. van Aert, M. Luysberg, S. Bals, G. van Tendeloo, E. P. Houwman, G. Koster, et al., Journal of Magn. Magnetic Mat. **323**, 2632 (2011).

[25] M. Belmeguenai, S. Mercone, C. Adamo, L. Méchin, C. Fur, P. Monod, P. Moch, and D. G. Schlom, Phys. Rev. B **81**, 054410 (2010).

[26] B. Cullity and C. Graham, *Introduction to Magnetic Materials* (Wiley, 2011), ISBN 9781118211496.

[27] S. Ikeda, K. Miura, H. Yamamoto, K. Mizunuma, H. Gan, M. Endo, S. Kanai, J. Hayakawa, F. Matsukura, and H. Ohno, Nature Materials **9**, 721 (2010).

[28] F. Vidal, Y. Zheng, P. Schio, F. Bonilla, M. Barturen, J. Milano, D. Demaille, E. Fonda, A. De Oliveira, and V. Etgens, Physical Review Letters **109**, 117205 (2012).

[29] E. Sallica Leva, R. Valente, F. Marttínez Tabares, M. Vásquez Mansilla, S. Roshdestwensky, and A. Butera, Physical Review B **82**, 144410 (2010).

[30] H. Kronmüller and M. Fähnle, *Micromagnetism and the microstructure of ferromagnetic solids* (Cambridge University Press, 2003), ISBN 9781118211495.

6. Use of PAD for deposition of epitaxial thin films over large areas

In the next paper we describe the fabrication of wafer-scale functional thin films by PAD. Crack-free, homogeneous 18 nm thick epitaxial film of $LaMnO_3$ over 1-inch diameter STO substrate was achieved in a single PAD deposition process. The homogeneity over the whole wafer, crystallinity, and reproducibility make the process compatible with the industrial requirements and with fundamental research. Particularly interesting is the metallic, robust ferromagnetic moment and high magnetoresistance at room temperature found in samples annealed in air.

X ray experiments in different areas revealed a very narrow distribution of the lattice parameter, which demonstrate a great crystalline homogeneity. The lack of defects and the thickness in this large area was corroborated by optical measurements in different points of the layer. Finally, more than three hundred Hall bars and the room temperature conductivity were defined by optical lithography. The results show that the conductivity of all of them is in a very narrow range; resistivity ρ=7.5$\pm$1.5 mΩcm.

6.1. Paper I

Room-temperature ferromagnetism in thin films of $LaMnO_3$ deposited by a chemical method over large areas

José M. Vila-Fungueiriño

B. Rivas-Murias

B. Rodríguez-González

O. Txoperena

D. Ciudad

Luis E. Hueso

Massimo Lazzari

F. Rivadulla

ACS Applied Materials & Interfaces 2015, 7(9), 5410-5414

DOI: 10.1021/am508941j

7. Deposition of epitaxial oxide heterostructures by PAD

Properties of oxide heterostructures reside on the quality of their individual layers and their interfaces. The ability of developing high quality multilayer structures is common in physical methods but not so by CSD routes due to the difficulty to control the roughness and thickness of films, which is crucial to obtain abrupt interfaces. In this chapter we explain our achievement in the synthesis and characterization of epitaxial nanometric bilayers combining manganites and cobaltites in different configurations.

As for the cobalt oxide we select the perovskite $LaCoO_3$ (LCO) as an interesting material for thin films as it can act as insulating barrier in oxide-based magnetic junctions. The bulk is insulator and diamagnetic, but in thin film form becomes ferromagnetic and insulator. It is one of the few ferromagnetic-insulator (FM-I) materials known. We demonstrated in Paper II the suitability of PAD for synthesizing high quality thin films of ferromagnetic and insulator LCO.

Growing ultrathin films of a ferromagnetic insulating (LCO) on top of a ferromagnetic metallic (LMO) film is an important step in the fabrication of advanced devices, like spin-filtering tunnel barriers. The high-resolution TEM confirm the epitaxial growth of layers, with clear interfaces analyzed by EELS. In Paper III a 4 nm layer of LCO was deposited on top of LMO showing a high epitaxial quality. A two-step feature in the ferromagnetic cycle is observed, what can be attributed to an independent switching of the magnetization in the LMO and LCO layers. The resistivity measurement shows that growing a continuous layer of 4 nm thick LCO on top of LMO is enough to provide an insulating behavior, demonstrating that there is a uniform coverage over the metallic layer.

LCO/LMO bilayers were deposited also on LAO substrates (Paper IV). Both bilayers on tensile-straining STO and compressive-straining LAO show an increase of the magnetization and coercive field with respect to individual ferromagnetic layers. Either in Paper III and Paper IV we suggest that this increase is due to a strong ferromagnetic superexchange interaction of Mn^{4+}-O-Co^{2+} at the interface.

In Paper V we report the magnetic and electronic transport measurements across epitaxial bilayers of LCO (3.5 nm) on top of LSMO (20 nm) deposited on conductive Nb-doped STO substrate. The epitaxial quality of the bilayers allowed us to measure I−V curves at room temperature and at 4K with conducting atomic force microscopy (C-AFM). The results exhibit the typical features of a tunneling process. The curves were fitted to the Simmons model to determine the height (φ) and width (s) of the insulating LCO barrier. The results yield φ = 0.40 ± 0.05 eV (0.50 ± 0.01 eV) at room temperature (4K) and s = 3 nm, in good agreement with the structural analysis.

Our results demonstrate that complex structures of high quality nanometric multilayers can be achieved through a simple and accessible chemical technique like PAD, with the quality required for fundamental studies of interface coupling.

7.1. Paper II

Strain-induced ferromagnetism and magnetoresistance in epitaxial thin films of $LaCoO_3$ prepared by polymer-assisted deposition

F. Rivadulla

Zhenxing Bi

Eve Bauer

B. Rivas-Murias

José M. Vila-Fungueiriño

Quanxi Jia

Chemistry of Materials 2013, 25 (1), 55-58

DOI: 10.1021/cm3031472

7.2. Paper III

Interface magnetic coupling in epitaxial bilayers of $La_{0.92}MnO_3/LaCoO_3$ prepared by polymer-assisted deposition

José M. Vila-Fungueiriño

B. Rivas-Murias

B. Rodríguez-González

F. Rivadulla

Chemistry of Materials 2014, 26 (3), 1480-1484

DOI: 10.1021/cm403868y

7.3. Paper IV

Strong interfacial magnetic coupling in epitaxial bilayers of $LaCoO_3/LaMnO_3$ prepared by chemical solution deposition

José M. Vila-Fungueiriño

B. Rivas-Murias

F. Rivadulla

Thin Solid Films 2014, 553, 81-84

DOI: 10.1016/j.tsf.2013.11.060

7.4. Paper V

Tunnel conduction in epitaxial bilayers of ferromagnetic $LaCoO_3/La_{2/3}Sr_{1/3}MnO_3$ deposited by a chemical solution method

Irene Lucas

José M. Vila-Fungueiriño

Pilar Jiménez-Cavero

B. Rivas-Murias

César Magén

Luís Morellón

F. Rivadulla

ACS Applied Materials & Interfaces 2014, 6(23), 21279-21285

DOI: 10.1021/am506259p

8. Synthesis of layered misfit cobalt-oxides: anisotropic materials for thermoelectric applications

To further show the advantages of this growth method, we applied PAD to the synthesis of complex structures, like misfit cobalt oxides, which are very difficult to prepare by sputtering or PLD due to problems of stoichiometric transfer from target. For this reason some of these mentioned phases were not reported as thin films. In particular we synthesized films of 3- ($Ca_3Co_4O_9$, $Sr_3Co_4O_9$) and 4- ($[Bi_{1.74}Sr_2O_4][CoO_2]_{1.82}$, $[Bi_2Ba_{1.8}Co_{0.2}O_4][CoO_2]_2$, and $[Bi_{1.68}Ca_2O_4][CoO_2]_{1.69}$) rock salt layers intercalated between the CoO_2. This family of cobaltites exhibit interesting p-type thermoelectric behavior but their synthesis as thin films is complicated.

As we show in the next paper, the epitaxial matching to LAO substrate yields high quality crystalline films, perfectly oriented and with good interfaces. This structural quality results in electrical resistivity and thermopower similar to single-crystals.

Devices based on thermoelectric materials can act as power generation and as refrigeration to decrease energy consumption, but most of them reside in rare and toxic elements. In this respect, nanostructuration of oxide-based materials could increment the efficiency and extension of demanding applications of thermoelectric materials.

8.1. Paper VI

High quality thin films of thermoelectric misfit cobalt oxides prepared by a chemical solution method

B. Rivas-Murias

José M. Vila-Fungueiriño

F. Rivadulla

Scientific Reports 2015, 5, 11889

DOI: 10.1038/srep11889

9. Use of PAD for integration of functional oxides on Silicon

This chapter is intended to demonstrate the integration of epitaxial perovskite oxides in silicon using PAD, in combination with Molecular Beam Epitaxy (MBE). The applications of directly exploiting the properties of oxides monolithically integrated in Si are enormous. However the deposition of epitaxial oxides on silicon is complicated as a native SiO_2 barrier tends to growth at interface. The attempt proposed here is based on a strategy of coupling a soft chemical solution method with buffer layers of STO deposited on Si/SiO_2 by MBE.

In the next review paper presented we show the successful integration of 15 nm LCO film on Si (001), through a 10 nm STO buffer layer deposited by MBE. The epitaxial quality of the film with sharp interfaces is clearly observed by High-Angle Annular Dark Field Scanning Transmission Electron Microscopy (HAADF-STEM). That means that strain is transferred to the film just by using 10 nm of STO instead of a single-crystal substrate.

Inversely, the fact of deposited high quality films by PAD in several nanometers thick buffer layers opens up to create a platform to further deposited subsequently layers. For example, LSMO might be a good candidate to be deposited as bottom electrode for further deposition of ferroelectric oxides, like $BaTiO_3$. The synthesis can be done alternating CSD and high-vacuum techniques in the same route.

9.1. Review

Integration of functional complex oxide nanomaterials on silicon

José M. Vila-Fungueiriño

Romain Bachelet

Guillaume Saint-Girons

Michel Gendry

Martí Gich

Jaume Gázquez

Etienne Ferain

F. Rivadulla

Juan Rodríguez-Carvajal

Narcís Mestres

Adrián Carretero-Genevrier

Frontiers in Physics 2015, 3, 38

DOI: 10.3389/fphy.2015.00038

10. Conclusions and outlook

The most relevant contributions of this thesis are summarized below:

- PAD is competitive with classic physical methods for synthesizing high-quality single-crystal epitaxial thin films of multicationic oxides. This was exemplified in the diversity of materials fabricated in this thesis.
- We have demonstrated that the method is scalable for homogenous deposition over large areas, with the quality demanded for microfabrication techniques. All of this is achieved by an affordable and environment friendly chemical method.
- The role of the polymer in PAD was completely elucidated, opening the path to further optimization with different families of polymers.
- Chapter 8 shows that complex oxides difficult to grow by PLD can be prepared by PAD due to the different growth conditions of this chemical method. Furthermore, the quasi-equilibrium growth provides new functionalities, as it was illustrated for $LaMnO_3$.
- The synthesis of epitaxial multilayers with independent control of the thickness and composition is possible by this chemical method. These results were explained in chapter 7 with several combinations of materials and thicknesses.
- The integration of perovskite oxides in silicon was achieved in the case of $LaCoO_3$.

Future studies in Polymer Assisted Deposition should contemplate some of these possibilities:

- The ability of PAD for conformal coating of large and irregular surfaces.
- The combination with nanoparticles in the early stages of solution preparation can be used to nanostructuration improvements of some materials (fabrication of composite film/nanoparticle hybrids).
- The synthesis of materials like $BiFeO_3$, $SrIrO_3$, $Pr_2Ir_2O_7$ with 4d, 5d and post-transition metal ions is of great interest, due to their physical properties.
- The progress in PAD approach should contemplate the use of other polymers (polyvinylpyrrolidone, PVP; poly(2-ethyl-2-oxazoline), PEOX; Polyacrylamide, PAm; etc.) and other chelating agents.
- The soft integration of functional oxides in Si by combination of physical techniques and PAD is yet at the beginning of the study of their enormous possibilities.

11. Summary in Galician / Resumo en Galego

11.1. Introdución e motivación

Os óxidos metálicos amosan unha extraordinaria variedade de propiedades físicas con aplicacións en moitos campos diferentes: mecánica, óptica, magnetismo, captación de enerxía, etc. Esta diversidade provén da súa alta gama de composicións e da alta flexibilidade estrutural, que resulta nun amplo rango de interaccións electrónicas e magnéticas a nivel fundamental [i,ii]. Para aproveitar estas propiedades en dimensións reducidas, requírese a fabricación de películas finas de gran calidade cristalina. Un número crecente de óxidos teñen sido sintetizados como películas finas epitaxiais, multicapas ou superredes durante as últimas décadas, pero mediante sofisticadas técnicas de crecemento, principalmente por deposición a alto baleiro (MBE, pulverización catódica, PLD e ALD).

Estas películas caracterízanse por unha excelente homoxeneidade química e cristalina sobre toda a mostra, interfaces abruptas e baixa rugosidade. Ás veces filmes policristalinos bastan para satisfacer as propiedades masivas nunha dimensión reducida, pero as películas epitaxiais monocristalinas son as únicas precisas para estudios fundamentais e algunhas aplicacións avanzadas. Porén, acadar un filme epitaxial por medio dun método de deposición de disolución química (*Chemical Solution Deposition*, CSD) é difícil, e os resultados obtidos mediante estas vías corresponden na meirande parte dos casos a mostras policristalinas. Por esta razón, os resultados obtidos pola Deposición Asistida por Polímero (*Polymer Assisted Deposition*, PAD) na última década abriron unha ruta prometedora e accesible para a síntese de películas epitaxiais de alta calidade. Ademais, en contraste con outros métodos de CSD, a PAD foi seleccionada porque en principio non precisa dunha manipulación química complexa, reactivos tóxicos, destilación, refluxo, etc.

Con todo, moitos aspectos químicos do método PAD aínda continúan sen ser clarexados. Como consecuencia, algúns resultados foron difíciles de reproducir por distintos grupos de investigación. Nesta tese identificáronse os aspectos químicos máis relevantes do método PAD. Optimizamos este método para producir películas finas epitaxiais homoxéneas de óxidos multicatiónicos sobre áreas de varios centímetros cadrados. Como amosamos nesta tese, os filmes depositados deste xeito medran preto de condicións de equilibrio termodinámico, condicionados polo substrato, tensión, temperatura, tratamento térmico, atmosfera, etc. Isto representa unha diferenza importante con relación ós métodos físicos clásicos, como PLD, onde os aspectos cinéticos definen o crecemento dos filmes por riba dos aspectos termodinámicos. Así, non só estudar os materiais sintetizados, senón tamén estudar o proceso de síntese en si ha prover importantes conclusións para avanzar aínda máis no deseño de métodos químicos máis eficaces, co que engadir funcionalidades adicionais.

Nesta tese aplicamos o método PAD a unha ampla grama de óxidos tipo perovskita: manganitas $La_{1-x}Sr_xMnO_3$ e $La_{1-x}Ca_xMnO_3$; cobaltita $LaCoO_3$; titanato $SrTiO_3$, ferrita $BiFeO_3$, iridato $SrIrO_3$ e bicapas epitaxiais de $LaCoO_3/La_{1-x}Sr_xMnO_3$.

Así acadamos, por vez primeira, a fabricación de bicapas epitaxiais de gran calidade con interfaces abruptas mediante un método de disolución química. A capacidade para acadar multicapas que combinen materiais con distintas propiedades é altamente desexable para aplicacións tecnolóxicas sofisticadas.

Co gallo de demostrar a síntese de materiais esquivos para os procesos de alto baleiro, algúns compostos laminares de cobalto con estrutura complexa e con aplicacións termoeléctricas foron fabricados. O problema de sintetizar películas finas destes materiais polos métodos físicos clásicos de alto baleiro reside na dificultade para transferir a súa estequiometría, debido á distinta natureza dos catións das súas estruturas. Por iso demostramos a síntese de alta calidade mediante PAD de $Ca_3Co_4O_9$, $Sr_3Co_4O_9$, $[Bi_{1.74}Sr_2O_4][CoO_2]_{1.82}$, $[Bi_2Ba_{1.8}Co_{0.2}O_4][CoO_2]_2$ e $[Bi_{1.68}Ca_2O_4][CoO_2]_{1.69}$.

Finalmente, a posibilidade de integración non agresiva de óxidos en silicio mediante PAD en combinación con MBE foi explorada nesta tese. O silicio é o segundo elemento máis abondoso (só despois do osíxeno) na codia terrestre e a base para a industria electrónica. Con todo, a deposición de óxidos epitaxiais en silicio é complicada, xa que unha barreira de SiO_2 nativa tende a crecer na interface. Para resolver este obstáculo tentamos unha estratexia de combinar CSD con capas de STO depositadas mediante MBE.

Existen moitos métodos distintos para a obtención de películas finas de óxidos, ben por vías físicas ou químicas. Tan só nos centraremos nos métodos químicos, como alternativa ós físicos, que empregan disolucións, os métodos CSD. Hai unha gran diversidade destes métodos [3,4,5,6,7]: sol-xel, Deposición en Baño Químico (CBD), procesos con quelatos, de hidrólise-condensación, PAD, Descomposición Metal-Orgánica (MOD), SILAR, hidrotermais, electroquímicos, etc.

En xeral os métodos CSD deben satisfacer varias esixencias: solubilidade dos precursores, homoxeneidade da disolución sen separación de fases (isto é, precipitación), estabilidade a longo prazo da disolución, boa adherencia e viscosidade axeitada da disolución ó substrato e a descomposición completa dos precursores no tratamento térmico sen producir fendas no filme.

As principais vantaxes dos métodos CSD con respecto ós físicos son o seu baixo custo, execución doada e a aplicabilidade para revestir áreas grandes. Calquera método CSD segue tres pasos xerais:

1. Preparación dunha disolución estable (disolución precursora) que conteña os catións de interese.
2. Deposición da disolución sobre o substrato mediante calquera sistema capaz de revestir a superficie cunha capa homoxénea da disolución precursora.
3. Tratamento térmico nunhas condicións de atmosfera e temperatura dadas para eliminar o disolvente e a parte orgánica da disolución e inducir a cristalización da película inorgánica. Este proceso pode implicar algúns pasos intermedios con distintas temperaturas, dependendo da composición final do filme.

A técnica que empregamos, PAD, é un método CSD particular de base acuosa co que Jia *et al.* [71,72,73] obtiveron películas finas de óxidos epitaxais. Esta ruta mostrou unha gran mellora na cristalinidade e na calidade estrutural con respecto á maioría dos métodos CSD. O procesamento é similar ó de calquera método CSD pero con algunhas peculiaridades inherentes na fase de preparación da disolución, debido ó uso dun polímero para coordinar e estabilizar os catións.

A primeira e principal etapa para a obtención de películas finas inorgánicas por PAD é preparar disolucións estables dos metais individuais co polímero en medio acuoso. Para elo sales dos metais con alta solubilidade, tales como nitratos, cloruros ou acetatos, son disoltas en auga e estabilizadas en presenza dun polímero. Este polímero dota de viscosidade á disolución, a cal é un parámetro fundamental durante o proceso de deposición, por *spin-coating* ou *dip-coating*. O uso de polímeros con grupos amino terminais ($-NH_2$), como a Polietilenimina (PEI), promove a coordinación directa dos catións e prevén da hidrólise e outras reaccións indesexables. A interacción entre o polímero e o metal está principalmente dominada pola atracción nucleofílica do grupo amino cara o catión. De xeito similar a un quelato, o alto número de interaccións dentro da mesma molécula reforza a formación do complexo final. Non obstante, non sempre é posible obter un grao de coordinación satisfactorio cos metais. Así, cando a coordinación cun catión non é suficientemente boa, un axente quelatante pode ser empregado para coordinarse ó metal en disolución e que a PEI estableza interaccións co complexo metálico. O AEDT é o ligando típico empregado en PAD, dado que o complexo resultante $[AEDT\text{-}M]^{-n}$ está cargado negativamente e pode interaccionar electrostaticamente coa PEI cargada positivamente a un *pH* baixo

abondo. A combinación de metal-AEDT/PEI foi documentada para producir disolucións precursoras estables de cando menos 45 elementos diferentes [72]. A elección axeitada do precursor catiónico é moi importante para evitar problemas co contraión. Pola mesma razón e para evitar problemas de contaminación con Na^+ nos filmes, o AEDT e non a súa forma conxugada de sal sódica debe ser usado.

A continuación a disolución precursora co polímero é filtrada para purificala, e analízase a concentración do metal que permanece na disolución retida. Esta disolución pode ser concentrada ata un valor de molaridade axeitado antes de ser depositada por *spin-coating* ou calquera outro método axeitado para producir unha película polimérica homoxénea sobre un substrato. A filtración da disolución precursora é crucial para obter películas delgadas homoxéneas.

O derradeiro paso na síntese de filmes mediante PAD é o tratamento térmico da película polimérica que contén o metal ou metais para obter una película delgada cristalina. Durante o tratamento térmico teñen lugar a evaporación do disolvente, a descomposición do polímero e a cristalización da película inorgánica final. Unha vez máis o polímero ten un papel importante ó protexer o metal durante a fase de quentamento inicial, especialmente para fabricar compostos multicatiónicos para previr a formación de óxidos individuais.

11.2. Caracterización da disolución precursora

A PEI é un polímero hidrosoluble cun grao variable de ramificación e peso molecular composto de grupos amina. A cantidade de aminas primarias, secundarias e terciarias depende do uso de axentes de reticulación durante a polimerización da aziridina. O grao de ramificación e a distribución do peso molecular de diferentes PEIs comerciais determinouse por Resonancia Magnética Nuclear de ^{13}C-RMN e ^{1}H-RMN. Para este estudo compararonse PEIs de *Sigma Aldrich* (SA-PEI) e de *Supelco Analytical* (SU-PEI). A porcentaxe de grupos amino primario, secundario e terciario foi: 1º:2º:3º=39:37:24 para SU-PEI e 31:35:34 para SA-PEI. En consecuencia, o grao de ramificación, definido como a razón de aminas 2º/3º, foi 1,54 para SU-PEI e 1,03 para SA-PEI.

A pesar destas diferenzas estruturais en RMN, o comportamento químico en disolución acuosa de ámbolos tipos de PEI non revela diferenzas significativas. As valoracións potenciométricas ácidas das disolucións de SU-PEI e SA-PEI amosaron resultados moi semellantes con tres constantes de

protonación; sendo os pK_a para as aminas primaria, secundaria e terciaria ≈10.5, ≈6.4 e ≈4.2, respectivamente. En calquera caso, hai que remarcar que non atopamos ningunha diferenza significativa nos resultados finais (calidade das películas) empregrando SU-PEI ou SA-PEI.

Nesta tese preparamos disolucións estables de 16 elementos (Ca^{+2}, Sr^{+2}, Ba^{+2}, Ti^{+4}, V^{+5}, Mn^{+2}, Fe^{+2}, Co^{+2}, Zn^{+2}, Ir^{+3}, La^{+3}, Pr^{+3}, Al^{+3}, Bi^{+3}, B^{+3}, Ge^{+4}). As disolucións son filtradas antes da deposición para evitar defectos e agregados que destrúan a homoxeneidade das películas e obstaculicen a escalabilidade do método para fabricar películas finas de gran calidade sobre áreas grandes. Co fin de eliminar os agregados as disolucións fíltranse usando unha cela de filtración *Amicon*, cun filtro de corte de 10 kDalton. Os catións non coordinados, anións e a fracción do polímero de baixo peso molecular son eliminados neste paso na fracción permeada, mentres que a porción retida e purificada da disolución é empregada para a síntese dos filmes.

A partir de Cromatografía por Exclusión de Tamaño (SEC) fíxose unha comparación das porcións retidas e permeadas da disolución filtrada. Só as fraccións cun peso molecular moi baixo son eliminadas, cun peso molecular medio de ≈ 1.000 g/mol, con respecto ós valores de M_n = 193.000 g/mol para SU-PEI e M_n = 35.000 g/mol para SA-PEI. Por outra banda, os experimentos de RMN revelaron menores aínda que importantes diferenzas entre as especies poliméricas retidas e permeadas a través da membrana *Amicon*. Todas elas refírense a grupos metileno en unidades N-CH_2-CH_2-N, representando unha estrutura que contén maioritariamente aminas primarias e terciarias. Este feito indica a presenza de diferentes especies que poden ser illadas a partir do seu distinto tamaño molecular. As especies máis pequenas, permeadas, presentan unha estrutura globular cunha diferente natureza química que poden ser separadas no proceso de purificación. Esta estrutura diferente ten implicacións no diferente comportamento en disolución e en consecuencia nunha coordinación inhomoxénea cos metais.

A información cuantitativa sobre o peso molecular destes compoñentes poliméricos máis pequenos foi obtida a partir da atenuación da sinal de RMN con Espectroscopia de Difusión Ordenada (DOSY), a través da determinación dos seus coeficientes de difusión, *D*. O valor do coeficiente foi estimado como *D* = 109 $\mu m^2 s^{-1}$, o que resulta en M_n ≈ 5.000 g/mol. Medicións semellantes para a PEI sen filtrar revelaron a mostra como unha mestura de dúas compoñentes, cunha compoñente moi pequena, é dicir, a fracción permeada, e unha segunda compoñente con *D* = 21 $\mu m^2 s^{-1}$ e M_n > 200.000 g/mol.

Polo tanto, identificamos a presenza de fraccións de baixo peso molecular do polímero na solución permeada, cunha estrutura molecular distinta e por iso con propiedades químicas distintas. A orixe desas moléculas máis pequenas está relacionado coa polimerización e por tanto deben estar presentes na maioría das PEIs comerciais de alto peso molecular.

Para seguir a coordinación das especies catiónicas á PEI e para determinar a súa concentración nas disolucións purificadas realizamos análises de Espectroscopia de Emisión Atómica con Plasma Indutivamente Acoplado (EEA-PIA). Esta análise química permite estudar a eficiencia da interacción da PEI cos metais e cos complexos aniónicos comparando o rendemento entre as porcións retidas e permeadas durante a filtración. Canto maior sexa a formación de complexos poliméricos cos metais maior será o grao de retención xa que a fin de permanecer na porción retida o metal ou complexo necesariamente debe estar coordinado á PEI. A maioría dos elementos utilizados neste traballo amosaron un comportamento satisfactorio nas disolucións poliméricas, con altos rendementos, normalmente superiores ao 60%. Ademais, a maioría destas disolucións son estables durante meses e incluso anos. Para algúns metais, deben terse en conta restricións de *pH* para evitar a hidrólise do metal. Por exemplo, a hidrólise do La^{+3} ten lugar a *pH* ≈8.5 mentres que a do Mn^{+2} ten lugar a *pH* ≈7.

Unha vez que a disolución metal-polímero estable está lista, a súa viscosidade pode ser axustada, tanto incrementándoa evaporando auga como diminuíndoa diluíndo con auga destilada. A viscosidade dinámica η das disolucións foi medida a 20ºC cun densímetro *DMA 4100M Anton Paar* cun módulo microviscosímetro *Lovis 2000 ME*. Os valores de viscosidade foron axustados no rango de η≈3-4 mPa.s para obter as condicións óptimas de deposición no *spin coating*.

11.3. Síntese de películas delgadas

Antes da deposición, hai que seleccionar o substrato axeitado e acondicionalo para incrementar a adherencia da disolución e obter unha superficie plana cunha terminación homoxénea. O pretratamento depende de cada substrato pero en xeral é preciso un ataque químico selectivo en combinación cun tratamento térmico a alta temperatura para a reconstrución da superficie. Especificamente para o $SrTiO_3$ (001), unha superficie plana e homoxénea terminada en TiO_2 foi obtida mediante ataque químico ácido do SrO en auga rexia e un posterior tratamento térmico a 1.000ºC. A observación da superficie por Microscopia de Forzas Atómicas (AFM) confirma que a rugosidade é moi baixa, con valores de rugosidade cuadrática media de 0,13 nm.

A disolución final é depositada no spin coater modelo *WS-650-23 NPP* de *Laurell* controlando varios parámetros da disolución (volume, viscosidade, tensión superficial), do substrato (rugosidade, hidrofilicidade, tamaño, forma), do *spin coater* (velocidade, aceleración, tempo) e do ambiente (humidade

e temperatura). A maioría dos substratos nesta tese tiñan dimensión de 5x5 mm^2, polo que as condicións de depósito foron optimizadas para este tamaño. O volume da disolución dispensada foi ≈ 30-50 µL, cunha aceleración de 250 rpm/s ata acadar 3.000-4.500 rpm durante 20 s.

A capa polimérica homoxénea co metal é finalmente tratada termicamente a alta temperatura a fin de obter a película fina inorgánica. Seguimos a descomposición térmica do polímero mediante Análise Termogravimétrico (TGA) nunha termobalanza *Q5000 IR* de *TA Instruments.* A curva TGA da PEI amosa unha forte degradación oxidante do polímero por baixo de 400ºC, cunha perda de ≈ 80 % de masa e a súa completa eliminación ≈ 575ºC. O AEDT tamén se descompón completamente a esas temperaturas.

O tratamento térmico promove a formación da película preto de condicións de equilibrio termodinámico outorgando unha gran calidade e cristalinidade. Atendendo ó crecemento sobre o substrato distínguense tres modos principais de crecemento dos filmes:

- Frank-van der Merwe (capa a capa). O substrato é completamente recuberto pola primeira capa da película.
- Volmer-Weber (en illas ou 3D). A interacción entre os átomos da película é máis forte que cós do substrato.
- Stranski-Krastanov (capas e illas). É o caso intermedio e o máis común.

Cada material require unhas condicións particulares de temperatura, tempo e atmosfera. O tratamento térmico é a fase onde o crecemento de quasi-equilibrio termodinámico define a estrutura e as propiedades da película.

11.4. Caracterización da estrutura cristalina de filmes

As películas finas son unha forma 2D a escala nanométrica onde novas funcionalidades son posibles con respecto á condición masiva. A estabilización de filmes de diferentes óxidos con distintas propiedades e a posibilidade de proxectar esas propiedades mediante tensión epitaxial recibiu gran atención por parte dos investigadores [123]. O crecemento epitaxial refírese ó proceso de medrar unha película mono-cristalina con coherencia estrutural, orientación cristalográfica e axuste á cela unidade do substrato. A tensión

inducida polo substrato axuda a modular a cela unidade da película tanto dunha maneira compresiva como de tracción.

Segundo o desaxuste entre o substrato e a película, a epitaxia pode producirse de tres xeitos:

1. Cando a cela unidade do filme é menor có substrato, a película medrará baixo tensión expansiva.
2. Cando a cela unidade do filme é maior có substrato, a película medrará en tensión compresiva.
3. Totalmente relaxada. Isto acontece cando hai un desaxuste moi grande entre o filme e o substrato, ou cando a película excede un determinado grosor por riba do cal a tensión é desprezable.

A tensión introducida no material da película fina ten un importante impacto na orde electrónica e magnética ao modificarse o entorno cristalino da rede. Actualmente existe unha crecente oferta comercial de substratos mono-cristalinos que permiten un axuste moi fino no grao de tensión que se pode aplicar.

A difracción de Raios X é a técnica de caracterización fundamental para o estudo da estrutura cristalina das películas delgadas. As razóns son que a lonxitude de onda dos Raios X é da orde da distancia dos planos cristalográficos e que son técnicas non destrutivas. Nesta tese os experimentos de Raios X foron realizados en dous difractómetros semellantes: *Empyrean* e *X`Pert Pro* de *PANalytical*, cunha plataforma Euler e unha lonxitude de onde incidente de $\lambda\left(K_{\alpha_1}^{Cu}\right)$ = 1,540598 Å. Segundo esta óptica, diferentes configuracións da fonte de Raios X, plataforma, mostra e detector foron aplicadas ás películas. Deste xeito realizáronse medidas tales como varrido $\theta/2\theta$, *Rocking curve*, varrido en φ, Cartografía en Espazo Recíproco (RSM), análises en reflexións semienteiras e Reflectividade de Raios X.

11.5. Resultados e conclusións

Películas finas de manganitas de $La_{1-x}Ca_xMnO_3$ foron sintetizadas en STO (001) con disolucións de concentración 0.4 M e tratadas a 950ºC en fluxo de O_2 (15 mL/min) durante 2 horas. Estas películas son monocristalinas e orientadas sen a presenza de fases secundarias. A caracterización magnética e as medidas de transporte eléctrico coinciden co comportamento masivo agardado, agás no caso do composto nai, $LaMnO_3$, que sendo semicondutor e antiferromagnético pasa a ser unha película metálica e

ferromagnética a temperatura ambiente. Isto é debido á deficiencia en La que xorde das condicións impostas durante o crecemento para acomodarse ó substrato. A segregación de La é apreciada mediante XRD e AFM condutor, que detecta a presenza de exceso de La_2O_3 illante.

A anisotropía magnética de películas epitaxiais do semi-metal ferromagnético $La_{0.7}Sr_{0.3}MnO_3$ pode ser determinada polas condicións de crecemento. Comparamos películas de LSMO medradas por PLD e PAD mediante difracción de Raios X e Resonancia ferromagnética. As mostras de PLD amosan unha gran anisotropía cúbica no plano cunha gran compoñente uniaxial, mentres que a compoñente uniaxial é suprimida na mostra de PAD resultando nunha meirande anisotropía cúbica. Este cambio é debido a un diferente patrón de rotación dos octaedros de MnO_6 para acomodarse á tensión expansiva do substrato nas condicións termodinámicas de crecemento.

Para demostrar a escalabilidade do método PAD, unha película condutora continua de 18 nm de $LaMnO_3$ deficiente en La depositouse nunha oblea dunha polgada de diámetro. Os experimentos de Raios X revelaron unha distribución moi estreita do parámetro de rede de 3,87 Å, e a calidade morfolóxica foi corroborada mediante medidas ópticas de elipsometría. Ademais, a medida de máis de 300 barras Hall patroneadas no filme confirmaron o comportamento metálico en toda a mostra a temperatura ambiente, cun valor de resistividade de ρ=7.5±1.5 mΩcm.

O crecemento de bicapas epitaxias con aplicación para dispositivos avanzados confirmouse coa deposición de 4 nm de $LaCoO_3$ sobre $LaMnO_3$. O ciclo ferromagnético mostra un trazo en dúas etapas que pode ser atribuído a unha conmutación independente dos momentos magnéticos de ambas capas. As medidas de resistividade amosan que con 4 nm de espesor de $LaCoO_3$ pode probarse o recubrimento total con este material semicondutor sobre a primeira capa metálica. Tanto en substratos de $SrTiO_3$ como en $LaAlO_3$ obsérvase un aumento do campo coercitivo vinculado coa interacción de Mn^{4+}-O-Co^{2+} na interface. Tamén describimos as medidas magnéticas e eléctricas a través de bicapas epitaxiais de LCO (3,5 nm) e LSMO (20 nm), que permitiron determinar curvas I-V cun comportamento de efecto túnel. Estas curvas foron axustadas ao modelo de Simmons determinando a altura (φ) e espesor (*t*) do barreira illante de LCO, dando φ = 0.40 ± 0.05 eV e 0.50 ± 0.01 eV a temperatura ambiente e a 4K, respectivamente, e *t* = 3 nm, en concordancia co análise estrutural.

Para afondar máis no crecemento de materiais en réxime de quasi-equilibrio aplicamos a técnica PAD a estruturas aínda máis complexas, como a dos óxidos de cobalto laminares con propiedades termoeléctricas tipo-*p* pero de síntese complicada en filmes. En particular crecéronse $Ca_3Co_4O_9$, $Sr_3Co_4O_9$, $[Bi_{1.74}Sr_2O_4][CoO_2]_{1.82}$, $[Bi_2Ba_{1.8}Co_{0.2}O_4][CoO_2]_2$ e $[Bi_{1.68}Ca_2O_4][CoO_2]_{1.69}$. A coincidencia epitaxial dos filmes co substrato de LAO a través de capa con estrutura de cloruro sódico da lugar a películas de

gran calidade cristalina, aliñadas e con claras interfaces. Esta calidade estrutural permite comportamentos eléctricos e termoeléctricos semellantes ós dos monocristais masivos.

Por último a integración en Silicio de perovskitas epitaxiais foi abordado combinando PAD e MBE, demostrando o crecemento de películas de $LaCoO_3$. A calidade epitaxial do filme observouse por Microsopia Electrónica de Transmisión, que amosa a calidade das interfaces do $LaCoO_3$ co $SrTiO_3$ e deste co Silicio. Este traballo abre o camiño cara a integración doutros materiais e transferir as súas propiedades a dispositivos baseados en Silicio.

Publications

- **José M. Vila-Fungueiriño**, B. Rivas-Murias, F. Rivadulla.
  Synthesis and magnetic properties of manganite thin films on Si by polymer assisted (PAD) and pulsed laser deposition (PLD)
  Materials Research Society Symposium Proceedings 2012, 1449, bb07-02
  DOI: 10.1557/opl.2012.1040

- F. Rivadulla, Z. Bi, E. Bauer, B. Rivas-Murias, **José M. Vila-Fungueiriño**, Q. X. Jia
  Strain-induced ferromagnetism and magnetoresistance in epitaxial thin films of $LaCoO_3$ prepared by polymer-assisted deposition
  Chemistry of Materials 2013, 25 (1), 55-58
  DOI: 10.1021/cm3031472

- P. L. Bach, **José M. Vila-Fungueiriño**, V. Leborán, Elías Ferreiro-Vila, B. Rodríguez-González, F. Rivadulla
  Strain-induced enhancement of the thermoelectric power in thin films of hole-doped $La_2Ni_{4+\delta}$
  APL Materials 2013, 1, 021101-021106
  DOI: 10.1063/1.4818356

- **José M. Vila-Fungueiriño**, B. Rivas-Murias, F. Rivadulla
  Strong interfacial magnetic coupling in epitaxial bilayers of $LaCoO_3/LaMnO_3$ prepared by chemical solution deposition
  Thin Solid Films 2014, 553, 81-84
  DOI: 10.1016/j.tsf.2013.11.060

- **José M. Vila-Fungueiriño**, B. Rivas-Murias, B. Rodríguez-González, F. Rivadulla
  Interface magnetic coupling in epitaxial bilayers of $La_{0.92}MnO_3/LaCoO_3$ prepared by polymer-assisted deposition
  Chemistry of Materials 2014, 26 (3), 1480-1484
  DOI: 10.1021/cm403868y

- Irene Lucas, **José M. Vila-Fungueiriño**, Pilar Jiménez-Cavero, B. Rivas-Murias, César Magén, Luis Morellón, F. Rivadulla
  Tunnel conduction in epitaxial bilayers of ferromagnetic $LaCoO_3/La_{2/3}Sr_{1/3}MnO_3$ deposited by a chemical solution method
  ACS Applied Materials & Interfaces 2014, 6 (23), 21279-21285
  DOI: 10.1021/am506259p

- **José M. Vila-Fungueiriño**, B. Rivas-Murias, B. Rodríguez-González, O. Txoperena, D. Ciudad, Luis E. Hueso, Massimo Lazzari, F. Rivadulla
  Room-temperature ferromagnetism in thin films of $LaMnO_3$ deposited by a chemical method over large areas
  ACS Applied Materials & Interfaces 2015, 7(9), 5410-5414
  DOI: 10.1021/am508941j

- **José M. Vila-Fungueiriño**, Romain Bachelet, Guillaume Saint-Girons, Michel Gendry, Marti Gich, Jaume Gázquez, Etienne Ferain, F. Rivadulla, Juan Rodríguez-Carvajal, Narcís Mestres, Adrián Carretero-Genevrier
  Integration of functional complex oxide nanomaterials on silicon
  Frontiers in Physics 2015, 3, 38
  DOI: 10.3389/fphy.2015.00038

- B. Rivas-Murias, **José M. Vila-Fungueiriño**, F. Rivadulla
  High quality thin films of thermoelectric misfit cobalt oxides prepared by a chemical solution method
  Scientific Reports 2015, 5, 11889
  DOI: 10.1038/srep11889

Bibliography

i J.B. Goodenough, *Progress in Solid State Chemistry* 5, 145-399 (1971) “Metallic oxides”.

ii P. A. Cox, *Transition metal oxides: an introduction to their electronic structure and properties*. OUP Oxford, 2010.

3 F.F. Lange, *Science* 273, 903-909 (1996) “Chemical solution routes to single-crystal thin films”.

4 C.J. Brinker, G.W. Scherer, *Sol-Gel Science: The Physics and Chemistry of Sol-Gel Processing*. Academic Press, Inc., San Diego, CA, 1990.

5 R.W. Schwartz, T. Schneller, R. Waser, *Comptes Rendus Chimie* 7, 433-461 (2004) “Chemical solution deposition of electronic oxide films”.

6 D. Mitzi, *Solution Processing of Inorganic Materials*. John Wiley & Sons, Inc., Hoboken, NJ, 2009.

7 T. Schneller, R. Waser, M. Kosec, D. Payne, *Chemical Solution Deposition of Functional Oxide Thin Films*. Springer-Verlag, Wien, 2013.

8 T. Hayashi, N. Ohji, K. Hirohara, T. Fukunaga, H. Maiwa, *Japanese Journal of Applied Physics* 32, 4092 (1993) “Preparation and properties of ferroelectric $BaTiO_3$ thin films by sol-gel process”.

9 S.-C. Pang, M.A. Anderson, T.W. Chapman, *Journal of the Electrochemical Society* 147, 444-450 (2000) “Novel electrode materials for thin-film ultracapacitors: comparison of electrochemical properties of sol-gel-derived and electrodeposited manganese dioxide”.

10 J.H. Park, M.G. Kim, H.M. Jang, S. Ryu, Y.M. Kim, *Applied Physics Letters* 84, 1338-1340 (2004) “Co-metal clustering as the origin of ferromagnetism in Co-doped ZnO thin films”.

11 J.-H. Lee, K.-H. Ko, B.-O. Park, *Journal of Crystal Growth* 247, 119-125 (2003) “Electrical and optical properties of ZnO transparent conducting films by the sol-gel method”.

12 D.C. Bradley, *Chemical Reviews* 89, 1317-1322 (1989) "Metal alkoxides as precursors for electronic and ceramic materials".

13 J. Davidovits, *Journal of Thermal Analysis* 37, 1633-1656 (1991) "Geopolymers. Inorganic polymeric new materials".

14 J.P. Zheng, T.R. Jow, *Journal of the Electrochemical Society* 142, L6-L8 (1995) "New charge storage mechanism for electrochemical capacitors".

15 J.P. Zheng, P.J. Cygan, T.R. Jow, *Journal of the Electrochemical Society* 142, 2699-2703 (1995) "Hydrous ruthenium oxide as an electrode material for electrochemical capacitors".

16 C. Di Valentin, G. Pacchioni, A. Selloni, S. Livraghi, E. Giamello, *Journal of Physical Chemistry B.* 109, 11414-11419 (2005) "Characterization of paramagnetic species in N-doped TiO_2 powders by EPR spectroscopy and DFT calculations".

17 Y. Lu, Y. Yin, B.T. Mayers, Y. Xia, *Nano Letters* 2, 183-186 (2002) "Modifying the Surface Properties of Superparamagnetic Iron Oxide Nanoparticles through a Sol-Gel Approach".

18 M.L. Zheludkevich, R. Serra, M.F. Montemor, K.A. Yasakau, I.M.M. Salvado, M.G.S. Ferreira, *Electrochimica Acta* 51, 208-217 (2005) "Nanostructured sol-gel coatings doped with cerium nitrate as pre-treatments for AA2024-T3 Corrosion protection performance".

19 S. Pavasupree, J. Jitputti, S. Ngamsinlapasathian, S.T. Yoshikawa, *Materials Research Bulletin* 43, 149-157 (2008) "Hydrothermal synthesis, characterization, photocatalytic activity and dye-sensitized solar cell performance of mesoporous anatase TiO_2 nanopowders".

20 J. Raittila, H. Huhtinen, P. Paturi, Y.P. Stepanov, *Physica C: Superconductivity and its Applications* 371, 90-96 (2002) "Preparation of superconducting $YBa_2Cu_3O_{7-\delta}$ nanopowder by deoxydation in Ar before final oxygenation".

21 H.-M. Xiong, Y. Xu, Q.-G. Ren, Y.-Y. Xia, *Journal of the American Chemical Society* 130, 7522-7523 (2008) "Stable aqueous ZnO@polymer core-shell nanoparticles with tunable photoluminescence and their application in cell imaging".

22 A. Punnoose, H. Magnone, M.S. Seehra, J. Bonevich, *Physical Review B* 64, 1744201 (2001) "Bulk to nanoscale magnetism and exchange bias in CuO nanoparticles".

23 J. Park, J. Joo, G.K. Soon, Y. Jang, T. Hyeon, *Angewandte Chemie* 46, 4630-4660 (2007) "Synthesis of monodisperse spherical nanocrystals".

24 C.-C. Wang, J.Y. Ying, *Chemistry of Materials* 11, 3113-3120 (1999) "Sol-gel synthesis and hydrothermal processing of anatase and rutile titania nanocrystals".

25 T. Kasuga, M. Hiramatsu, A. Hoson, T. Sekino, K. Niihara, *Langmuir* 14, 3160-3163 (1998) "Formation of titanium oxide nanotube".

26 F. Krumeich, H.-J. Muhr, M. Niederberger, F. Bieri, B. Schnyder, R. Nesper, *Journal of the American Chemical Society* 121, 8324-8331 (1999) “Morphology and topochemical reactions of novel vanadium oxide nanotubes”.

27 C.T. Kresge, M.E. Leonowicz, W.J. Roth, J.C. Vartuli, J.S. Beck, *Nature* 359, 710-712 (1992) “Ordered mesoporous molecular sieves synthesized by a liquid-crystal template mechanism”.

28 A. Imhof, D J. Pine, *Nature* 389, 948-951 (1997) “Ordered macroporous materials by emulsion templating”.

29 P. Yang, T. Deng, D. Zhao, P. Feng, D. Pine, B.F. Chmelka, G.M. Whitesides, G.D. Stucky, *Science* 282, 2244-2246 (1998) “Hierarchically ordered oxides”.

30 M. Ebelmen, *Annales de Chimie et de Physique* 16, 129-166 (1846) “Recherches sur les combinaisons des acides borique et silicique avec les éthers”.

31 T.P. Niesen, M.R. De Guire, *Journal of Electroceramics* 6, 169-207 (2001) “Review: Deposition of ceramic thin films at low temperatures from aqueous solutions”.

32 A.V. Vinogradov, V.V. Vinogradov, *RSC Advances* 4, 45903-45919 (2014) “Low-temperature sol-gel synthesis of crystalline materials”.

33 J. Livage, M. Henry, C. Sanchez, *Progress in Solid State Chemistry* 18, 259-341 (1988) “Sol-gel chemistry of transition metal oxides”.

34 L.L. Hench, J.K. West, *Chemical Reviews* 90, 33-72 (1990) “The Sol-Gel process”.

35 M. Pechini, United States Patent No. 3,330,697 (1967).

36 M. Liu, D. Wang, *Journal of Materials Research* 10, 3210-3221 (1995) “Preparation of $La_{1-z}Sr_zCo_{1-y}Fe_yO_{3-x}$ thin films, membranes, and coatings on dense and porous substrates”.

37 U. Choppali, B.P. Gorman, *Journal of Luminescence* 128, 1641-1648 (2008) “Structural and optical properties of nanocrystalline ZnO thin films synthesized by the citrate precursor route”.

38 M.S.G. Baythoun, F.R. Sale, *Journal of Materials Science* 17, 2757-2769 (1982) “Production of strontium-substituted lanthanum manganite perovskite powder by the amorphous citrate process”.

39 J. Rivas, L.E. Hueso, A. Fondado, F. Rivadulla, M.A. Lopez-Quintela, *Journal of Magnetism and Magnetic Materials* 221, 57-62 (2000) “Low field magnetoresistance effects in fine particles of $La_{0.67}Ca_{0.33}MnO_3$ perovskites”.

40 J. Fukushima, K. Kodaira, T. Matsushita, *Journal of Materials Science* 19, 595-598 (1984) “Preparation of ferroelectric PZT films by thermal decomposition of organometallic compounds”.

41 M. Klee, R. Eusemann, R. Waser, W. Brand, H. Van Hal, *Journal of Applied Physics* 72, 1566-1576 (1992) “Processing and electrical properties of $Pb(Zr_xTi_{1-x})O_3$ (x= 0.2–0.75) films: Comparison of metallo-organic decomposition and sol-gel processes”.

42 G.D. Hu, X. Cheng, W.B. Wu, C.H. Yang, *Applied Physics Letters* 91, 2909 (2007) "Effects of Gd substitution on structure and ferroelectric properties of $BiFeO_3$ thin films prepared using metal organic decomposition".

43 M.E. Gross, M. Hong, S.H. Liou, P.K. Gallagher, J. Kwo, *Applied Physics Letters* 52, 160-162 (1988) "Versatile new metalorganic process for preparing superconducting thin films".

44 O. Castano, A. Cavallaro, A. Palau, J.C. Gonzalez, M. Rossell, T. Puig, F. Sandiumenge, N. Mestres, S. Pinol, A. Pomar, X. Obradors, *Superconductor Science and Technology* 16, 45-53 (2003) "High quality $YBa_2Cu_3O_7$ thin films grown by trifluoroacetates metal-organic deposition".

45 M.W. Rupich, D.T. Verebelyi, W. Zhang, T. Kodenkandath, X. Li, *MRS Bulletin* 29, 572-578 (2004) "Metalorganic deposition of YBCO films for second-generation high-temperature superconductor wires".

46 T. Manabe I. Yamaguchi, W. Kondo, S. Mizuta, T. Kumagai, *Journal of Materials Research* 12, 541-545 (1997) "Preparation of epitaxial $La_{1-x}Sr_xMnO_3$ films on $SrTiO_3$ (001) by dipping-pyrolysis process".

47 K. Daoudi, T. Tsuchiya, I. Yamaguchi, T. Manabe, S. Mizuta, T. Kumagai, *Journal of Applied Physics* 98, 013507 (2005) "Microstructural and electrical properties of $La_{0.7}Ca_{0.3}MnO_3$ thin films grown on $SrTiO_3$ and $LaAlO_3$ substrates using metal-organic deposition".

48 A. Galembeck, O.L. Alves, *Thin Solid Films* 365, 90-93 (2000) "$BiVO_4$ thin film preparation by metalorganic decomposition".

49 A. Li, C. Ge, P. Lü, N. Ming, *Applied Physics Letters* 6, 1347-1349 (1996) "Preparation of perovskite conductive $LaNiO_3$ films by metalorganic decomposition".

50 K.W. Terry, C.G. Lugmair, T.D. Tilley, *Journal of the American Chemical Society* 119, 9745-9756 (1997) "Tris(tert-butoxy)siloxy complexes as single-source precursors to homogeneous zirconia- and hafnia-silica materials. An alternative to the sol-gel method".

51 M.T. Soo, N. Prastomo, A. Matsuda, G. Kawamura, H. Muto, A.F.M. Noor, Z. Lockman, K.Y. Cheong, *Applied Surface Science* 258, 5250-5258 (2012) "Elaboration and characterization of sol-gel derived ZrO_2 thin films treated with hot water".

52 G. Yi, Z. Wu, M. Sayer, *Journal of Applied Physics* 64, 2717-2724 (1988) "Preparation of $Pb(Zr,Ti)O_3$ thin films by sol gel processing: Electrical, optical, and electro-optic properties".

53 K.D. Budd, S.K. Dey, D.A. Payne, *British Ceramic Society Proceedings* 36, 107-121 (1985) "Sol-gel processing of $PbTiO_3$, $PbZrO_3$, PZT and PLZT thin films".

54 U. Hasenkox, S. Hoffmann, R. Waser, *Journal of Sol-Gel Science and Technology* 12, 67-79 (1988) "Influence of precursor chemistry on the formation of $MTiO_3$ (M= Ba, Sr) ceramic thin films".

55 D.H. Kang, J.H. Kim, J.H. Park, K.H. Yoon, *Materials Research Bulletin* 36, 265-276 (2001) "Characteristics of $(Pb_{1-x}Sr_x)TiO_3$ thin film prepared by a chemical solution processing".

56 B. Lee, J. Zhang, *Thin Solid Films* 388, 107-113 (2001) “Preparation, structure evolution and dielectric properties of $BaTiO_3$ thin films and powders by an aqueous sol-gel process”.

57 M. Sedlar, M. Sayer, *Journal of Sol-Gel Science and Technology* 5, 27-40 (1995) “Reactivity of titanium isopropoxide, zirconium propoxide and niobium ethoxide in the system of 2-methoxyethanol, 2,4-pentanedione and water”.

58 R.W. Schwartz, *Chemistry of Materials* 9, 2325-2340 (1997) “Chemical solution deposition of perovskite thin films”.

59 A.H. Carim, B.A. Tuttle, D.H. Doughty, S.L. Martinez, *Journal of the American Ceramic Society* 74, 1455-1458 (1991) “Microstructure of Solution-Processed Lead Zirconate Titanate (PZT) Thin Films”.

60 J. Emerson-Reynolds, *Journal of the Chemical Society, Transactions* 45, 162-165 (1884) “XXV. - On the synthesis of galena by means of thiocarbamide, and the deposition of lead sulphide as a specular film”.

61 G. Hodes, *Physical Chemistry Chemical Physics* 9, 2181-2196 (2007) “Semiconductor and ceramic nanoparticle films deposited by chemical bath deposition”.

62 S.R. Deo, A.K. Singh, L. Deshmukh, M. Abu Bin Hasan Susan, *Journal of Electronic Materials* 44, 4098-4127 (2015) “Metal Chalcogenide Nanocrystalline Solid Thin Films”.

63 P.K. Nair, M.T.S. Nair, V.M. García, O.L. Arenas, Y. Peña, A. Castillo, I.T. Ayala, O. Gomezdaza, A. Sánchez, J. Campos, H. Hu, R. Suárez, M.E. Rincón, *Solar Energy Materials and Solar Cells* 52, 313-344 (1998) “Semiconductor thin films by chemical bath deposition for solar energy related applications”.

64 C.D. Lokhande, *Materials Chemistry and Physics* 27, 1-43 (1991) “Chemical deposition of metal chalcogenide thin films”.

65 R.S. Mane, C.D. Lokhande, *Materials Chemistry and Physics* 65, 1-31 (2000) “Chemical deposition method for metal chalcogenide thin films”.

66 K. Govender, D.S. Boyle, P.B. Kenway, P. O'Brien, *Journal of Materials Chemistry* 14, 2575-2591 (2004) “Understanding the factors that govern the deposition and morphology of thin films of ZnO from aqueous solution?”.

67 M.Ristov, G. Sinadinovski, I. Grozdanov, *Thin Solid Films* 123, 63-67 (1985) “Chemical deposition of Cu2O thin films”.

68 Y.F.Nicolau, *Applied Surface Science* 22-23 (Part 2), 1061-1074 (1985) “Solution deposition of thin solid compound films by a successive ionic-layer adsorption and reaction process”.

69 O. Lupan, S. Shishiyanu, L. Chow, T. Shishiyanu, *Thin solid films* 516, 3338-3345 (2008) “"Nanostructured zinc oxide gas sensors by successive ionic layer adsorption and reaction method and rapid photothermal processing”.

70 H.M. Pathan, C.D. Lokhande, *Bulletin of Materials Science* 27, 85-111 (2004) “Deposition of metal chalcogenide thin films by successive ionic layer adsorption and reaction (SILAR) method”.

71 Q.X. Jia, T.M. McCleskey, A.K. Burrell, Y. Lin, G.E. Collis, H. Wang, A.D.Q. Li, S.R. Foltyn, *Nature materials* 3, 529-532 (2004) “Polymer-assisted deposition of metal-oxide films”.

72 A.K. Burrell, T.M. McCleskey, Q.X. Jia, *Chemical Communication* 1271-1277 (2008) “Polymer assisted deposition”.

73 T.M. McCleskey, P. Shi, E. Bauer, M.J. Highland, J.A. Eastman, Z.X. Bi, P.H. Fuoss, P.M. Baldo, W. Ren, B.L. Scott, A.K. Burrell, Q.X. Jia, *Chemical Society Reviews* 43, 2141-2146 (2014) “Nucleation and growth of epitaxial metal-oxide films based on polymer-assisted deposition”.

74 B.F. Smith, T.W. Robison, N.N. Sauer, *Environmental separation of heavy metals: Engineered processes*, edited by A. Sengupta. Lewis, New York, 2001.

75 G.F. Zou, J. Zhao, H.M. Luo, T.M. McCleskey, A.K. Burrell, Q.X. Jia, *Chemical Society Reviews*, 42, 439-449 (2013) “Polymer-assisted-deposition: a chemical solution route for a wide range of materials”.

76 Y. Lin, H. Wang, M.E. Hawley, S.R. Foltyn, Q.X. Jia, G.E. Collis, A.K. Burrell, T.M. McCleskey, *Applied Physics Letters* 85, 3426-3428 (2004) “Epitaxial growth of Eu_2O_3 thin films on $LaAlO_3$ substrates by polymer-assisted deposition”.

77 M.A. Garcia, M.N. Ali, T. Parsons-Moss, P.D. Ashby, H. Nitsche, *Thin Solid Films* 516, 6261-6265 (2008) “Metal oxide films produced by polymer-assisted deposition (PAD) for nuclear science applications”.

78 M.N. Ali, M.A. Garcia, T. Parsons-Moss, H. Nitsche, *Nature Protocols* 5, 1440-1446 (2010) “Polymer-assisted deposition of homogeneous metal oxide films to produce nuclear targets”.

79 Q. Yi, P. Zhai, Y. Sun, Y. Lou, J. Zhao, B. Sun, B. Patterson, H. Luo, W. Zhang, L. Jiao, H. Wang, G. Zou, *ACS Applied Materials and Interfaces* 7, 18218-18224 (2015) “Aqueous Solution-Deposited Molybdenum Oxide Films as an Anode Interfacial Layer for Organic Solar Cells”.

80 E.S. Gillman, D. Costello, M. Moreno, A. Raspopin, R. Kasica, L. Chen, *Journal of Applied Physics* 108, 044310 (2010) “Polymer-assisted conformal coating of TiO_2 thin films”.

81 M.A. Garcia, M.N. Ali, N.N. Chang, T. Parsons-Moss, P.D. Ashby, J.M. Gates, L. Stavsetra, K.E. Gregorich, H. Nitsche, *Nuclear Instruments and Methods in Physics Research, Section A: Accelerators, Spectrometers, Detectors and Associated Equipment* 592, 483-485 (2008) “Heavy-ion irradiation of thulium(III) oxide targets prepared by polymer-assisted deposition”.

82 A.K. Burrell, T.M. McCleskey, P. Shukla, H. Wang, T. Durakiewicz, D.P. Moore, C.G. Olson, J.J. Joyce, Q.X. Jia, *Advanced Materials* 19, 3559-3563 (2007) “Controlling oxidation states in uranium oxides through epitaxial stabilization”.

83 S.D. Senanayake, K. Mudiyanselage, A.K. Burrell, J.T. Sadowski, H. Idriss, *Journal of Physical Chemistry C* 119, 24895-24901 (2015) “Surface Reactions of Ethanol over UO_2 (100) Thin Film”.

84 L. Kang, Y. Gao, Z. Zhang, J. Du, C. Cao, Z. Chen, H. Luo, *Journal of Physical Chemistry C,* 114, 1901-1911 (2010) "Effects of annealing parameters on optical properties of thermochromic VO_2 films prepared in aqueous solution".

85 L. Kang, Y. Gao, H. Luo, Z. Chen, J. Du, Z. Zhang, *ACS Applied Materials and Interfaces* 3, 135-138 (2011) "Nanoporous thermochromic VO_2 films with low optical constants, enhanced luminous transmittance and thermochromic properties".

86 F. Yue, W. Huang, Q. Shi, D. Li, Y. Hu, Y. Xiao, X. Deng, C. Wang, *Journal of Sol-Gel Science and Technology* 72, 565-570 (2014) "Phase transition properties of vanadium oxide films deposited by polymer-assisted deposition".

87 S.S. Kalagi, D.S. Dalavi, R.C. Pawar, N.L. Tarwal, S.S. Mali, P.S. Patil, *Journal of Alloys and Compounds* 493, 335-339 (2010) "Polymer assisted deposition of electrochromic tungsten oxide thin films".

88 S.J. Hong, H. Jun, J.S. Lee, *Scripta Materialia* 63, 757-760 (2010) "Nanocrystalline WO_3 film with high photo-electrochemical activity prepared by polymer-assisted direct deposition".

89 Y. Lin, J. Xie, H. Wang, Y. Li, C. Chavez, S. Lee, S.R. Foltyn, S.A. Crooker, A.K. Burrell, T.M. McCleskey, Q.X. Jia, *Thin Solid Films* 492, 101-104 (2005) "Green luminescent zinc oxide films prepared by polymer-assisted deposition with rapid thermal process".

90 H. Ren, G. Xiang, G. Gu, X. Zhang, W. Wang, P. Zhang, B. Wang, X. Cao, *Journal of Nanomaterials* 295358 (2012) "Zinc vacancy-induced room-temperature ferromagnetism in undoped Zno thin films".

91 P. Shukla, E.M. Minogue, T.M. McCleskey, Q.X. Jia, Y. Lin, P. Lu, A. K. Burrell, *Chemical Communications* 8, 847-849 (2006) "Conformal coating of nanoscale features of microporous Anodisc™ membranes with zirconium and titanium oxides".

92 M. Jain, P. Shukla, Y. Li, M.F. Hundley, H. Wang, S.R. Foltyn, A.K. Burrell, T.M. McCleskey, Q.X. Jia, *Advanced Materials* 18, 2695-2698 (2006) "Manipulating magnetoresistance near room temperature in $La_{0.67}Sr_{0.33}MnO_3/La_{0.67}Ca_{0.33}MnO_3$ films prepared by polymer assisted deposition".

93 M. Jain, Y. Li, M.F. Hundley, M. Hawley, B. Maiorov, I.H. Campbell, L. Civale, Q.X. Jia, P. Shukla, A.K. Burrell, T.M. McCleskey, *Applied Physics Letters* 88, 232510 (2006) "Magnetoresistance in polymer-assisted deposited Sr- and Ca-doped lanthanum manganite films".

94 M. Jain, Y. Lin, P. Shukla, Y. Li, H. Wang, M.F. Hundley, A.K. Burrell, T.M. McCleskey, S.R. Foltyn, Q.X. Jia, *Thin Solid Films* 515, 6411-6415 (2007) "Ferroic metal-oxide films grown by polymer assisted deposition".

95 M. Jain, E. Bauer, F. Ronning, M.F. Hundley, L. Civale, H. Wang, B. Maiorov, A.K. Burrell, T.M. McCleskey, S.R. Foltyn, R.F. DePaula, Q.X. Jia, *Journal of the American Ceramic Society* 91, 1858-1863 (2008) "Mixed-valence perovskite thin films by polymer-assisted deposition".

96 Y. Lin, J.-S. Lee, H. Wang, Y. Li, S.R. Foltyn, Q.X. Jia, G.E. Collis, A.K. Burrell, T.M. McCleskey, *Applied Physics Letters* 85, 5007-5009 (2004) "Structural and dielectric properties of epitaxial $Ba_{1-x}Sr_xTiO_3$ films grown on $LaAlO_3$ substrates by polymer-assisted deposition".

97 M. Jain, E. Bauer, Y. Lin, H. Wang, A.K. Burrell, T.M. McClesky, Q.X. Jia, *Integrated Ferroelectrics* 100, 132-139 (2004) "$BaTiO_3$-related ferroelectric thin films by polymer assisted deposition".

98 H. Du, W.Z. Liang, Y. Li, M. Gao, Y. Zhang, Y. Lin, *Integrated Ferroelectrics* 159, 127-133 (2015) "Effect of a Second Annealing Process on the Properties of $BaTiO_3$ Thin Films on Polycrystalline Nickel Substrates Grown by Polymer-Assisted Deposition".

99 H.M. Luo, M. Jain, S.A. Baily, T.M. McCleskey, A.K. Burrell, E. Bauer, R.F. DePaula, P.C. Dowden, L. Civale, Q.X. Jia, *Journal of Physical Chemistry B* 111, 7497-7500 (2007) "Structural and ferromagnetic properties of epitaxial SrRuO3 thin films obtained by polymer-assisted deposition".

100 F. Rivadulla, Z. Bi, E. Bauer, B. Rivas-Murias, J.M. Vila-Fungueiriño, Q.X. Jia, *Chemistry of Materials* 25, 55-58 (2013) "Strain-induced ferromagnetism and magnetoresistance in epitaxial thin films of $LaCoO_3$ prepared by Polymer-Assisted Deposition".

101 H.M. Luo, M. Jain, T.M. McCleskey, E. Bauer, A.K. Burrell, Q.X. Jia, *Advanced Materials* 19, 3604-3607 (2007) "Optical and structural properties of single phase epitaxial p-type transparent oxide thin films".

102 Y.-H. Chuai, H.-Z. Shen, Y.-D. Li, B. Hu, Y. Zhang, C.-T. Zheng, Y.-D. Wang, *RSC Advances* 5, 49301-49307 (2015) "Epitaxial growth of highly infrared-transparent and conductive $CuScO_2$ thin film by polymer-assisted-deposition method".

103 S.M. Baber, Q. Lin, G. Zou, N. Haberkorn, S.A. Baily, H. Wang, Z. Bi, H. Yang, S. Deng, M.E. Hawley, L. Civale, E. Bauer, T.M. McCleskey, A.K. Burrell, Q.X. Jia, H.M. Luo, *Journal of Physical Chemistry C* 115, 25338-25342 (2011) "Magnetic properties of self-assembled epitaxial nanocomposite $CoFe_2O_4$:$SrTiO_3$ and $CoFe_2O_4$:MgO films".

104 E. Bauer, A.H. Mueller, I. Usov, N. Suvorova, M.T. Janicke, G.I.N. Waterhouse, M.R. Waterland, Q.X. Jia, A.K. Burrell, T.M. McCleskey, *Advanced Materials* 20, 4704-4707 (2008) "Chemical solution route to conformal phosphor coatings on nanostructures".

105 H, Luo, A.H. Mueller, T.M. McCleskey, A.K. Burrell, E. Bauer, Q.X. Jia, *Journal of Physical Chemistry C* 112, 6099-6102 (2008) "Structural and photoelectrochemical properties of $BiVO_4$ thin films".

106 J.-S. Hwang, J.-M. Lee, S.K. Vishwanath, J. Kim, *Journal of Vacuum Science and Technology A: Vacuum, Surfaces and Films* 33, 041402 (2015) "Effects of H_2 plasma treatment on the electrical properties of titanium-doped indium oxide films prepared by polymer-assisted deposition".

107 C. Apetrii, H. Schlörb, M. Falter, I. Lampe, L. Schultz, B. Holzapfel, *IEEE Transactions on Applied Superconductivity* 15, 2642-2644 (2005) "YBCO thin films prepared by fluorine-free polymer-based chemical solution deposition".

108 Y.R. Patta, D.E. Wesolowski, M.J. Cima, *Physica C: Superconductivity and its Applications* 469, 129-134 (2009) “Aqueous polymer-nitrate solution deposition of YBCO films”.

109 D.E. Wesolowski, Y.R. Patta, M.J. Cima, *Physica C: Superconductivity and its Applications* 469, 766-773 (2009) “Conversion behavior comparison of TFA-MOD and non-fluorine solution-deposited YBCO films”.

110 W.-W. Yan, C.-X. Zhang, P.-F. Wang, L.-H. Jin, C.-S. Li, Y.-F. Lu, *Gongneng Cailiao/Journal of Functional Materials* 43, 984-987 (2012) “Rapid preparation of YBCO superconductive film by the nitrate PAD solution deposition”.

111 G. Zou, H. Luo, F. Ronning, B. Sun, T.M. McCleskey, A.K. Burrell, E. Bauer, Q.X. Jia, *Angewandte Chemie - International Edition* 49, 1782-1785 (2010) “Facile chemical solution deposition of high-mobility epitaxial germanium films on silicon”.

112 H. Luo, Y. Lin, H. Wang, J.H. Lee, N.A. Suvorova, A.H. Mueller, A.K. Burrell, T.M. McCleskey, E. Bauer, I.O. Usov, M.E. Hawley, T.G. Holesinger, Q.X. Jia, *Advanced Materials* 21, 193-197 (2009) “A Chemical Solution Approach to Epitaxial Metal Nitride Thin Films”.

113 H. Luo, H. Wang, G. Zou, E. Bauer, T.M. McCleskey, A.K. Burrell, Q.X. Jia, *Transactions on Electrical and Electronic Materials* 11, 54-60 (2010) “A Review of Epitaxial Metal-Nitride Films by Polymer-Assisted Deposition”.

114 H. Luo, Y. Lin, H. Wang, C.-Y. Chou, N.A. Suvorova, M.E. Hawley, A.H. Mueller, F. Ronning, E. Bauer, A.K. Burrell, T.M. McCleskey, Q.X. Jia, *Journal of Physical Chemistry C* 112, 20535-20538 (2008) “Epitaxial GaN thin films prepared by polymer-assisted deposition”.

115 G. Zou, M. Jain, H. Zhou, H. Luo, S.A. Baily, L. Civale, E. Bauer, T.M. McCleskey, A.K. Burrell, Q.X. Jia, *Chemical Communications* 45, 6022-6024 (2008) “Ultrathin epitaxial superconducting niobium nitride films grown by a chemical solution technique”.

116 Y. Zhang, N. Haberkorn, F. Ronning, H. Wang, N.A. Mara, M. Zhuo, L. Chen, J.H. Lee, K.J. Blackmore, E. Bauer, A.K. Burrell, T.M. McCleskey, M.E. Hawley, R.K. Schulze, L. Civale, T. Tajima, Q.X. Jia, *Journal of the American Chemical Society* 133, 20735-20737 (2011) “Epitaxial superconducting δ-MoN films grown by a chemical solution method”.

117 H. Luo, G. Zou, H. Wang, J.H. Lee, Y. Lin, H. Peng, Q. Lin, S. Deng, E. Bauer, T.M. McCleskey, A.K. Burrell, Q.X. Jia, *Journal of Physical Chemistry C* 115, 17880-17883 (2011) “Controlling crystal structure and oxidation state in molybdenum nitrides through epitaxial stabilization”.

118 H. Luo, H. Wang, Z. Bi, D.M. Feldmann, Y. Wang, A.K. Burrell, T.M. McCleskey, E. Bauer, M. Hawley, Q.X. Jia, *Journal of the American Chemical Society* 130, 15224-15225 (2008) “Epitaxial ternary nitride thin films prepared by a chemical solution method”.

119 H. Luo, H. Wang, Z. Bi, G. Zou, T.M. McCleskey, A.K. Burrell, E. Bauer, M. Hawley, Y. Wang, Q.X. Jia, *Angewandte Chemie - International Edition* 48, 1490-1493 (2009) "Highly conductive films of layered ternary transition-metal nitrides".

120 G. Zou, H. Wang, N. Mara, H. Luo, N. Li, Z. Di, E. Bauer, Y. Wang, T.M. McCleskey, A.K. Burrell, X. Zhang, M. Nastasi, Q.X. Jia, *Journal of the American Chemical Society* 132, 2516-2517 (2010) "Chemical solution deposition of epitaxial carbide films".

121 G. Zou, H. Luo, Y.Y. Zhang, J. Xiong, Q.M. Wei, M.J. Zhuo, J.Y. Zhai, H.Y. Wang, D. Williams, N. Li, E. Bauer, X.H. Zhang, T.M. McCleskey, Y.R. Li, A.K. Burrell, Q.X. Jia, *Chemical Communications* 46, 7837-7839 (2010) "A chemical solution approach for superconducting and hard epitaxial NbC film".

122 R.E. Jilek, E. Bauer, A.K. Burrell, T.M. McCleskey, Q.X. Jia, B.L. Scott, M.F. Beaux, T. Durakiewicz, J.J. Joyce, K.D. Rector, J. Xiong, K. Gofryk, F. Ronning, R.L. Martin, *Chemistry of Materials* 25, 4373-4377 (2013) "Preparation of epitaxial uranium dicarbide thin films by polymer-assisted deposition".

123 M.G. Blamire, J.L. MacManus-Driscoll, N.D. Mathur, Z.H. Barber, *Advanced Materials* 21, 3827-3839 (2009) "The materials science of functional oxide thin films".

124 M. Opel, *Journal of Physics. D: Applied Physics* 45, 033001 (2012) "Spintronic oxides grown by laser-MBE".

125 M.A. Moram, Z.H. Barber, C.J. Humphreys, T.B. Joyce, P.R. Chalker, *Journal of Applied Physics* 100, 023514 (2006) "Young's modulus, Poisson's ratio, and residual stress and strain in (111)-oriented scandium nitride thin films on silicon".

126 A. Kossoy, E. Wachtel, I. Lubomirsky, *Journal of Electroceramics* 32, 47-51 (2014) "On the Poisson ratio and XRD determination of strain in thin films of $Ce_{0.8}Gd_{0.2}O_{1.9}$".

127 L. Ranno, A. Llobet, R. Tiron, E. Favre-Nicolin, *Applied Surface Science* 188, 170-175 (2002) "Strain-induced magnetic anisotropy in epitaxial manganite films".

128 D.G. Schlom, L.Q. Chen, X. Pan, A. Schmehl, M.A. Zurbuchen, *Journal of the American Ceramic Society* 91, 2429-2454 (2008) "A thin film approach to engineering functionality into oxides".

129 J. Cao, J. Wu, *Materials Science and Engineering: R: Reports* 71, 35-52 (2011) "Strain effects in low-dimensional transition metal oxides".

130 M. Birkholz, *Thin film analysis by X-Ray scattering*. Wiley-VCH, Weinheim, Germany, 2006.

131 D. Pavia, G. Lampman, G. Kriz, J. Vyvyan, *Introduction to spectroscopy*. Cengage Learning, Belmont, CA, 2008, p. 588.

132 A. von Harpe, H. Petersen, Y. Li, T. Kissel, *Journal of Controlled Release* 69, 309-322 (2000) "Characterization of commercially available and synthesized polyethylenimines for gene delivery".

133 U. Steuerle, R. Feuerhake, in *Ullmann's Encyclopedia of Industrial Chemistry*, 7th ed.; Wiley-VCH: Weinheim, Germany, 2007.

134 G. Scherr, U. Steuerle, R. Fikentscher, in *Kirk-Othmer's Encyclopedia of Chemical Technology*, John Wiley & Sons, Inc., New York, NY, 1995, p. 2-40.

135 T.St. Pierre, M. Geckle, *Journal of Macromolecular Science: Part A - Chemistry* 22, 877-887 (1985) "^{13}-NMR analysis of branched polyethyleneimine".

136 E.O. Stejskal, J.E. Tanner, *Journal of Chemical Physics* 42, 288-292 (1965) "Spin diffusion measurements: spin echoes in the presence of a time-dependent field gradient".

137 A. Chen, D. Wu, C.S. Johnson, *Journal of the American Chemical Society* 117, 7965-7970 (1995) "Determination of molecular weight distributions for polymers by diffusion-ordered NMR".

138 S. Auge, P.O. Schmit, C.A. Crutchfield, M.T. Islam, D.J. Harris, E. Durand, M. Clemancey, A.A. Quoineaud, J.M. Lancelin, Y. Prigent, F. Taulelle, M.A. Delsuc, *Journal of Physical Chemistry B* 113, 1914-1918 (2009) "NMR measure of translational diffusion and fractal dimension. Application to molecular mass measurement".

139 R.G. Parr, R.G. Pearson, *Journal of the American Chemical Society* 105, 7512-7516 (1983) "Absolute hardness: companion parameter to absolute electronegativity".

140 Y.Y. Yakubovich, V.G. Alekseev, *Russian Journal of Inorganic Chemistry* 57, 911-915 (2012) "Hydrolysis constants of tervalent lanthanum and lanthanide ions in 0.1 M KNO3 solution".

141 G.E. Krejcarek; K.L. Tucker, *Biochemical Biophysical Research Communications* 77, 581-585 (1977) "Covalent attachment of chelating groups to macromolecules".

142 M.W. Sundberg, C.F. Meares, D.A. Goodwin, C.I. Diamanti, *Nature* 250, 587-588 (1974) "Chelating agents for the binding of metal ions to macromolecules".

143 A.F. Holleman, *Inorganic Chemistry*. Academic Press, San Diego, 2001, p. 1321.

144 O. Lichtenberger, J. Woltersdorf, *Materials Chemistry and Physics* 44, 222-232 (1997) "On the atomic mechanisms of water-enhanced silicon wafer direct bonding".

145 V.E. Agabekov, G.K Zhavnerko, *Russian Journal of General Chemistry* 77, 343-349 (2007) "Mono- and multimolecular Langmuir-Blodgett films as protective coatings for friction surfaces".

146 F. Sánchez, C. Ocal, J. Fontcuberta, *Chemical Society Reviews* 43, 2272-2285 (2014) "Tailored surfaces of perovskite oxide substrates for conducted growth of thin films".

147 M. Kawasaki, K. Takahashi, T. Maeda, R. Tsuchiya, M. Shinohara, O. Ishiyama, T. Yonezawa, M. Yoshimoto, H. Koinuma, *Science* 266, 1540-1542 (1994) "Atomic Control of the $SrTiO_3$ Crystal Surface".

148 J. Chang, Y.-S. Park, S.-K. Kim, *Applied Physics Letters* 92, 152910 (2008) "Atomically flat single-terminated $SrTiO_3$ (111) surface".

149 J.G. Connell, B.J. Isaac, G.B. Ekanayake, D.R. Strachan, S.S.A. Seo, *Applied Physics Letters* 101, 251607 (2012) "Preparation of atomically flat $SrTiO_3$ surfaces using a deionized-water leaching and thermal annealing procedure".

150 M. Kareev, S. Prosandeev, J. Liu, C. Gan, A. Kareev, J. W. Freeland, M. Xiao, J. Chakhalian, *Applied Physics Letters* 93, 061909 (2008) "Atomic control and characterization of surface defect states of TiO_2 terminated $SrTiO_3$ single crystals".

151 G. Binnig, H. Rohrer, C. Gerber, E. Weibel, *Physical Review Letters* 49, 57 (1982) "Surface studies by scanning tunneling microscopy".

152 G. Binnig, C.F. Quate, C. Gerber, *Physical Review Letters* 56, 930 (1986) "Atomic force microscope".

153 P. Haaland, J. McKibben, M. Paradi, "Fundamental constraints on thin film coatings for flat-panel display manufacturing". In *SID* (pp. 79-84), 1995.

154 R.A. Pethrick, K.E. Rankin, *Journal of Materials Science: Materials in Electronics*, 10, 141-144 (1999) "Criteria for uniform thin film formation for polymeric materials".

155 G. Carcano, M. Ceriani, F. Soglio, *Microelectronics International*, 10, 12-20 (1993) "Spin Coating with High Viscosity Photoresist on Square Substrates-Applications in the Thin Film Hybrid Microwave Integrated Circuit Field".

156 S.A. Idris, O.A. Mkhatresh, F. Heatley, *Polymer International* 55, 1040-1048 (2006) "Assignment of ^{1}H NMR spectrum and investigation of oxidative degradation of poly(ethylenimine) using ^{1}H and ^{13}C 1-D and 2-D NMR".

157 I.E. Kirillina, V.N. Voronov, A.M. Dolgonosov, M.A. Lazeikina, *Teploenergetika* 35, 538-539 (1988) "Composition of gaseous products of decomposition of ethylenediaminetetra-acetate".

158 E. Bauer, *Zeitschrift für Kristallographie-Crystalline Materials* 110, 395-431 (1958) "Phänomenologische theorie der kristallabscheidung an oberflächen".

159 H. Yamada, H. Nagamoto, "Thermal Expansion Coefficient and Electrical Conductivity of Based Perovskite-Type Oxide", in S.C. Singhal, H. Ihawara (eds.), *Proc. 3rd Int. Symp. SOFC Electrochem. Soc*., p. 213-219, Pennington, NJ, 1993.

160 J. Schoonman, I. Riess, *Oxygen ion and mixed conductors and their technological applications*. Springer Science & Business Media, 2000.

161 J. D. Bucci, B. K. Robertson, W. J. James, *Journal Applied Crystallography* 5, 187-191 (1972) "The precision determination of the lattice parameters and the coefficients of thermal expansion of $BiFeO_3$".

162 J.R. Chen, W.L. Wang, J.-B. Li, G.H. Rao, *Journal of Alloys and Compounds* 459, 66-70 (2008) "X-ray diffraction analysis and specific heat capacity of $(Bi_{1-x}La_x)FeO_3$ perovskites".

163 J.M. Longo, J.A. Kafalas, R.J. Arnott, *Journal of Solid State Chemistry* 3, 174-179 (1971) "Structure and properties of the high and low pressure forms of $SrIrO_3$".

164 M.B. Salamon, M. Jaime, *Reviews of Modern Physics,* 73, 583 (2001). "The physics of manganites: Structure and transport".

165 P. Schiffer, A.P. Ramirez, W. Bao, S.W. Cheong, *Physical Review Letters,* 75, 3336-3339 (1995). "Low temperature magnetoresistance and the magnetic phase diagram of $La_{1-x}Ca_xMnO_3$".

166 A. Szewczyk, M. Gutowska, B. Dabrowski, *Physical Review B* 72, 224429 (2005) "Specific heat and phase diagram of heavily doped $La_{1-x}Sr_xMnO_3$ ($0.45 \leqslant x \leqslant 1.0$)".

167 J. M. Vila-Fungueiriño, B. Rivas-Murias, F. Rivadulla, Materials Research Society Symposium Proceedings, 1449 (2012) "Synthesis and magnetic properties of manganite thin films on Si by polymer assisted (PAD) and pulsed laser deposition (PLD)".

168 Z. Zeng, M. Greenblatt, M. Croft, *Physical Review B*, 59, 8784-8788 (1999) "Large magnetoresistance in antiferromagnetic $CaMnO_{3-\delta}$".

169 M. Pissas, G. Kallias, *Physical Review B*, 68, 134414 (2003) "Phase diagram of the $La_{1-x}Ca_xMnO_3$ compound ($0.5 \leq x \leq 0.9$)".

170 P.G. Radaelli, G. Iannone, M. Marezio, H.Y. Hwang, S.W. Cheong, J.D. Jorgensen, D.N. Argyriou, *Physical Review B*, 56, 8265 (1997) "Structural effects on the magnetic and transport properties of perovskite $A_{1-x}A'_xMnO_3$ (x= 0.25, 0.30)".

171 J. Rodríguez-Carvajal, M. Hennion, F. Moussa, A.H. Moudden, L. Pinsard, A. Revcolevschi, *Physical Review B*, 57, R3189 (1998) "Neutron-diffraction study of the Jahn-Teller transition in stoichiometric $LaMnO_3$".

172 C. Zener, *Physical Review*, 82, 403 (1951) "Interaction between the d-shells in the transition metals. II. Ferromagnetic compounds of manganese with perovskite structure"

173 V.E. Henrich, G. Dresselhaus, H.J. Zeiger, *Physical Review B* 17, 4908-4921 (1978) "Surface defects and the electronic structure of $SrTiO_3$ surfaces".

USC
UNIVERSIDADE
DE SANTIAGO
DE COMPOSTELA